



A Monte Carlo Model of Pitting Corrosion of Underground Power Transmission Cable

Thesis submitted for the degree of

Doctor of Philosophy

at the University of Leicester

by

Lixin Zhang

Department of Engineering

University of Leicester

2018

Abstract

The life of underground power transmission cables is greatly reduced by pitting corrosion of the reinforcing tin-bronze tapes and this corrosion fatigue leads to cable failure. Since these cables are distributed in different places and can fail at different times, it is difficult to maintain and replace these cables until they fail. Hence, accurate prediction of pit growth in these tapes and plastic deformation analysis of these tapes with pits are crucial steps in cable maintenance.

This thesis documents the findings from the probability distribution of corrosion pits on reinforcing tin-bronze tapes using deterministic Monte Carlo simulations. The findings were compared with the measured pit depth distribution of tapes that have been in service for over 40 years obtained from open literatures. Additionally, the finite element model (FEM) was used to analyse the relationships of applied stress and pit depth with a model of failure mechanisms. The input data for the FEM were based on the pit depth from the simulation and applied internal oil pressure from the experiment data.

A Monte Carlo simulation was performed with every stable pit that had nucleated, propagated, and repassivated on the metal surface, and the model considered the interaction between individual pits in an explicit manner. The measured data were compared against previously published data from actual samples from different locations and with various service durations to investigate the complete distribution of pits. The studies showed that the simulated pit depth distribution is very similar to the experimental pit depth distribution on the tapes. This pit depth distribution model provides a powerful tool to determine the residual life of reinforcing tin-bronze tapes used in underground power transmission cables.

The FEM was used to examine the failure condition of the reinforcing tapes under various applied stress and pit depths. The pit depth was gained from the Monte Carlo

simulations, and the applied stress was based on UTS. Thus, the life of an underground power cable can be calculated. This FEM procedure provides an alternative method to determine the probability of failure of reinforcing tapes and a convenient way to identify the life of underground cables, dependent on the failure model.

Acknowledgements

The author wishes to express his sincere gratitude to his supervisor Prof Pan for his continuous support during this PhD study and related research and for his patience, motivation, and immense knowledge. Prof Pan's guidance helped the author in all the stages of the research and in preparing this thesis. Besides the supervisor, the author would like to thank his co-supervisor Dr Weston for the encouragement and the tough questions that drove the author to widen his research from various perspectives.

This research was conducted alongside a research team led by Dr S. Gnanasambandam. The work presented in the thesis benefited from the published models and data by her team. The author would like to express sincerely gratefulness to Dr S. Gnanasambandam, Mr M. Foresta and Mr H. Zhou. Additionally, the author gratefully acknowledges his colleague Mr A. N. Tabatabaeian for optimising the computer codes. The assistance rendered by Mr M. Foresta in discussing the equations is also gratefully acknowledged.

Finally, the author would like to thank his family, mainly his parents and his wife, for supporting him spiritually throughout the writing this thesis and his life in general.

Finite element analysis of the presented work were performed using COMSOL Multiphysics (License number 7074366).

Table of Contents

Chapter 1. Introduction	1
1.1 Introduction to underground power transmission cables	1
1.2 Failure mechanism of reinforcing tape.....	4
1.3 Asset life of underground power cable	7
1.4 Application of prediction method for simulating pitting corrosion	8
1.5 Research objectives and thesis layout.....	12
Chapter 2. Literature review	16
2.1 Mechanisms of corrosion	16
2.2 Mechanism of pitting corrosion.....	19
2.2.1 Pit nucleation	23
2.2.2 Metastable pitting.....	26
2.2.3 Pit propagation.....	27
2.3 Factors influencing the pitting potential	29
2.3.1 Influence of alloy elements.....	29
2.3.2 Influence of inclusions.....	32
2.3.3 Influence of electrolyte composition	34
2.3.4 Influence of pH and temperature	36
2.4 Faraday’s Law and corrosion factors	38
2.4.1 Faraday’s Law	38
2.4.2 Corrosion reaction factors	40
2.5 Mechanism of corrosion fatigue.....	41
2.6 Numerical methods in predicting pitting corrosion	46
2.6.1 Monte Carlo simulation with pitting corrosion processes.....	46

2.6.2 Empirical models	52
2.6.3 Mechanical model	56
2.7 Overview of nonlinear stress analysis using finite element method	60
2.7.1 Elastic model	63
2.7.2 Elastoplastic model	64
Chapter 3. A critical analysis of pitting corrosion data of underground power transmission cables in the open literature.....	70
3.1 Review of underground cables	70
3.2 Process of copper dissolution and procedure to extract pit depth distribution ..	75
3.3 Experimental pit depth distribution and analysis.....	78
3.4 Key conclusions on the layout from the existing data.....	83
3.5 Summary.....	83
Chapter 4. The Monte Carlo model of pitting corrosion.....	85
4.1 Computational methodology.....	86
4.2 Material properties.....	93
4.3 Results comparison and Monte Carlo model validation	94
4.4 Parametric study of the Monte Carlo model.....	103
4.5 Summary.....	111
Chapter 5. Stress analysis around representative pits in failed cables.....	113
5.1 Review of failure models	113
5.2 Alternative failure criteria based on pitting corrosion	118
5.3 FEM model for reinforcing tape with a critical pit depth	125
5.4 Mesh convergency study	129
5.5 An alternative failure criterion based on the Ultimate tensile strength	133
5.6 Summary.....	142

Chapter 6. Conclusions and recommendations for future work.....	144
6.1 Overall conclusions	144
6.2 Recommendations for future work	147
References	149
Appendix.....	160

List of Figures

Figure 1.1: Excavation of underground cables (http://www.pier-uk.co.uk/category/vacuum-excavation/).....	2
Figure 1.2: Construction of underground power transmission cable [2].....	3
Figure 1.3: The sequence of events leading to cable failure.....	4
Figure 1.4: Tape failure process	7
Figure 2.1: Relationship between various forms of chemical degradation of materials [14].....	17
Figure 2.2: Shape of corrosion pits: (a) deep narrow pit, (b) occluded pit, (c) hemispherical pit [36].....	20
Figure 2.3: Variation in partial anodic current density with potential for a passivating metal [36]	21
Figure 2.4: Evans' diagram of a passive electrode showing sensitivity to pitting corrosion: (a) $E_{cor} < E_b$; (b) $E_{cor} > E_b$ [36]	22
Figure 2.5: Penetration mechanism and phase diagram of a passive film with related processes of ion and electron transfer within the film and at its phase boundaries [43]	24
Figure 2.6: Mechanical film breakdown mechanism and related competing processes [43].....	25
Figure 2.7: Adsorption mechanism with increased local transfer of metal ions and related corrosion current density caused by complexing aggressive anions leading to thinning of the passive layer and increases in field strength and final free corrosion current density within the pit [43]	26
Figure 2.8: Current transients typical of pre-pits [46].....	27
Figure 2.9: Explanation of the nature of E_p . Pits became stable only at potentials above E_2 [46]	28

Figure 2.10: Pitting potential of Fe-Cr alloys as a function of Cr content [47].....	30
Figure 2.11: Effect of molybdenum on pitting potential of 2 Fe-Cr alloys in 1-M NaCl, at 25°C [48]	30
Figure 2.12: Pitting potential of binary Al-Cu, Al-Mg and Al-Zn alloys in 1 M NaCl solution [46].....	31
Figure 2.13: Estimated pitting potential values for binary aluminium alloys in sea water [49].....	32
Figure 2.14: Anodic polarization curves of (a) industrial grade and (b) high-purity samples of Fe-17Cr in 0.12-M HCl, at 25°C [52]	33
Figure 2.15: Effect of inclusions on pit initiation: (a) surface with an inclusion, (b) formation of an aeration cell in the space between an inert inclusion and the metal, (c) anodic dissolution of the inclusion, and (d) formation of a corrosion cell between the cathodic inclusion and the metal [36]	34
Figure 2.16: Effect of 0.1 M NaCl, NaBr, NaF and NaI on pitting potential of copper [53]	35
Figure 2.17: Potentiostatic polarisation curves showing the effect of electrolyte composition on pitting behaviour of copper exposed to aggressive and non-aggressive anions [53]	36
Figure 2.18: Pitting potential of high purity iron, in 1.0 M NaCl at various pH values [46].....	37
Figure 2.19: Critical pitting temperature [46]	38
Figure 2.20: H ₂ /O ₂ fuel cell [36].....	40
Figure 2.21: Different stresses working in a corrosive environment [55].....	42
Figure 2.22: Damage chain showing sequence of events and processes of material degradation [20]	45
Figure 2.23: The shape of a pit [20].....	58

Figure 2.24: Stress-strain curve of uniaxial tensile test (https://en.wikipedia.org/wiki/Stress%E2%80%93strain_curve).....	64
Figure 3.1: An example of route profile (https://connect.ncdot.gov/projects/construction/ConstManRefDocs/ENGINEERING%20CONTROL%20-%20VERIFICATION%20OF%20OVERHEAD%20MOUNTED%20SIGNS.pdf).....	70
Figure 3.2: Excavation of underground cables (http://www.caseyelectricalservice.com.au/hydro-excavation/).....	71
Figure 3.3: Schematic drawing of the power transmission cable. The tape is wrapped around the lead sheath [3]	72
Figure 3.4: Optical image of outer and inner surface of the corroded tin-bronze reinforcing tape. The outer surface (a) is highly discoloured while the inner surface (b) shows only slight discolouration at the edges [3]	73
Figure 3.5: Pits on the outer surface of the tape cut through a line (a), and corresponding profile from 3D optical microscope (b) [3]	74
Figure 3.6: Cross section showing several pits with variable shape, taken perpendicularly to the longitudinal axis of the tape [3]	74
Figure 3.7: The mechanism of copper dissolution (anodic reaction) in NaCl solution [118].....	75
Figure 3.8: (a) Outer and inner surface of the tape covered with bitumen. (b) Outer and inner surface of the tape after bitumen removal with pentane. (c) Tape in the mounting machine. (d) Cross-sectional view of the corrosion pits taken perpendicularly to the longitudinal axis of the tape [1]	77
Figure 3.9: Pit depth distribution for samples from the ROUTE J circuit [3].....	79
Figure 3.10: Pit depth distributions for 2 sets of samples from the same piece of tape in the ROUTE F circuit [3]	80
Figure 3.11: Pit depth distribution for samples from ROUTE A (year 2008) [3]	81
Figure 3.12: Pit depth distribution for samples from ROUTE A (year 2014) [3]	81

Figure 3.13: Pit depth distribution for samples from ROUTE K [3]	82
Figure 4.1: The flow chart of programmes for tracking each individual pit.....	92
Figure 4.2: Pit depth without repassivation occurring.....	95
Figure 4.3: A comparison between maximum and average pit depth.....	95
Figure 4.4: Number of pits for pit growth and pit repassivation within 560 days.....	96
Figure 4.5: The pit depth distribution of Monte Carlo simulation results	97
Figure 4.6: Two sets of samples [3] compared with the Monte Carlo method (MCM) results	99
Figure 4.7: A comparison between pit depth distribution samples from the ROUTE J circuit [3] and the Monte Carlo simulation	100
Figure 4.8: Comparison between the experiment [3] and MCM pit depth distribution of reinforcing tape of 38 years of age	101
Figure 4.9: Comparison between the experiment [3] and MCM pit depth distribution for reinforcing tape of 44 years of age.....	102
Figure 4.10: Monte Carlo model pit depth distributions for different simulation years (8 years, 20 years, and 32 years)	102
Figure 4.11: Pit depth distribution with different dissolution times (three, 100, and 300 days)	104
Figure 4.12: Number of stable pits ($N(t)$) increasing with time under different value of a ($a=1, 3.65, 5, 7, 10, 20$)	105
Figure 4.13: A comparison of pit depth between three temperatures	106
Figure 4.14: A comparison between the experimental [3] and computational pit depth distributions with different γ values	107
Figure 4.15: A comparison between experiment data (Courtesy of Mechanical of Material group) and Monte Carlo simulation results with 100 pits.....	108
Figure 4.16: A comparison between experimental results (Courtesy of Mechanical of Material group) and Monte Carlo simulation results with total 600 pits	108

Figure 4.17: A comparison between two different set of total number of pits.....	110
Figure 5.1: Stages of the corrosion fatigue failure process of reinforcing tape corrosion, and the key events contributing to the life of the cable [3]	114
Figure 5.2: An illustration of the pit-to-crack transition for a single pit that has specific values of the growth rate parameters α and C , while the time to reach x_{crit} is the time of failure (t_f) for the cable [3]	116
Figure 5.3: PDF of pit depth distribution with three parameters (α, n & γ).....	120
Figure 5.4: PDF of pit depth distribution with different value of γ (0.066, 0.166, and 0.266).....	121
Figure 5.5: Failure probability of critical pit depth with different repassivation delay constant γ (0.066, 0.166, and 0.266)	123
Figure 5.6: Failure probability of critical pit depth with different α (1, 2, 3, and 3.7611) which is used in pit growth model	124
Figure 5.7: Failure probability of critical pit depth with different n (0.3, 0.4, 0.5, and 0.583) which is used in pit growth model	124
Figure 5.8: The plate geometry	126
Figure 5.9: The symmetry of the geometry of a pit occurs on the tape for a 2D model	127
Figure 5.10: Von Mises stress of the 3D model.....	129
Figure 5.11: von Mises stress with the 'Extra coarse' mesh	131
Figure 5.12: The von Mises stress with different element sizes	132
Figure 5.13: Average applied stress in x direction vs von Mises stress without plasticity added in the model	134
Figure 5.14: Average applied stress in x direction vs von Mises stress with plasticity added in the model	136
Figure 5.15: Average applied stress in x direction vs von Mises stress with plasticity added in the model and the pit depth is 90 μm	137

Figure 5.16: The averaged applied stress that meet the failure condition with different critical pit depth138

Figure 5.17: Plastic region for the FEM model with pit depth equal to 110 μm : (a) Applied stress with 73.95 MPa, (b) Applied stress with 104.57 MPa, (c) Applied stress with 130.40 MPa.....140

Figure 5.18: Applied stress against failure time with a constant pit depth142

List of Tables

Table 2.1: Statistical fitting of the observed corrosion data [12].....	53
Table 2.2: Scoring model for pipeline coating type [12]	54
Table 2.3: Regression coefficients for the maximum pit depth model [12]	55
Table 4.1: Parameter values for model calculations	93
Table 5.1: The input parameters of the model	127
Table 5.2: The constraints and loads for the model's geometry	128
Table 5.3: The working stresses of various sections of different circuits [3]	135

Abbreviation

MCM	Monte Carlo Method
PVC	Polyvinyl Chloride
PE	Polyethylene
AHI	Asset Health Index
SCC	Stress Corrosion Cracking
XCT	X-Ray Computed Tomography
SEM	Scanning Electron Microscopy
PDM	Point Defect Model
GEV	Generalized Extreme Value
CDF	Cumulative Distribution Function
FEA	Finite Element Analysis
FEM	Finite Element Method
CAD	Computer-aided Design
PDF	Probability Density Function
UTS	Ultimate tensile strength

Nomenclature

A	Surface area (m^2)
a	Pit depth (μm)
b	Inverse Tafel constant
D	Diffusivity for the population of the breakdown sites
\bar{D}	Average diffusivity of breakdown sites
D_{kl}	Deformation rate
d_{max}	Maximum pit depth (μm)
E	Young's modulus (GPa)
E_b	Critical pitting corrosion potential (V)
E_{cor}	Corrosion potential (V)
$E_{measured}$	Measured potential (V)
E_{rev}	The equilibrium potential or reversible potential (V)
E_{rp}	Repassivation potential (V)
F	Faraday constant ($C * mol^{-1}$)
G	Shear modulus (GPa)
G_k	Random number
H	Plastic modulus (GPa)
i	Current density ($A * m^{-2}$)
i_0	Exchange current density ($A * m^{-2}$)
I	Current (A)
K	Bulk modulus (GPa)
K_V	Electrochemical equivalent volume ($m^3 * (A * day)^{-1}$)
L	Distance (m)
M	Molecular weight ($kg * mol^{-1}$)
N_0	Total number of stable pits
$N_{mp,0}$	Total number of breakdown sites
n	Charge number

P_{nucl}	Probability of pit that would nucleate
P_{γ}	Probability of repassivation
p	Number of particles in a cluster
p_{crit}	Critical probability of failure
Q	Electric charge (C)
q_{α}	Hardening parameter
R	Gas constant ($J * K^{-1} * mol^{-1}$)
s_i	Deviatoric stress (MPa)
T	Temperature (K)
t	Time (day)
V_{crit}	Critical pitting corrosion potential (V)
x	Crack length (μm)
α	Anodic transfer coefficient
$\Delta\Phi_{\Omega}$	Ohmic potential drop (V)
κ	Conductivity ($A * (V * m)^{-1}$)
ΔK_{th}	Threshold stress intensity factor range ($Pa * m^{\frac{1}{2}}$)
ζ_{ca}	The flux of cation vacancies across the barrier layer at the breakdown site
ζ_m	The annihilation flux
τ	The dissolution time (day)
ξ	The critical areal concentration of vacancies
σ_D	Standard deviation
$\Delta\varphi$	Averaged electrical potential (V)
$\Delta\varphi_{cr}$	The difference between corrosion and repassivation potentials (V)
γ	Delay repassivation constant (day^{-1})
ρ	Density ($kg * m^{-3}$)
ΔH	Activation energy of the alloy ($kcal * mol^{-1}$)
σ	Stress (MPa)
σ_{mean}	Mean stress (MPa)

$\Delta\sigma$	Alternating stress (<i>MPa</i>)
ε	Strain
δ_{ij}	Kronecker delta function
s_{ij}^{∇}	Jaumann rate of deviatoric stress

Chapter 1. Introduction

This thesis explores the use of the Monte Carlo Method (MCM) to simulate the pitting corrosion process on reinforcing tin-bronze tapes of underground power cables and to predict the asset life of the tapes. In this chapter, a brief overview of the underground power transmission cable and its failure mechanisms is presented. As underground power cables are widely used, it is important to estimate cable service life to determine whether a cable is at relatively high risk of failure and needs to be replaced. Also, in the final section, the thesis objective and structure are outlined. The aim of this thesis is to illustrate the advantages and feasibility of using MCM to simulate the pitting corrosion process and expand the scope of MCM to cable asset life prediction.

1.1 Introduction to underground power transmission cables

Underground power cables are widely used in power transmission and distribution networks since they provide reliable and safe impact. Fluid-filled paper insulated metallic sheathed cables are well designed, and these fluid-filled cables have been installed for carrying high voltages (33 kV to 400 kV) in the UK since the 1960s [1]. A cable system includes cables, joints, and terminations. The components most susceptible to electrical failure are the joints and terminations. However, these items can be economically replaced, so the end of the working life of a cable system will normally depend on the condition of the cable.



Figure 1.1: Excavation of underground cables (<http://www.pier-uk.co.uk/category/vacuum-excavation/>)

The excavation of underground cables is shown in Figure 1.1. To investigate the cables, the soil above the cables needs to be removed so that the cables can be dug out. The construction of the cables is shown in Figure 1.2. The cable has a central oil duct inside a copper conductor which is designed to carry the load current. A metallised paper is used to wrap the conductor, creating a semiconducting screen that smooths the high electrical stress at the boundary of the conductor. The conductor is insulated from earth potential by continuous layers of paper tapes, which are infused with insulating fluid. This fluid controls electrical discharge by filling the voids, thereby improving the insulating properties of the paper. Copper-woven fabric tape acts as another semiconducting screen that is applied over the outer surface of the insulation. Then, a

seamless sheath is formed on the cable by extruding lead alloy in order to maintain the fluid inside the cable, and fault current can be reduced by the lead alloy forming an earth return. However, lead cannot withstand the internal fluid pressure of the cable owing to the properties of creep in the absence of external reinforcing tapes. Therefore, reinforcing tin-bronze tapes are wrapped over the lead sheath. These reinforcing tapes play an important role in ensuring the security of the cable. To provide protection from moisture, bitumen is applied over the reinforcing tapes, and the cable is finally given a polyvinyl chloride (PVC) or polyethylene (PE) oversheath. This oversheath insulates the lead sheath from the earth to enable cross-bonding of the sheath.

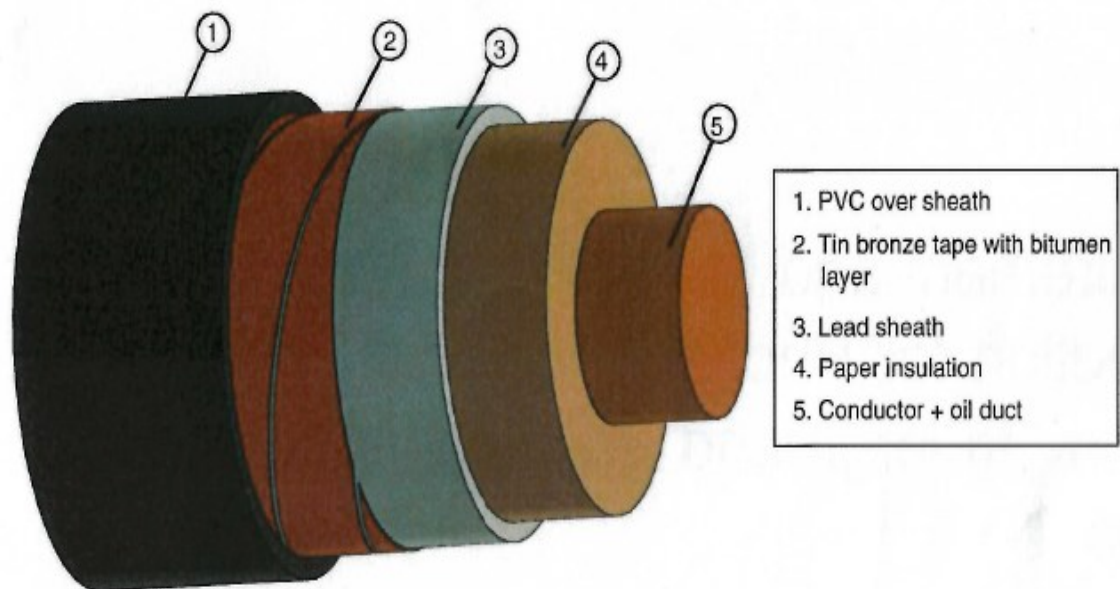


Figure 1.2: Construction of underground power transmission cable [2].

All high-voltage cables installed on the power transmission system are protected and insulated by an oversheath. From the mid-1950s to the mid-1970s, cables were usually manufactured with a PVC oversheath. Since the mid-1970s, PVC has been replaced with PE, which has better mechanical properties than PVC.

It is commonly assumed that cable installations should have a design life for more than 40 years. However, several leaks in the fluid-filled underground cables have been reported [2]. The fluid leak was caused by the splitting of the lead sheath. When the reinforcing tin-bronze tapes over the lead sheath were exposed to reduce the leak, a blue/green substance was observed on the tapes and the tapes had parted across their width. The majority of the substance was on the upper surface of the tapes, but it was also present on a smaller area on the lower surface of the cable. When the cable had been excavated to determine the fluid leak position, the oversheath was found to have distended. When the PVC was removed at these positions, the tapes were found to have split. It was also observed that the bitumen filling between the PVC and the reinforcing tin-bronze tapes was incomplete and the tapes were corroded in areas where the bitumen was absent. The sequence of events leading to cable failure is shown in Figure 1.3.

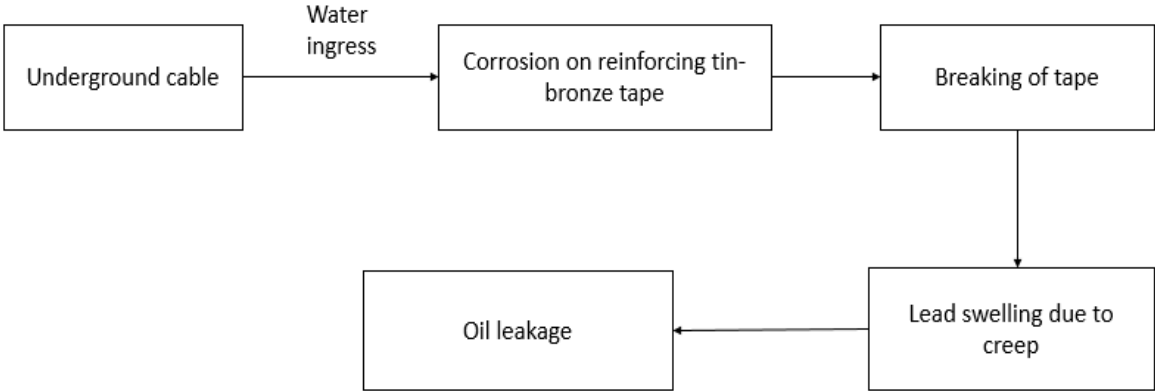


Figure 1.3: The sequence of events leading to cable failure

1.2 Failure mechanism of reinforcing tape

The main reasons that led to failure of the reinforcing tin-bronze tapes are illustrated below [1-3]:

i. Corrosion

Failure of the reinforcing tin-bronze tape was a result of pitting corrosion and corrosion fatigue initiated at the outer tape surface [1]. This was confirmed by the occurrence of multiple incipient cracks close to the fracture surfaces and by the presence of substantial corrosion products on the fracture surfaces. Copper alloys are widely used in underground cable applications because of the high resistance to corrosion. However, for the long-term underground cables, it was found that the degree of corrosion had a relation with the location of the pipe and the different conditions of the surrounding soil. As Foresta [1] pointed out, the damage of corrosion would be the maximum when the soil was silty sand which possessed properties like low water drainage rate, high moisture content and low resistivity.

ii. Moisture diffusion

Corrosion failure requires water to come into contact with the reinforcing tapes. In the absence of an oversheath fault, moisture can diffuse through the oversheath over a period of time. Using diffusion coefficient for water in PVC, it can be estimated that water can penetrate the polymer layer in 200 – 300 days.

iii. Mechanical stresses

It is important to look at both the static and transient pressures experienced by the cable sheath and the reinforcing tapes. Static pressure is a function of the profile of the cable and the ambient temperature. Transient pressures occur with changes in load on the cable and are due to the resistance of the fluid to flow through the duct to the pressure tanks as the cable heats up or cools down. The presence of such transient pressure will increase the hoop stress experienced by the reinforcing tapes under the static pressure. When there is uniform corrosion on the cable, then the fracture of the tapes firstly occurs at these corroded positions. However, fracture of the tapes at

positions of high static pressure can be expected to occur if they are extensively corroded and had not been controlled to transient pressures. Therefore, these applied mechanical stresses lead to the occurrence of stress corrosion cracking (SCC) or corrosion fatigue.

Overall, the reinforcing tin-bronze tapes of lead sheathed cables are susceptible to corrosive failure. Corrosion reduces the life of reinforcing tapes, which may fracture because of the hoop stress generated by the cable's internal oil pressure. When this occurs, the cable lead sheath expands, and the cable fluid leaks. As the earlier designs did not include a fabric binder tape over the reinforcing tin-bronze tapes, the reinforcing tapes of cables manufactured before 1973 were particularly susceptible to corrosion. This caused the bitumen moisture barrier to migrate from the tape surface easily, thereby allowing moisture to come in contact with the tape surface and initiate the corrosion process. Meanwhile, in earlier designs, cables were oversheathed with PVC and later designs employed polythene. It is known that moisture diffusion through PVC is much faster than through PE. Typically, for PVC, equilibrium is reached in about 200 days whilst for PE, the process can take about 330 days. Both of these timescales are short compared to the life of a cable, so whether the cable has a PVC or PE oversheath has little effect on the extent to which the cable reinforcing tapes will corrode. Also, given the effect of internal fluid pressure of the cable, corrosion fatigue plays an important role in accelerating the failure of reinforcing tapes as well [2]. The overall process of tape failure is shown in Figure 1.4.

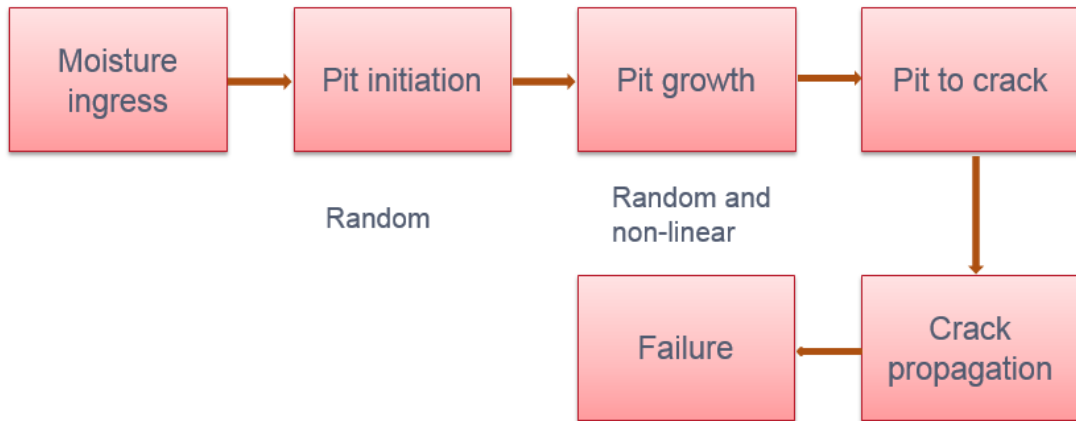


Figure 1.4: Tape failure process

1.3 Asset life of underground power cable

The underground power cables installed are expected to serve for long-term. However, because of the corrosion of reinforcing tin-bronze tapes, some oil-filled cables experience fluid leakage within 25 years. Therefore, it is necessary to forecast the expected life of cable systems so that a long-term capital programme can be developed. For a distributed asset, such as underground cables, the definition of “failure” and “life” can be problematic. Cable sections that are affected by tape corrosion will be assumed to have failed if the reinforcing tapes have broken.

Cable system replacement is programmed such that the elements of the cable systems are replaced when the safety, operational, or environmental risks of continued operation meet specific criteria. An Asset Health Index (AHI) is assigned to each cable circuit based on condition assessment, defect history, service experience, and history of similarly designed works.

It should be noted that the life assessment of any cable section with the AHI is based on a limited number of tape samples. These samples are taken from parts of the section

and hence may not be the most corroded part. Furthermore, life examination based on pit depth and the choice of the representative value for each tape sample has a significant value in life prediction. The above section provides information on the factors influencing the corrosion process and the effect of water in corrosion progression. All of these factors make remnant life prediction inaccurate.

When analysing cable replacement priority, locating the cable leakages can be difficult owing to the migration of the oil along the outer PVC oversheath resulting in widespread civil works, and extremely long outages are required to repair the cables. Meanwhile, cables are normally installed in urban areas, and failures in these cables are not only expensive to repair but also have wider impacts such as transport interruption, environmental contamination, etc. Whilst it is possible to quantify the level of corrosion, the eventual time to failure is determined by many factors. Not least among these is the shape of the corrosion pit and its susceptibility to crack progression both through the tape thickness and across its width. It should be noted that the predictions are based on an assumed uniform rate of corrosion progression and on the corrosion found being the worst for that section. All of these are substantial assumptions, and inevitably, some cables can be expected to fail earlier or later than the predicted dates. Scheduled maintenance and replacement can be effective for the prevention of cable failures in future; however, this requires considerable effort and expenditure and should only be done when absolutely necessary. Hence, a better asset life and asset deterioration prediction methodology is needed for reinforcing tape corrosion that will be beneficial for both asset management and system operation.

1.4 Application of prediction method for simulating pitting corrosion

In previous works [1-3], the reinforcing tin-bronze tapes were taken from different leaking cables to investigate the failure mechanism. The results of the investigation

showed that pitting corrosion was the main reason behind the failure of tapes. However, it took more than 1 year to investigate the corrosion rate and the pit depth. In other words, this kind of investigation is expensive and time consuming. Moreover, as the samples were taken from a few circuits and the relevant back fills were fairly simple, the results of the corrosion rate may not be accurate for different underground environments. Also, there are very few studies on the analysis of pitting corrosion of tin-bronze tapes, and most of the research is focused on aluminium alloy [4-8] and stainless steel [9-12]. In such a situation, there is no suitable model to analyse the pitting corrosion of tin-bronze tapes. Therefore, a more accurate and suitable model that can be widely used for most of the circuits is needed.

In order to predict cable service life, identifying the failure mechanism of the tapes and using an appropriate theoretical model available from literature are necessary steps. In underground environments, the most probable mechanisms of copper alloy failure are SCC and corrosion fatigue [13]. Gnanasambandam et al. pointed out that the failure mechanism of reinforcing tin-bronze tapes was corrosion fatigue [1]. In their work, they analysed failed tin-bronze tapes and found that corrosion fatigue was the failure mechanism. 2D and 3D optical microscopy and SEM were used for the detailed examination of the tape samples. The SEM images illustrated that the pits occurring on the surface could be the starting point for the crack that finally led to failure. Stress calculation in their work illustrated that the reinforcing tape could fail only if corrosion pits occurred on the tape surface. Therefore, occurrence of corrosion pits, multi cracks, and striations on the fractured surface indicates corrosion fatigue cracking as the failure mechanism across the tape samples.

SCC fracture of reinforcing tapes only occurs when they are exposed to a specific substance with a part of tape containing a micro-crack and loaded beyond the critical minimum stress [14]. However, according to Gnanasambandam's research, the samples were taken from different circuits under the combined effect of localised environmental corrosion and corrosion fatigue due to the cyclic pressure from the oil. Thus, in this

research work, the failure mechanism of reinforcing tapes was corrosion fatigue. The result of investigations of different circuits of underground power transmission cables indicated that most of the failed cables faced several corrosion problems, and the most common problem was pitting corrosion. The pits transformed to cracks that propagated and led to the failure mechanism of corrosion fatigue. However, pitting occurs randomly on the surface. The pit depth is also random and cannot be predicted accurately. Hence, the models used to predict pit depth are very important. Many researchers are working with corrosion models, such as empirical, experimental, mechanistic, and stochastic models. However, each model has its limitations in modelling pit depth, given the presence of uncontrollable factors. Alloy composition, microstructure, temperature, and composition of the surrounding media are all involved in the pitting process as variables of the metal-environment system [15].

As already stated in the above sections, the life of an underground power cable is greatly reduced by pitting corrosion of the tin-bronze tapes, so an accurate computational method is required to predict the growth of pitting depth. In the present work, the phenomenon of pitting corrosion is explored using several samples of tin-bronze tapes that have been in service for different circuits of underground power cables for 45 years. It is necessary to measure pit depth, as only a small part of the long cable can be experimentally analysed. Many methods and tools have been found in previous studies for estimating pit depth, mainly for ferrous materials or aluminium alloys. Magnetic flux leakage is used in a data fitting work for steel [16]. X-Ray computed tomography (XCT) or scanning electron microscopy (SEM) can be used to observe single pit morphology. The majority of the research deals with the pit growth problem, where the deepest pit is known to cause failure [17]. Moreover, measurement tools are usually available for relatively large pits ($>100\ \mu\text{m}$). In contrast, for the reinforcing tin-bronze tapes, the pits of interest are very small ($<100\ \mu\text{m}$) and filled with corrosion products. For these reasons, metallographic examination is suitable for pit depth measurement of the tapes because it can overcome the problem of corrosion products whilst providing the pit depth in a systematic way.

Many theoretical studies have illustrated prediction models of pit depth with time increasing [18-19]. To predict pitting corrosion, one model predicted the time dependence of pitting depth and rate [15]. This model considered the chemical and physical properties of the soil and pipe. However, the data used for analysis were collected from more than 250 excavation sites over 3 years. The limitation of this model is obvious. If the conditions change, the results of the prediction will not hold true. Another model was built according to the mechanism of pitting growth [20]. This mechanism model used Faraday's Law and pit morphology to determine the relationship between pitting depth and pit growth period. However, in this prediction model, all the pits continued growing. As the mechanism of pitting corrosion shows, the propagation of pits can stop at any time because of repassivation. Therefore, the results of the mechanism model may not be accurate. Most of the models have some limitations. The mechanical model considers several mechanisms of pitting corrosion and treats environment (temperature) factors as parameters, but it does not consider the mechanism of passivation or repassivation. Passivation or repassivation is an important factor when determining whether pits continue to grow or not at a certain time during the whole pit growth period. The empirical model is simply based on the equation $d_{max} = kt^v$ and probabilistic and statistical techniques [17, 21-28]. In order to use this model, a huge amount of pitting corrosion data is required. Moreover, much experimental work is also needed, which could take several years to complete. Also, this method cannot be used widely for predicting pit penetration as the pitting corrosion data has geographical and environmental restrictions. For pitting corrosion, the Monte Carlo simulation is a more accurate prediction model [29]. This model solves the problems of other models. The Monte Carlo simulation is based on random numbers or random conditions. Thus, the results of the prediction can be shown as a probability distribution function. With the Monte Carlo simulation method, pitting depth can be predicted accurately. The results can be used to determine the probability distribution function of the maximum pitting depth with time increasing. Therefore, the time of failure of tin-bronze can be predicted. In addition, one can forecast the requirement for repair or replacement of the tin-bronze tapes because of pitting corrosion.

1.5 Research objectives and thesis layout

The overall aim of this research was to develop an efficient computational model of the MCM in order to simulate the pitting corrosion process of reinforcing tin-bronze tapes and predict an underground power transmission cable's life. The computational model could provide an insight into the mechanisms of pitting corrosion, including pit nucleation, pit propagation, and pit repassivation. This model could also accurately predict the asset life of reinforcing tapes. This information could help reduce the influence of indefinite parameters, especially environment and soil conditions. The FEM simulates stress analysis with various applied stresses to identify the failure level of different critical pit depths on reinforcing tapes. The FEM could provide a criterion for the failure of cables, which could determine the "at-risk" level of underground cables that is not solely dependent on the critical pit depth of reinforcing tapes. This aim was achieved through the following objectives:

- Investigate computational models for simulating pitting corrosion behaviour with the MCM
- Critical review of pitting corrosion data gained from the National Grid and experiments to present the complete set of data; using these data to illustrate pit depth distribution of various cables without applying any statistical model
- Develop an efficient computational model to predict the distribution function of pit growth by reducing the influence of uncertainty
- Using the model to perform a series of studies to understand the severity of pitting corrosion in reinforcing tapes from different cables and then predict the asset life of the cables
- Using the FEM to analyse the effect of critical pit depth on reinforcing tapes with the cable's internal pressure

Research work presented in this thesis benefited from published mathematical models and data by a research team at University of Leicester in particular articles [1-3].

A description of the content of each chapter is presented below.

Chapter 2 – Literature review

This chapter presents the findings of the literature survey conducted to identify the relevant research on the mechanisms of corrosion, particularly pitting corrosion, and the techniques developed for modelling pit growth process. Firstly, a general summary of the mechanisms of pitting corrosion is presented, followed by an overview of the mechanisms of corrosion. The factors that influence the pit growth process are examined in detail with the related theories. Then, the literature survey on the techniques developed for modelling pit nucleation, pit propagation, and pit repassivation is presented. The MCM is introduced to model the pit growth process with mechanisms of pitting corrosion. The modelling approaches capture the pit depth distribution and pit growth rate for different materials in various environmental conditions. Finally, the mechanisms of corrosion fatigue are introduced to illustrate the failure process with pitting corrosion and applied stress on the materials.

Chapter 3 - A critical analysis of pitting corrosion data of underground power transmission cables

In this chapter, experimental data obtained from open literatures and University of Leicester research group on pitting corrosion are presented. Using these experimental data, a comprehensive understanding is presented without any analytical models. The results from the experimental data are then compared with the results from an analytical model to verify the consistency of these 2 sets of pit depth distribution results.

Chapter 4 – Monte Carlo model of pitting corrosion

In this chapter, the material properties of reinforcing tin-bronze tape are described and used for simulating the computational model of pitting corrosion. The MCM is added to the computational model to reduce the uncertainties of influencing factors. In addition, Newton's method is added to the computational model as a root-finding method in the pit propagation stage and a random number is added to make pit repassivation with time stochastic.

Moreover, in this chapter, the experimental data and computational data are comparatively analysed. Firstly, the computational data are examined using the empirical models and experimental data. A set of parameters used in the computational model are tested with various values to get the best fit with the experimental results. Then, the computational model is validated by a set of experimental results. As each set of experimental data has its own working environment conditions, the parameters used for determining the pit growth probability are described as a range of values.

Chapter 5 – Plastic deformation around representative pits in failed cables

In this chapter, a failure model with pitting corrosion is introduced. Then, an FEM is built with COMSOL software and the relation of pit depth and applied stress is illustrated by using this COMSOL model.

In addition, the failure mechanisms of reinforcing tin-bronze tape are further investigated independently. The study looks at the effect of pit depth and applied oil internal pressure on cable life prediction. In addition, the probability of failure is described based on the critical pit depth on the surface of reinforcing tapes. The time

to failure is analysed to obtain a set of relationships with the applied stress and the value of critical probability of failure.

Chapter 6 – Conclusions and recommendations for future work

A summary of significant conclusions obtained from the research work is presented in this chapter. Then, recommendations for future work and suggestions for improvements in further research are made in light of the results of this work.

Chapter 2. Literature review

As corrosion widely occurs in materials and leads to the failure of engineering structures, it is important to identify the process of corrosion and prevent its occurrence. Pitting corrosion, which is a form of localised corrosion, commonly occurs in underground cables and leads to the failure of reinforcing tapes. Further, pitting corrosion can combine with stress, leading to SCC or corrosion fatigue. This kind of mechanism accelerates the failure of reinforcing tapes and reduces the service life of cables. Therefore, a model for predicting cable life is an important requirement to determine when the cables will reach the “high-risk” probability for failure.

2.1 Mechanisms of corrosion

The most common reason behind material degradation is chemical intervention; materials can continue degrading without the influence of mechanical work. Material degradation by chemical intervention consists of reversion of metals to reach chemical equilibrium. A variety of chemical reactions play a role in material degradation. The most significant types of chemical reactions in material degradation are shown schematically in Figure 2.1.

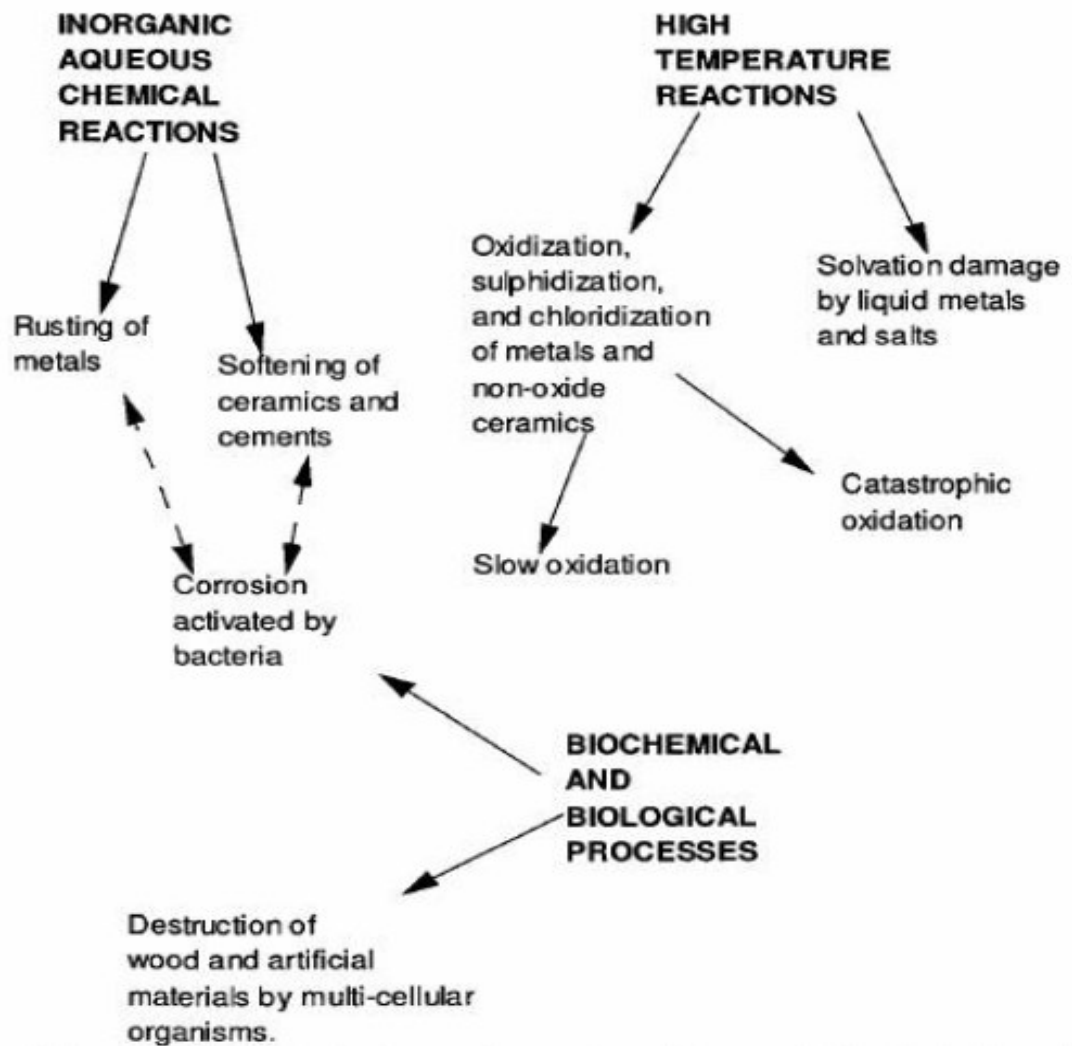


Figure 2.1: Relationship between various forms of chemical degradation of materials

[14]

Degradation due to chemical intervention can be categorised as follows: aqueous, high-temperature, and biochemical or biological degradation. Aqueous degradation involves loss of metals by water, salt water, or acids, which are normally present as rust or in a dissolved state. Certainly, non-metals can also be damaged by water and acids, especially strong acids with high dissolution speed. High-temperature corrosion is common for metals under high-temperature conditions. This type of corrosion is a form of burning although the oxide layers formed on the surface of the metal act as a protective layer to prevent sharp destruction of the metal. Metals and some non-metals

can also be damaged by destructive solvents that contain molten metals and salts. Biological corrosion, as the name implies, is caused by biological organisms. These organisms use solid materials as food. Also, corrosive excretions of organisms can destroy wood and artificial materials. Considering the economic costs, aqueous oxidation of metals at normal temperature and dry oxidation of metals at high temperature are the main forms of material degradation by chemical intervention [14].

Under normal temperature, the metals undergo slow destruction by aqueous corrosion or electrochemical corrosion. These destructions normally occur on the surface of the metals and lead to failure. Chemical corrosion is the result of oxidation of the materials when they react with chemical gases in a dry environment. In this type of corrosion, the metal is attacked by gases like oxygen, resulting in the formation of a solid film, which is the corrosion product, on the surface of the metal to maintain it for further corrosion reaction. The corrosion observed in galvanic cells is called electrochemical corrosion. In a galvanic cell, an electrolyte, which is normally water, is needed to ensure the flow of ions in the cell as a circuit. It is known that once a galvanic cell is formed, there are 2 different electrode potentials in that cell. Therefore, current is generated in the circuit during electron flow from the anode to the cathode. The metal atoms lose their electrons to the electrolyte and become positive ions in the anode area. This reaction is called oxidation. Hence, corrosion always occurs in the anodic area [30].

Pitting corrosion is the most general form of electrochemical corrosion. Pitting is a localised corrosion which is caused by localised failure of a passivating surface film, and tiny areas of the metal surface become exposed to a corrosive environment that continues corroding the metal. When a pit nucleates on a metal surface, the pit acts as an anode to the surrounding surface, and the remainder of the metal surface acts as a cathode. Inside the pit, rapid corrosion makes the pit wider and deeper. In this situation, even if the opening area of the pit is relatively small, the corrosion of the metal becomes possible on a wide-ranging subsurface. Pit nucleation is defined as the initial stage of pit

construction in an unbroken passivating film. The next stage of pit growth is called pit propagation [14]. The electrochemical potential of a metal surface plays the most important role in pitting corrosion. Pitting potential is the minimum potential for pitting, and pitting does not occur in the presence of corrosive mediums if the electrochemical potential is lower than the pitting potential [31].

Crevice corrosion is another form of localised corrosion. Crevice corrosion can reach the propagation stage from the crevice stage, whereas pitting corrosion can occur only after the initial stage of pit nucleation. In crevice corrosion, the crevice is treated as the anode and the surrounding exposed metal, the cathode. Nuts and bolts that play important roles as engineering components can be corroded inside closed spaces, which cannot be seen from the outside, by crevice corrosion and fail. Crevice corrosion is an extremely significant cause of corrosion fracture and failure [14].

2.2 Mechanism of pitting corrosion

Pitting is localised corrosion that can easily occur on a metal surface where there is (a) a scratch or mechanically caused break in a protective film of the surface or (b) applied or residual stresses leading to dislocation or slip step. Unlike crevice corrosion, which is initiated by differential concentrations of ions or oxygen in the electrolyte, pitting corrosion is initiated by metallurgical factors on plane surfaces [32]. Many studies are looking into the detailed mechanisms of pitting, especially the initiation of pits [33-35].

The mechanism of pitting corrosion is illustrated clearly by Landolt [36]. Metals form a thin oxide layer that separates the metal from its environment at the surface. These kinds of metals are called passive metals and the oxide layer is called passive film. In contrast, active metals are film free. Pitting corrosion requires the existence of aggressive anions, which are chloride ions in most cases of corrosion, and of an oxidising

agent, such as oxygen or ferric ions. A corrosion cell forms between the anode and the cathode. In this kind of a corrosion cell, the anode is the growing pit and the passive surface surrounding the pit acts as the cathode. In pitting corrosion, a passive metal is attacked by the localised corrosion, resulting in the growth of small pits. Pitting corrosion always occurs on a metal plate or pipe wall and eventually leads to perforation with the increase in pitting depth. Therefore, pitting corrosion can be destructive although the amount of corroded metal is small. Three typical pit shapes are shown in Figure 2.2: (a) crystalline attack can lead to deep, narrow pits, (b) occluded pits can be formed under a cover consisting of corrosion products or non-corroded metal, and (c) a smooth surface leads to hemispherical pits. Pitting corrosion also requires the action of aggressive anions, which are often chloride ions.

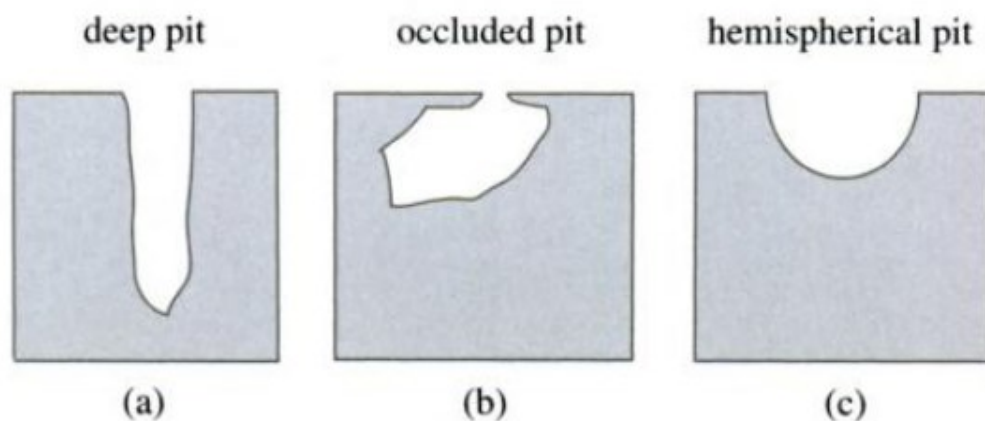


Figure 2.2: Shape of corrosion pits: (a) deep narrow pit, (b) occluded pit, (c) hemispherical pit [36]

Burstein et al. [37] pointed out that the process of pit nucleation is unstable as pits may not be able to reach the stage of propagation. Nucleation current may reach zero continuously and most pit nucleation events are suspended. If the pit shows nucleation, then the pit growth is considered to be metastable. In such a case, continued survival relies on preservation of an effective barrier to diffusion supplied by a perforated cover of the corrosion product over the pit surface. Also, when this kind of cover is missed,

but the pitting current density is not high enough, pitting is terminated at this stage. If the pit survives the metastable phase, then stable pitting occurs. This stage is diffusion controlled and the diffusion barrier relies on the pit depth.

During pitting corrosion, metals can be in 2 different states: active state and passive state. When metals reach the passive state, a thin oxide layer, called passive film, is formed on the surface, and it separates the metal from its environment. Metals are film free in the active state. Owing to the presence of an oxide film, the dissolution rate of a passive metal is extremely lower than the dissolution rate of an active metal when a particular potential is given. Generally, there are 3 distinct potential regions in the polarisation curve of a passivating metal (Figure 2.3): (a) the active region, (b) the passive region, and (c) the transpassive region. Unlike the active and passive regions, the surface state of the metal in the transpassive region is not well defined and an oxide film may not be covering the surface [36].

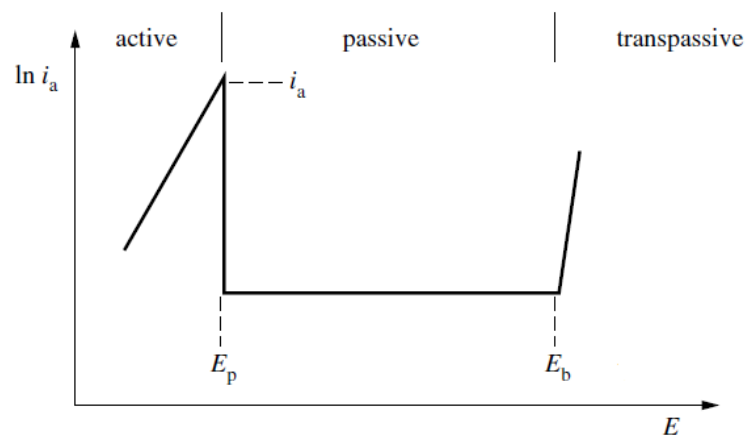


Figure 2.3: Variation in partial anodic current density with potential for a passivating metal [36]

Figure 2.3 illustrates the variation in the anodic partial current density on a passivating metal as a function of the potential. The passivation potential E_p insulates the passive metal from the active potential region. The transpassivation potential E_b defines the end of the passive potential region and the shift from passive to transpassive behaviour. When pitting corrosion occurs and the oxide layer undergoes dissolution during pit nucleation, the potential E_b is called pitting potential or critical pitting potential. In general corrosion, potential E_b is referred to as film breakdown potential, which means the oxide film is penetrated by aggressive ions [36].

According to Landolt [36], pitting corrosion takes place when the corrosion potential (E_{cor}) is greater than the critical pitting potential E_b , and this indicates that metal dissolution by pitting is the controlling reaction. In addition, E_b is also called as film breakdown potential, implying that passive film breakdown is the initiation of pitting. If $E_{cor} < E_b$, passivity is stable; otherwise, pitting corrosion occurs (Figure 2.4). Also, as Macdonald and Engelhardt [38] pointed out, the models must assume that $E_{cor} > V_{crit}$; otherwise, pitting corrosion cannot be initiated.

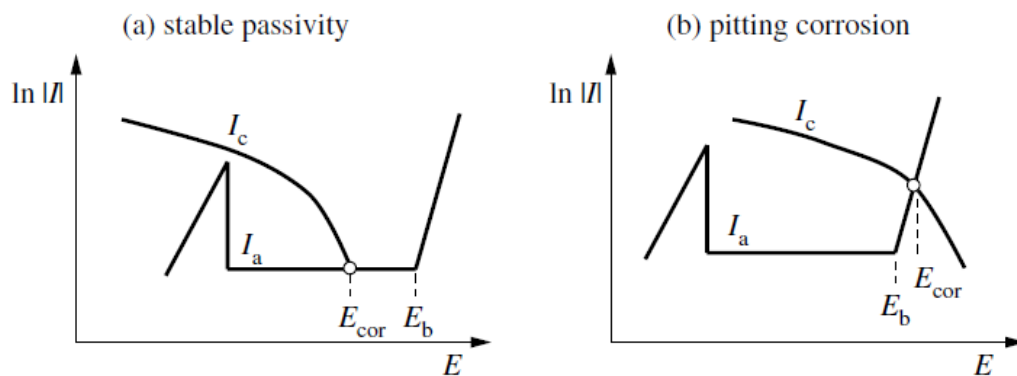


Figure 2.4: Evans' diagram of a passive electrode showing sensitivity to pitting corrosion: (a) $E_{cor} < E_b$; (b) $E_{cor} > E_b$ [36]

To determine the critical pitting potential, the potentiodynamic method is used. In the potentiodynamic method, with the increasing anodic potential, many inclusions and precipitates are generated. These generated products can become electrochemically active and then start to dissolve, enabling pit nucleation. After pit nucleation, the reaction can follow 1 of 3 different paths: the pit may immediately passivate (repassivation), it may repassivate after growing for a period of time (metastable pit formation), or it can form a stable pit that keeps growing for a long period of time (stable pit growth) [38]. Microelectrochemical methods have been found to be especially useful in the study of these appearances [39-40]. Generally, pitting corrosion of engineering metals and alloys involves 3 aspects [41]:

- Pit nucleation
- Metastable pitting
- Stable pit growth

2.2.1 Pit nucleation

The mechanism of passive film breakdown leading to dissolution by pitting is extremely important. It has been recommended that passive film loss leading to localised pitting corrosion in metals results from a variety of different mechanisms [42]. The penetration mechanism, the film breaking mechanism (Figure 2.6) and the adsorption mechanism (Figure 2.7) are studied by most researchers [43-45].

The penetration mechanism (Figure 2.5) includes the transfer of anions through the oxide film to the metal surface where they start their particular action. Aggressive ions penetrated the oxide film and followed their adsorption onto the film surface. For these ions (Cl^- , Br^- , I^-), Cl^- ions were found more aggressive than other two kind of ions because of the smaller diameter, and subsequent ability to penetrate the oxide lattice more easily. With such aggressive ions add to the film and leads to higher ionic conductivities along the penetration paths, the penetration process is auto-catalytic.

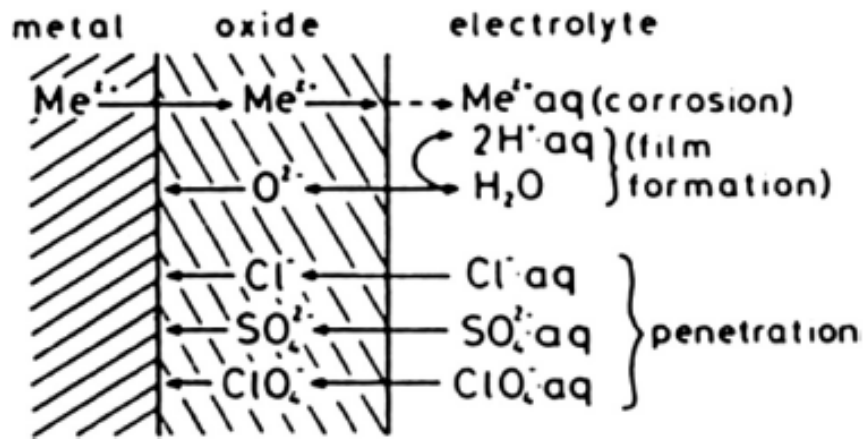


Figure 2.5: Penetration mechanism and phase diagram of a passive film with related processes of ion and electron transfer within the film and at its phase boundaries [43]

The film breakdown mechanism (Figure 2.6) requires the failure film which give direct access of aggressive anions to the unprotected metal surface. The surface tension of the passive film is reduced by adsorption of aggressive anions, and after that cracks would arise and then allowing anions to reach the metal surface. The role of aggressive anions (Cl^- ions) is to increase the electrostatic pressure and reduce the compressive strength of the film. Before the micropit reaches to a critical depth, the pit initiation could be treated as a repeated breakdown process. In the absence of aggressive anions, defects of the passive film would be healing quickly. However, in the presence of aggressive anions and at satisfactorily high potentials, the metal surface becomes activated.

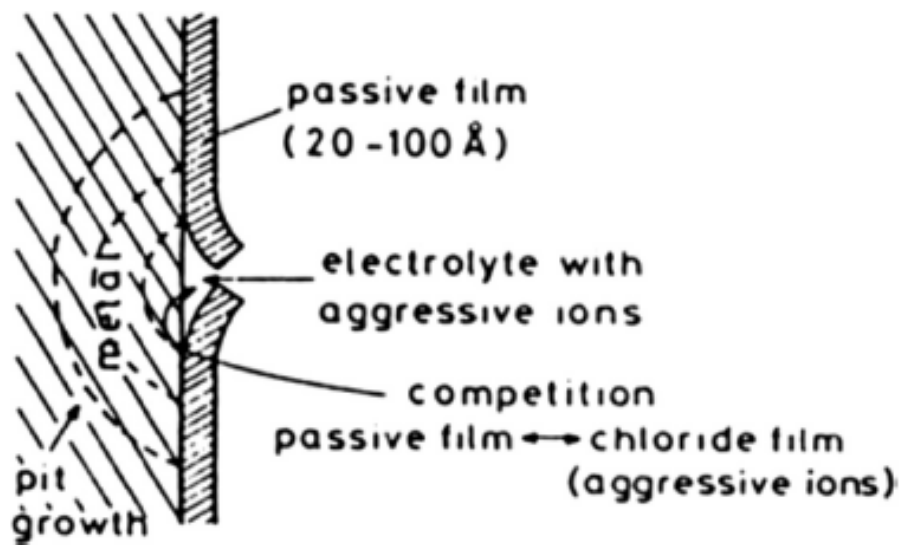


Figure 2.6: Mechanical film breakdown mechanism and related competing processes

[43]

The adsorption mechanism (Figure 2.7) assumes that the adsorption of aggressive anions at the oxide surface leads to improve the transfer of metal cations from the oxide to the electrolyte. This mechanism is based on localised formation of temporary complexes to create pits with metal cations. The passive film is a layer of adsorbed oxygen and the pits occur at the places where aggressive anions replace the oxygen. As Soltis [43] pointed out, localised adsorption of Cl^- ions cause to an enhanced oxide dissolution at these places and the oxide film becomes thinner until complete film removal and active dissolution.

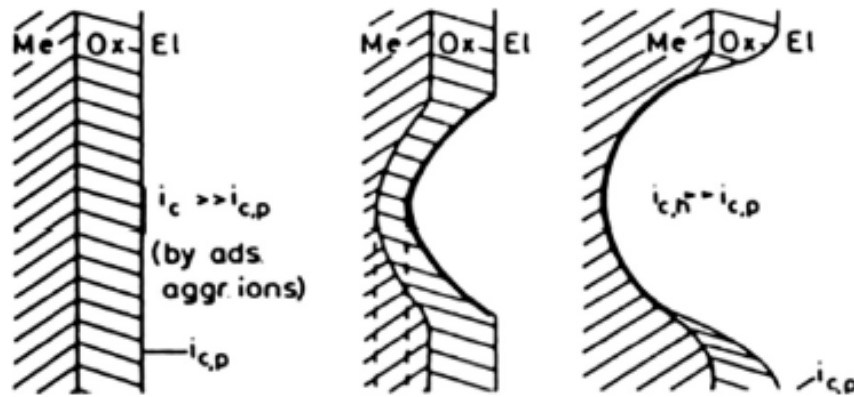


Figure 2.7: Adsorption mechanism with increased local transfer of metal ions and related corrosion current density caused by complexing aggressive anions leading to thinning of the passive layer and increases in field strength and final free corrosion current density within the pit [43]

2.2.2 Metastable pitting

According to Alvarez and Galvele [46], the formation of a stable pit is improved by electrochemical noise. Each of these electrochemical noise events initiates from the formation, growth and repassivation of a tiny pit. Such short life pits are indicated as metastable pits which can form at potentials much below the pitting potential and during the sense time before the initiation of stable pit at potentials above the pitting potential. Metastable pits grown on metal are covered by a layer which remains of the passive film. The failure of the covers leads to the dilution of the local pit environment and repassivation of the pits.

Metastable pitting temporarily displayed in chloride solutions have a characteristic shape (Figure 2.8). The current increases above the initial passive current as the pit nucleates and begins to grow. After a very short growth time period, the metastable pit repassivates and the current immediately reduces to the level of the original passive

current. There appear to be no noticeable differences between metastable pit growth and the early growth of a stable pit. Thus, studies of metastable pits were performed to gain understanding of the critical factors which can define the stable growth of pits. As Alvarez and Galvele [46] pointed out, metastable pit growth is controlled by the Ohmic resistance of the pit cover. Pits repassivated when their cover failure and the Ohmic barrier was lost. On the other hand, pit stability is retained if a salt film is present when the cover breaks.

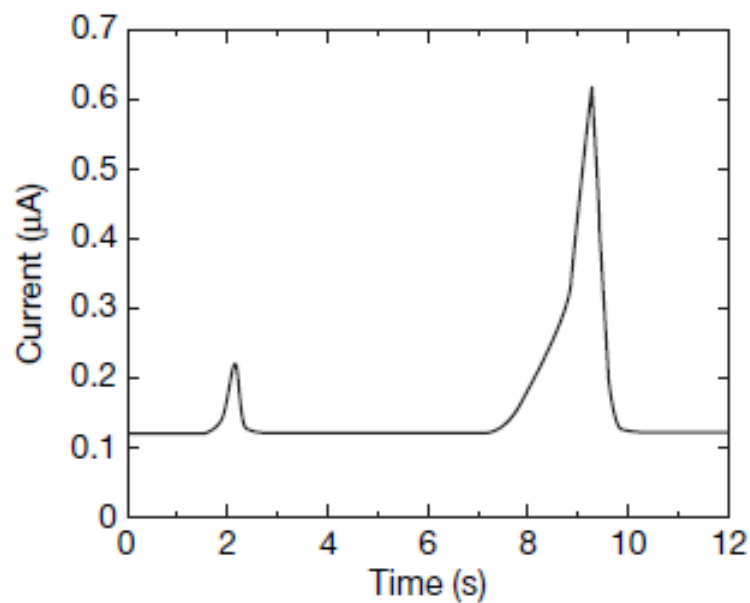


Figure 2.8: Current transients typical of pre-pits [46]

2.2.3 Pit propagation

During pit growth, chloride ions accumulate in the pit by diffusion in order to maintain electric balance in the presence of dissolving metal ions. In addition, dissolving metal ions undergo hydrolysis reactions, lowering the pH inside the corrosion pit:



An explanation for the existence of a pitting potential value with an acidification process is illustrated by Figure 2.9. The E-pH equilibrium diagram for Cu-H₂O is used to explain pitting of copper in chloride solutions. Above the potential E_1 the anodic reaction of the metal begins as Equation (2.1) leading to localized acidification. Locally reduced pH and high chloride concentration make repassivation of a growing pit difficult. When the pit grows, the chemical combination of the electrolyte inside the pit becomes increasingly aggressive. Therefore, pitting corrosion is an autocatalytic process, which means the pit itself creates conditions that approve its further growth once a stable pit is formed.

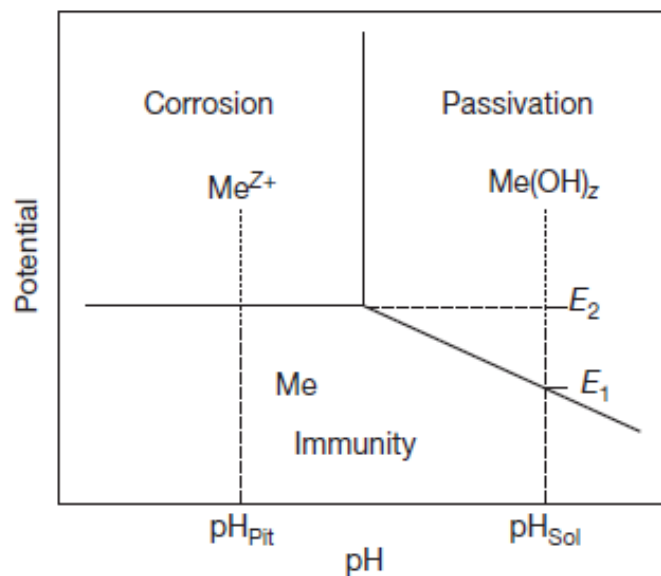


Figure 2.9: Explanation of the nature of E_p . Pits became stable only at potentials above E_2 [46]

This observation can be explained by the autocatalytic nature of pit growth, assuming the solution inside a pit approves its repassivation. Therefore, open pits repassivate more easily than occluded pits, as per this observation. For the same reason, engineering structures are most vulnerable to pitting corrosion in situations involving a stagnant electrolyte as concentration gradients can rise, undisturbed by convection.

2.3 Factors influencing the pitting potential

As Landolt [36] pointed out, critical pitting potential is not a well-defined kinetic or thermodynamic quantity. Its value depends both on the kinetics of pit growth and repassivation and the rate of pit initiation. In addition, the measurement of the pitting potential of industrial alloys requires statistical analysis to determine the probability of pitting for a given potential. Regardless of these limits, pitting potential is a beneficial quantity for the characterisation of the susceptibility of metals and alloys to pitting corrosion. As a characteristic of the metal-environment system, the pitting potential depends on several factors:

- Microstructure of the metal and the chemical composition
- Appearance of inclusions
- Composition of the electrolyte, especially the concentrations of aggressive anions
- Temperature

2.3.1 Influence of alloy elements

As Alvarez and Galvele pointed out [46], the pitting potential of a metal could be extremely revised by the use of alloying elements. For stainless steels, the main idea is to find alloying elements that could result the highest possible pitting potential which then gain a very resistant alloy. The pitting potential increases with increasing chromium content, as shown in Figure 2.10 [47]. At a sufficiently high concentration of chromium, depending on the environment, pitting no longer occurs and uniform transpassive dissolution is observed. This change occurs at about 40% chromium concentration under test conditions, as shown in Figure 2.10. To improve the resistance to pitting corrosion, molybdenum is often added to stainless steel. Figure 2.11 shows the effect of molybdenum on the pitting potential of 2 different type of stainless steels in NaCl [48].

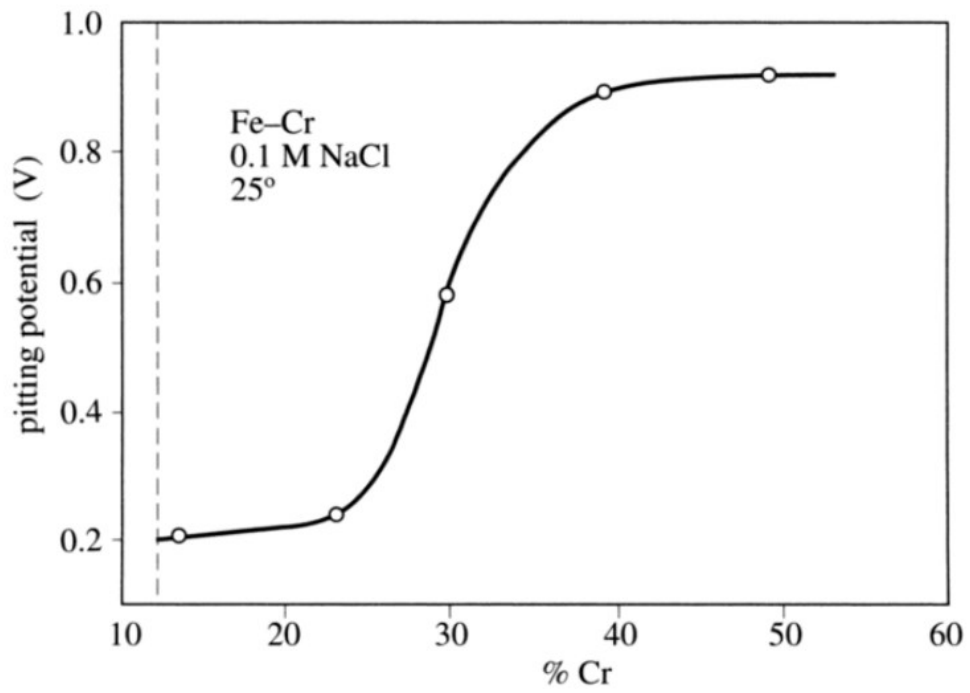


Figure 2.10: Pitting potential of Fe-Cr alloys as a function of Cr content [47]

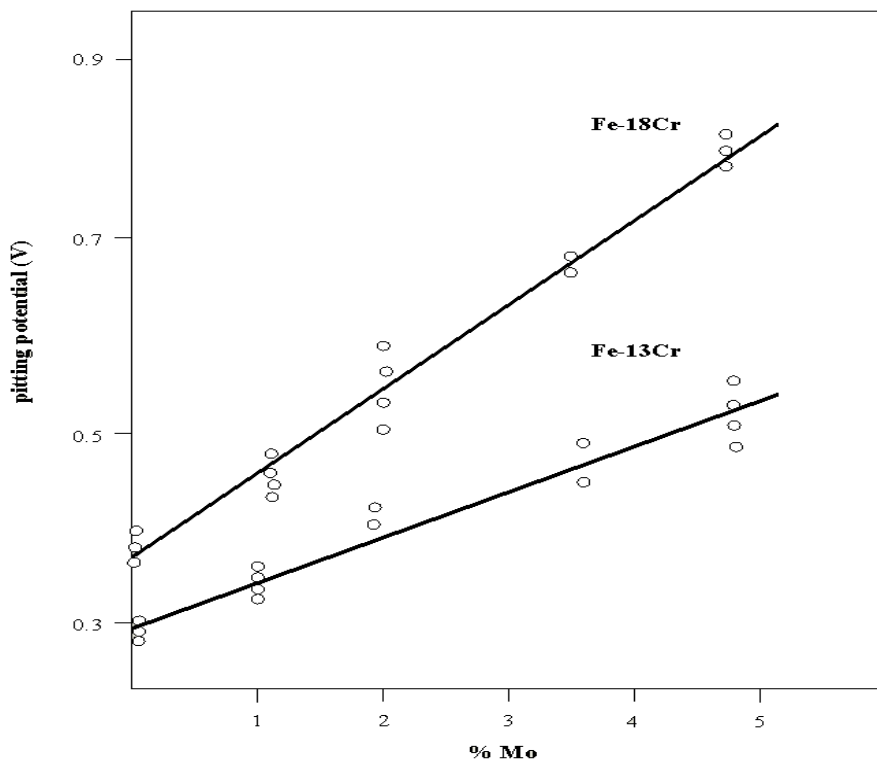


Figure 2.11: Effect of molybdenum on pitting potential of 2 Fe-Cr alloys in 1-M NaCl, at 25°C [48]

However, for aluminium, one of the technological ideas is to find an alloy with the lowest possible pitting potential in sea water which is for cathodic protection. For aluminium alloys with ~5% of the alloying metal, Figure 2.12 illustrates that copper increases the pitting potential of aluminium in chloride solutions, while magnesium has no effect and zinc decreases the pitting potential. Based on the research of Reding and Newport [49] and other researchers [50-51], their results could be used to have a rough estimate of the effect of alloying elements on the pitting potential of aluminium in sea water which is shown in Figure 2.13.

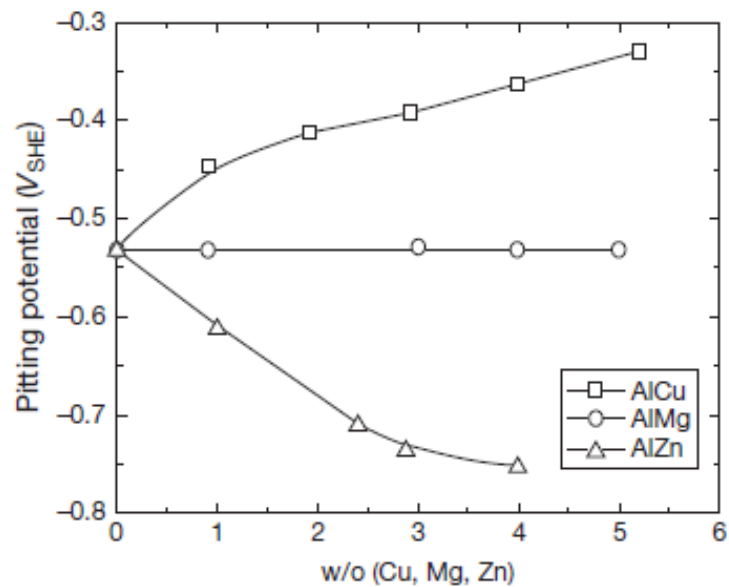


Figure 2.12: Pitting potential of binary Al-Cu, Al-Mg and Al-Zn alloys in 1 M NaCl solution [46]

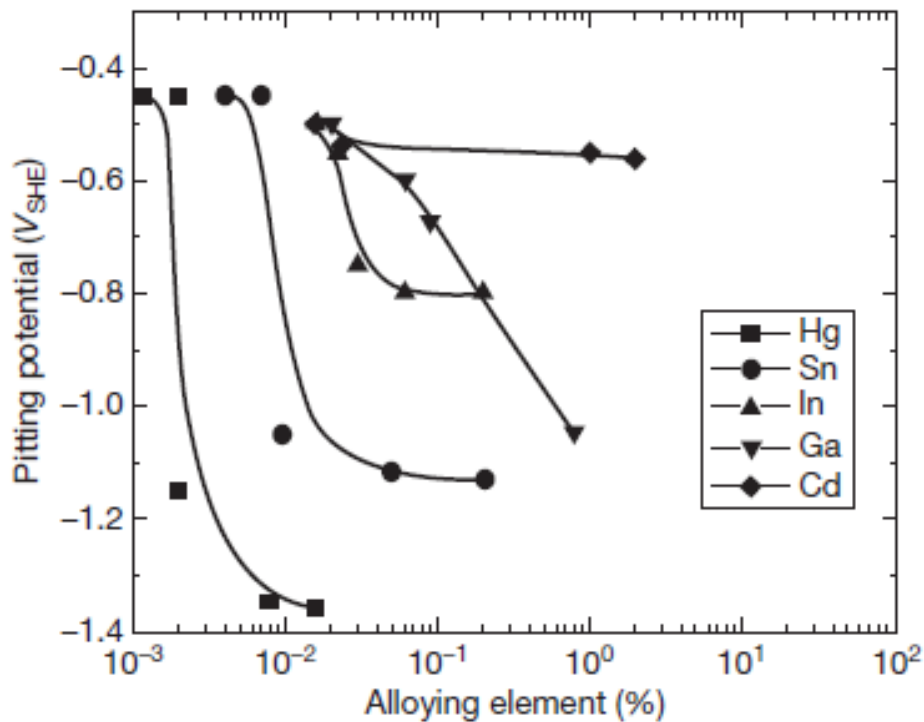


Figure 2.13: Estimated pitting potential values for binary aluminium alloys in sea water

[49]

2.3.2 Influence of inclusions

As Landolt [36] pointed out, industrial metals and alloys subjected to non-metallic inclusions, notably sulphides or intermetallic precipitates, almost always start to form pits. Therefore, the existence of inclusions or precipitates on a metal surface reduces the pitting potential. Figure 2.14 illustrates the anodic polarisation curves in HCl of 2 ferritic stainless steels, one of industrial grade and the other of high purity. It clearly shows that the high-purity alloy has a significantly wider passive section [52].

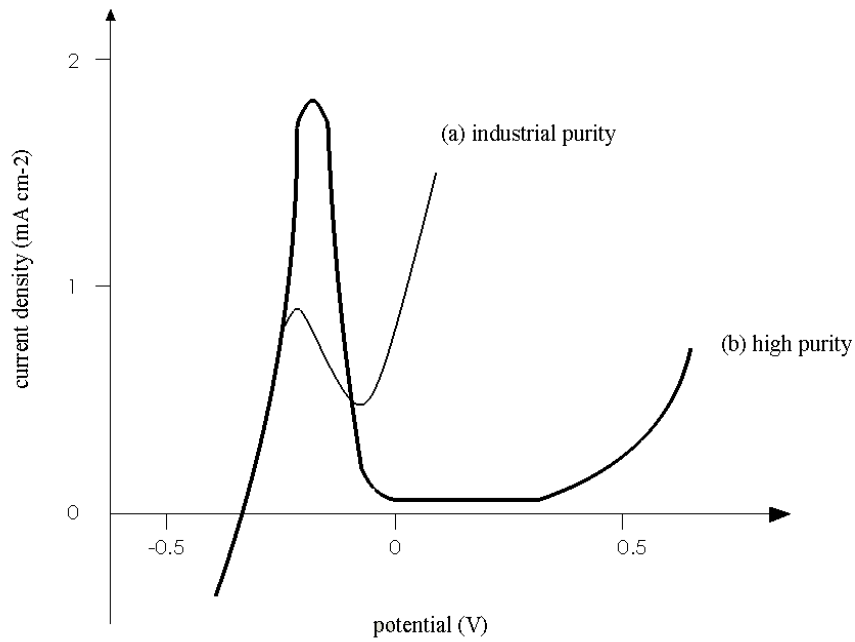


Figure 2.14: Anodic polarization curves of (a) industrial grade and (b) high-purity samples of Fe-17Cr in 0.12-M HCl, at 25°C [52]

Inclusions or intermetallic precipitates can expedite pit initiation and growth in different ways. Figure 2.15 illustrates the effect of inclusions that are anodic, cathodic, or inert with respect to the base metal. Electrochemical interactions do not occur between the base alloy and inert inclusions (a), but they still play a role in the initiation of pitting, and cracks can develop during quenching, something that happens between the inclusion and the matrix if the thermal expansion coefficients of the inclusion and the base metal are different. Consequently, a microscopic aeration cell (b) is formed. This cell then leads to the formation of a pit by undercutting through a crevice corrosion mechanism. Compared to the base metal, inclusions that are less noble become the anode of a corrosion cell and dissolve (c), and the pit nucleus is created. On the other hand, cathodic inclusions (d) approve the dissolution of the base metal in their immediate region. They finally fall off, forming a small pit on the surface.

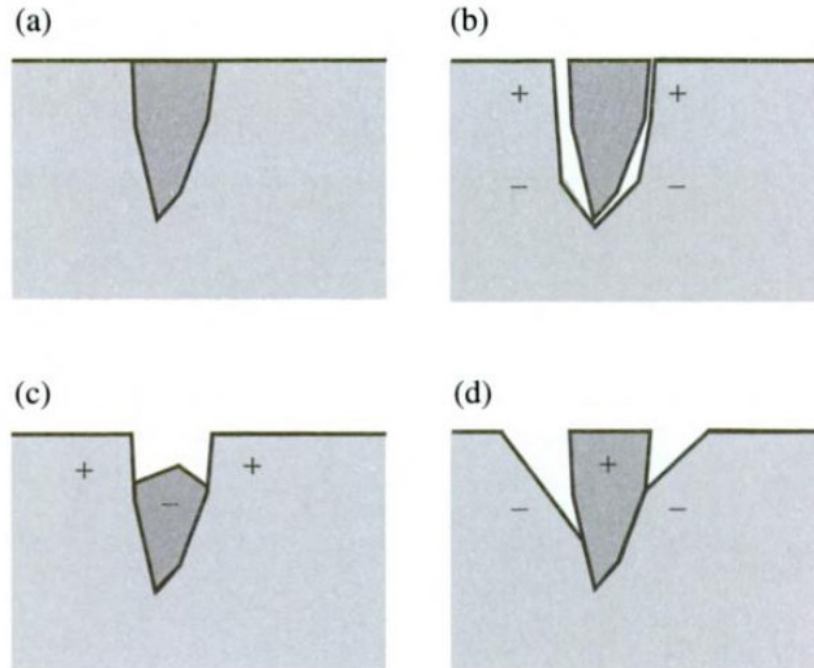


Figure 2.15: Effect of inclusions on pit initiation: (a) surface with an inclusion, (b) formation of an aeration cell in the space between an inert inclusion and the metal, (c) anodic dissolution of the inclusion, and (d) formation of a corrosion cell between the cathodic inclusion and the metal [36]

2.3.3 Influence of electrolyte composition

Generally, the higher the concentration of aggressive anions the lower the pitting potential. Figure 2.16 illustrates the variation in the pitting potential of copper as a function of the NaCl concentration in the electrolyte [53]. A relationship between E_b and the concentration of aggressive anions (Cl^-) could be written as:

$$E_b = A' - B' \log c_{Cl^-} \quad (2.2)$$

where A' and B' are constants. At ambient temperature, B' is about 0.1 V. In Figure 2.16, pitting potentials in 1-M solutions of NaBr, NaI and NaF are also shown for comparison. The pitting potential increases in the order $I < Cl < Br < F$ [53].

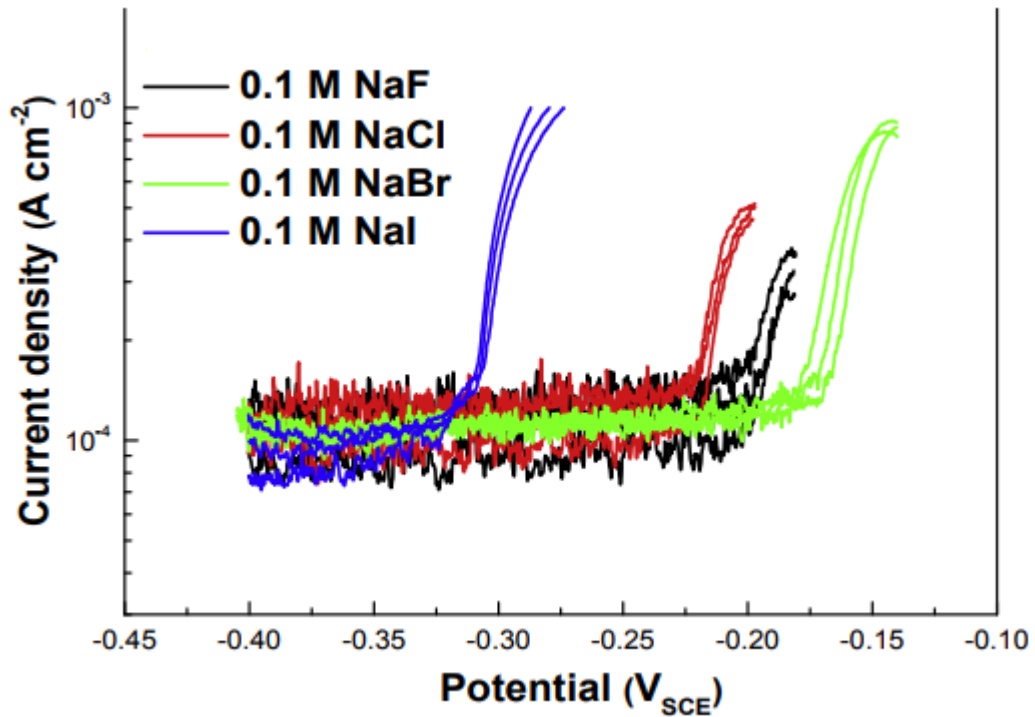


Figure 2.16: Effect of 0.1 M NaCl, NaBr, NaF and NaI on pitting potential of copper [53]

As Kong et al [53] pointed out, in the presence of both non-aggressive (OH^- , NO_3^- , SO_4^{2-} , S^{2-} , etc.) anions and aggressive (Cl^- , Br^- , I^- , etc.) anions, the pitting potential depends on the ratio of the 2 kinds of anions. For chloride-containing electrolytes, the relationship can be written as:

$$E_b = A' - B' \log \frac{c_{Cl^-}}{\sum c_i} \quad (2.3)$$

where $\sum c_i$ denotes the sum of non-aggressive anion concentrations. Figure 2.17 illustrates the potentiostatic polarisation curves in different aggressive and non-aggressive mixture solutions for copper. Figure 2.17 clearly shows that the pitting potential depends on the concentration of aggressive and non-aggressive ions.

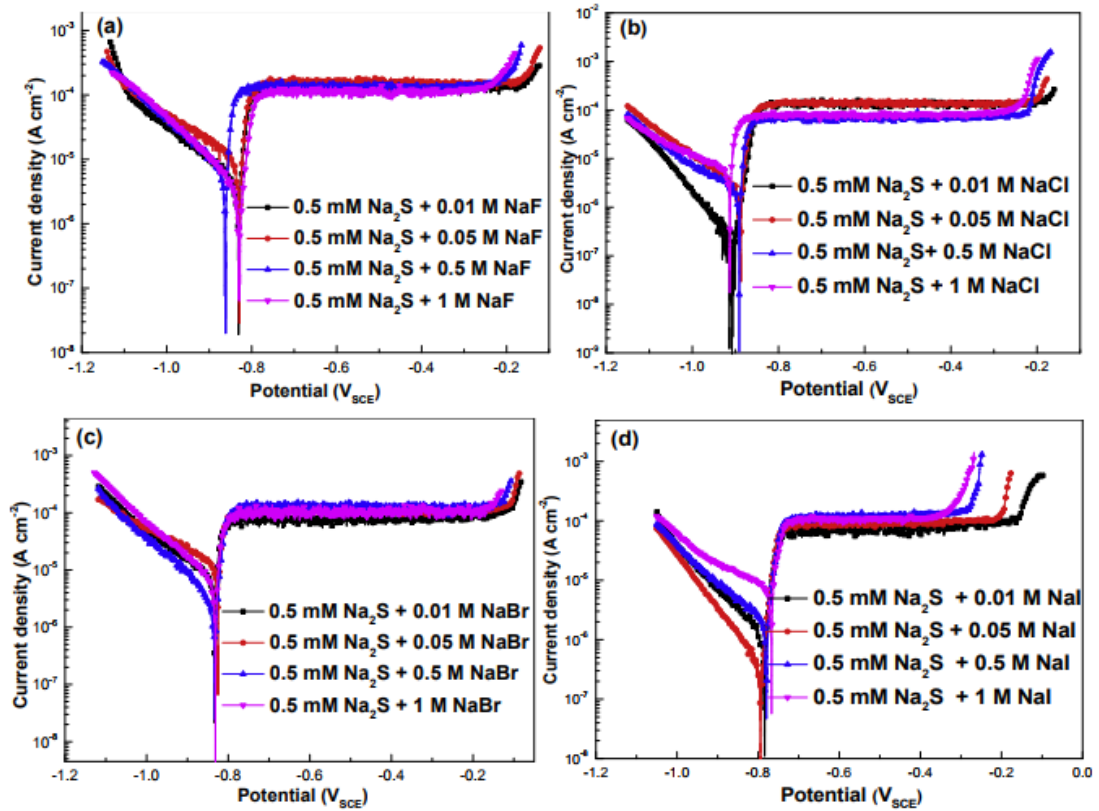


Figure 2.17: Potentiostatic polarisation curves showing the effect of electrolyte composition on pitting behaviour of copper exposed to aggressive and non-aggressive anions [53]

2.3.4 Influence of pH and temperature

Figure 2.18 illustrates that an increase in pH produced an increase in the pitting potential for iron in NaCl solutions which is found by Alvarez and Galvele [46]. However, as Kaesche [54] pointed out, the pH of the solution had no effect on pitting potential for aluminium in NaCl solutions, where the domain of pH values from pH 2 to pH 11.

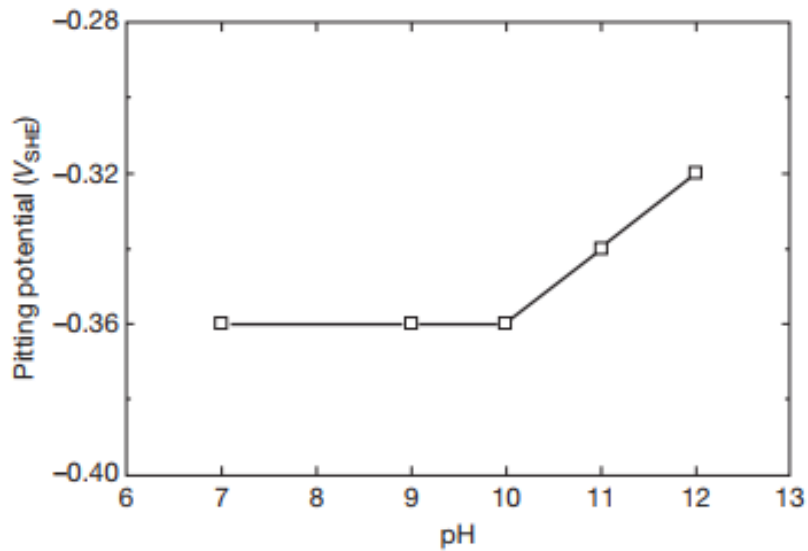


Figure 2.18: Pitting potential of high purity iron, in 1.0 M NaCl at various pH values

[46]

Pitting corrosion of stainless steel and other alloys is characterized by the existence of a critical pitting temperature (CPT), which is defined as the lowest temperature at which the growth of stable pits is possible. As Soltis [43] pointed out, no stable pits can occur at temperatures lower than CPT and only transpassive corrosion takes place, which as shown in Figure 2.19 [46]. Therefore, it can be concluded that the higher the CPT, the more resistant the alloy is to be pitting. At temperatures lower than CPT, passivity breakdown is observed at very high anodic potentials, where above the CPT, pitting can occur, and breakdown potentials are far below those required for transpassivity.

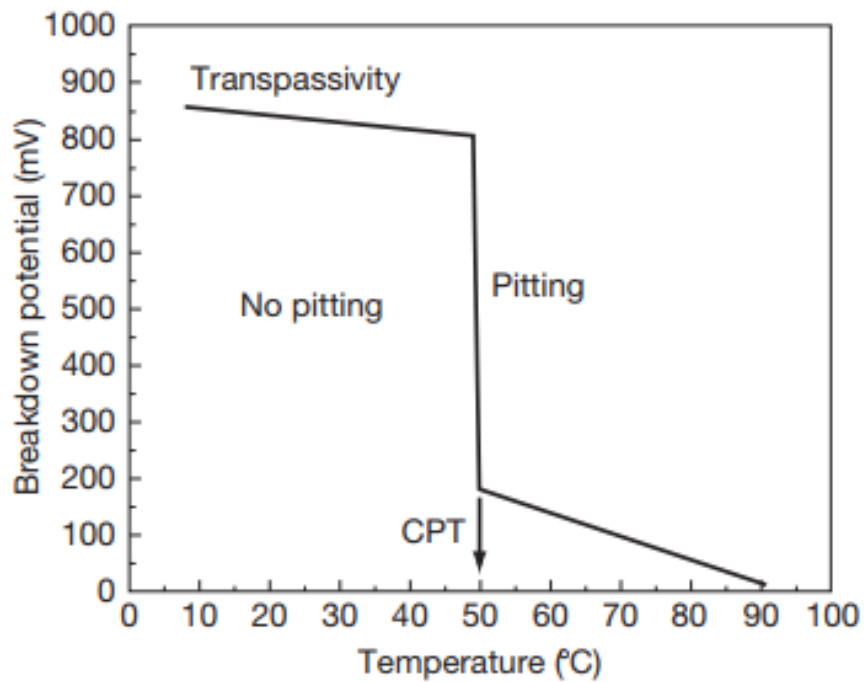
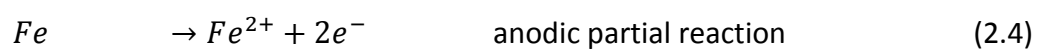


Figure 2.19: Critical pitting temperature [46]

2.4 Faraday's Law and corrosion factors

2.4.1 Faraday's Law

According to Landolt [36], a changeless oxidation-reduction (redox) reaction between an oxidising agent present in the environment and a metal leads to the corrosion of that metal. All redox reactions consist of 2 partial reactions which are also called half-cell reactions: (1) partial reduction reaction or cathodic partial reaction and (2) partial oxidation reaction which is also referred to as anodic partial reaction. Using iron as an example:





The cathodic and anodic partial reactions show explicitly the electrons that are exchanged during the course of the redox reaction.

According to Faraday's Law, when n_i moles of a given substance take part in a reaction, a proportional electric charge Q passes across the electrode-electrolyte interface:

$$Q = n \cdot F \cdot n_i \quad (2.7)$$

Here, F denotes a universal constant, called Faraday constant: $F = 96485 \text{ C/mol}$. The charge number n , which does not have units, is assumed to be the stoichiometric coefficient of the electrons in the equation for the electrode reaction. For iron, which describes the anodic dissolution above, $n = 2$ [36].

As Landolt [36] pointed out, by taking the derivative of equation (2.7) with respect to time, Faraday's Law can be rewritten as:

$$I = nF \frac{dn_i}{dt} \quad (2.8)$$

where the electric current is given by $I = dQ/dt$. Here, dn_i/dt describes the rate of reaction in moles per second. Faraday's Law which is rewritten as equation (2.8) expresses that the rate of an electrode reaction is proportional to the magnitude of the electrical current that crosses the electrode-electrolyte interface.

An electrochemical cell is a system consisting of 2 electrodes which are in contact with an electrolyte, and these 2 electrodes are connected by an electric conductor. The common examples of electrochemical cells are corrosion cells, battery cells, and fuel cells. A model of an H_2/O_2 fuel cell is shown in Figure 2.20. In this model, oxygen is reduced to H_2O at the cathode while hydrogen is oxidised to H^+ . Inert materials are used as electrodes in this fuel cell, and a solution of acid, normally phosphoric acid, acts as the electrolyte. Then, oxygen and hydrogen cause the oxidation-reduction reaction,

which is self-generated, and electric power is produced by the H₂/O₂ fuel cell [6]. The current through the electrodes is given by:

$$I = 4F \frac{dn_{O_2}}{dt} = 2F \frac{dn_{H_2}}{dt} \quad (2.9)$$

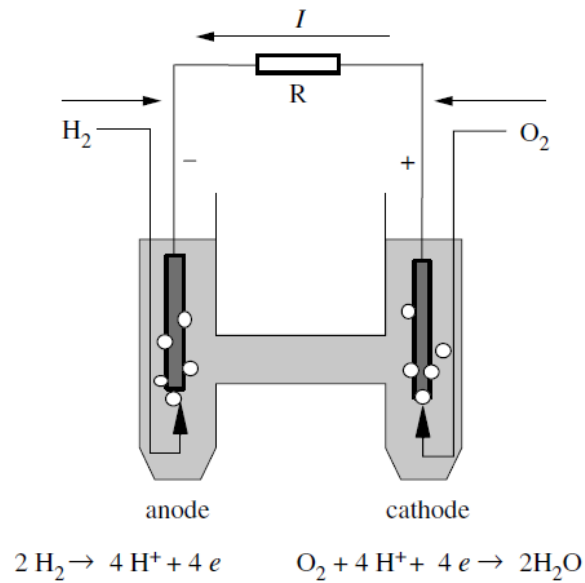


Figure 2.20: H₂/O₂ fuel cell [36]

2.4.2 Corrosion reaction factors

As Landolt [36] pointed out, the rate of an electrode reaction depends on the potential drop at the electrode-electrolyte interface. As Faraday's Law illustrates, the rate of reaction is relative to the current density that flows through the electrode-electrolyte interface. The kinetics of electrochemical reactions can be measured by the current density as a function of potential. To obtain the current density i , the measured current is divided by the surface A of the working electrode:

$$i = I / A \quad (2.10)$$

The current that passes between the working electrode and the counter electrode creates a potential gradient in the electrolyte. The measured potential, $E_{measured}$, is the sum of the electrode potential E and the ohmic potential drop in the electrolyte between the reference electrode and the working electrode, $\Delta\Phi_{\Omega}$:

$$E_{measured} = E + \Delta\Phi_{\Omega} \quad (2.11)$$

The value of $\Delta\Phi_{\Omega}$ can be calculated from the following equation:

$$\Delta\Phi_{\Omega} = \frac{i \cdot L}{\kappa} \quad (2.12)$$

where κ is the conductivity of the electrolyte, and L represents the distance between the capillary and the surface of the working electrode.

When the chemical reaction reaches the equilibrium state, the net reaction rate is 0. This means:

$$E = E_{rev}: \quad i = ia + ic = 0 \quad (2.13)$$

where E_{rev} is the equilibrium potential or reversible potential; as a result:

$$i_{a(E_{rev})} = -i_{c(E_{rev})} = i_0 \quad (2.14)$$

The equation describes the exchange current density i_0 of an electrode reaction. This new volume estimates the rate of charge transfer at equilibrium.

2.5 Mechanism of corrosion fatigue

Fatigue is a mechanism of slow crack growth, induced by variable stresses working on the structure of engineering components. It takes place at relatively low stresses and loads before the engineering components reach ductile or brittle fracture. The mechanism of fatigue includes 3 different processes: Crack nucleation, crack propagation, and fracture. Cracks are normally nucleated at the surface of an engineering component as the surface contains areas of critical stress concentration.

Corrosion pits, introduced above, play an important role in generating severe stress concentrations at the surface [14]. Cracks caused by stress joints with specific metal/electrolyte pairs, which lead to failure, are attributed to environment sensitive cracking. There is a significant difference between cyclic or periodic stress and static stress. Cyclic stress is called corrosion fatigue and static stress is called “stress corrosion cracking” (SCC) by most researchers [32]. The difference between corrosion fatigue and SCC is shown in Figure 2.21.

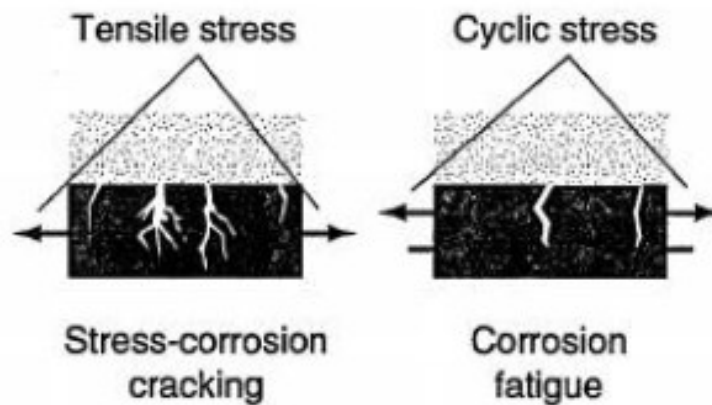


Figure 2.21: Different stresses working in a corrosive environment [55]

SCC is a term that combines the action of applied or residual tensile stress or shear stress and corrosion. SCC is generally observed only in specific metal-environment combinations and in a limited temperature interval [36]. Generally, SCC is found to occur more frequently in alloys than in pure metals though there are some well-documented cases showing the opposite situation, especially with copper. In the absence of stress, an alloy is normally subjected to weak reactions in a similar environment with the same species that would have otherwise led to cracking. Stress-corrosion cracks can appear in a brittle fracture even when a material is especially ductile [56].

There are many differences between corrosion fatigue and SCC. The most important difference is that corrosion fatigue is highly non-specific. Corrosion fatigue is a result of the combined action of cycling stresses and a corrosive environment. Metal fatigue resistance is reduced in corrosive environments. Almost all engineering structures experience some form of alternating stress and are exposed to corrosive environments during their service life. Therefore, corrosion fatigue is more dangerous than common corrosion and it is also a very complex phenomenon [32].

Corrosion fatigue damage usually goes through with cyclic load in 4 stages: cyclic plastic deformation, micro-crack initiation, small crack growth to linkup and coalescence, and macro-crack propagation. In corrosion fatigue, failure of the critically loaded parts of a component occurs just before corrosion has significantly damaged the cross-sectional area of such a component. However, it is still a significant factor when the structures lose load carrying material and fail owing to corrosion. The critical role of corrosion fatigue is at the crack point where crack propagation occurs. Corrosion pits play a significant role in corrosion fatigue as crack initiators. In the case of pitting corrosion, stress concentrations are produced around the pits, resulting in the local stress intensity increasing beyond the critical value in the crack initiation stage. Small cracks caused by corrosion becomes significant at the initial stages of acceleration of fatigue crack growth. Even if a pit is not formed directly by pitting corrosion, the initiation of fatigue can be accelerated by corrosion in the microscopic phase during pit propagation and growth [14].

The underlying mechanisms of crack initiation are poorly understood in corrosion fatigue. However, it is generally believed that corrosion plays an important role in the crack initiation stage [36]. Compared with the dry condition, corrosion does not speed up the crack growth rate when the crack is large. SCC is not accelerated by different pit structures; on the contrary, stress-corrosion cracks need to be exposed to an aggressive chemical environment for a specific period of time before fracture occurs. As Batchelor et al. [14] pointed out, crack growth is related to the chemical reaction between the

material and corrosive environment. This reaction obeys the rule in which inert materials have higher resistance to corrosion fatigue and fracture, provided the mechanical strength of the material is not less than that of the non-inert material.

When modelling the corrosion fatigue process, it can be assumed that the process consists of 3 stages: pit growth, crack nucleation from the pit, and corrosion fatigue crack propagation [20, 57-64]. The key event in the corrosion fatigue process is the pit-to-crack transition. After reviewing many models, 2 basic models were found to evaluate the corrosion fatigue crack nucleation process: critical pit size model [65-66] and pit growth/crack growth competition model [58, 67]. Both the models consider corrosion pit as a surface crack and its growth rate is described by pit kinetics. In the critical pit size model, the pit grows to a critical size and a corrosion fatigue crack is considered to have nucleated from it when the local mechanical conditions are adequate for the onset of crack growth. The critical condition is defined in terms of the threshold stress intensity factor for corrosion fatigue (ΔK_{th}). On the other hand, in the competition model, the pit growth law of a corrosion pit is formulated using fracture mechanics. The occurrence of corrosion fatigue nucleation is defined by the critical pitting condition (ΔK_p) at which the crack growth rate exceeds the pit growth rate. These 2 models provide a framework for predicting corrosion fatigue by correlating the parameters of fracture mechanics to crack nucleation [58, 67]. However, the usefulness and applicability of these models is not yet fully established because quantitative evidence is lacking.

The first simple and useful approach was developed in 1989 by Kondo [58, 67]. Kondo predicted the pit-to-crack transition and the associated critical crack length for corrosion fatigue cracks. Kondo's model is used to find fatigue crack initiation in low alloy steels. The pit-to-crack transition was based on 2 assumptions, namely the pit depth must be greater than a threshold value, corresponding to a particular ΔK (stress intensity factor range), and the crack growth rate should exceed the pit growth rate.

Kondo's approach was further developed by Wei et al. through a probabilistic model [59, 68-71]. They characterised the corrosion fatigue process using a simple model of pit growth that assumed a sustained hemispherical geometry, followed the criteria set by Kondo, and used laboratory-determined corrosion fatigue crack growth rates. A reasonable prediction of crack distribution in aircraft wings was obtained. Recently, a combination of deterministic and statistical approaches was developed by Engelhardt and Macdonald [72] and used to model the evolution of cracks in steam turbines starting from pits [73]. Similarly, Turnbull [19, 74-75] developed a model based on deterministic equations with statistically distributed input parameters. The model used Kondo's conditions for the pit-to-crack transition and captured the statistical variability of pit and crack growth using the MCM, where input values were chosen at random from statistical distributions. It was successfully applied to the simulation of the time-evolution of pit depth distribution to determine the percentage of pits that transform into stress corrosion cracks in the case of steam turbine steel discs. Figure 2.22 shows the damage chain through the sequence of events and processes that lead to fracture of structural components experiencing pitting damage under corrosion fatigue conditions [20].

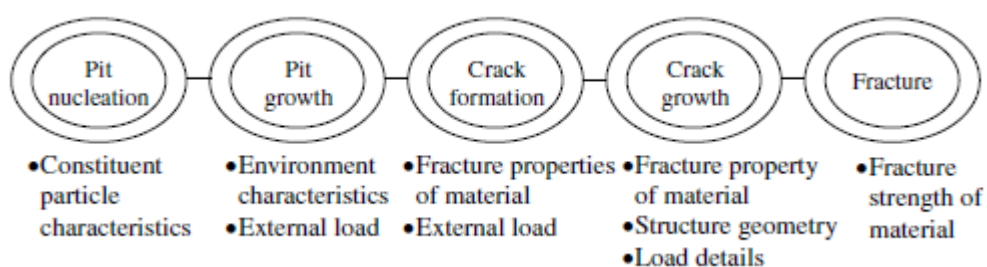


Figure 2.22: Damage chain showing sequence of events and processes of material degradation [20]

2.6 Numerical methods in predicting pitting corrosion

For predicting pitting corrosion, different models have been developed and widely used to simulate the growth of pit depth in aluminium alloy [4-8] and stainless steel [9-12]. Initially, with a poor understanding of the mechanisms of pitting corrosion, an empirical model based on corrosion data for long-term corrosion of pipes in a range of soils was introduced [76]. This model required a huge amount of pitting corrosion data to simulate pit depth and pit growth rate with a statistical method. To obtain these data, a relatively long period of time was needed for data collection. Later, with a better understanding of the mechanisms of pitting corrosion, mechanical models were developed. Further, the MCM was combined with mechanical models for predicting pitting corrosion in underground cables or pipes. Such kinds of models can simulate the pit depth and pit growth rate and treat pit morphology as a critical input. Investigations on pit morphology indicate that the potential due to the electrochemical reactions in the pit plays a direct role in deciding the surface texture of pits, including their size and shape [77-79]. In the following sections, 3 different models will be introduced to simulate corrosion pit depth.

2.6.1 Monte Carlo simulation with pitting corrosion processes

The Monte Carlo simulation is an alternative to analytical mathematics for understanding a statistic's sampling distribution and evaluating its behaviour in random samples. The random samples from known populations of simulated data are used by the Monte Carlo simulation to track a statistic's behaviour. The basic concept is simple: the values can be taken from a given population if a statistic's sampling distribution is the density function of the values. Then, its estimate is the relative frequency distribution of the values of that statistic, which were actually observed in many samples drawn from that population [80-81].

For pitting corrosion, it is important to note that a few pits or even a single pit may be alive on the corroding metal surface at a particular time. In this situation, the differential equations which are equivalent to a balance equation for particles in discontinuous media for the damage function could lose their strict physical meaning. The main idea of using the MCM for pitting corrosion is to keep track of each stable pit that has reached the nucleation stage, propagation stage, and repassivation stage on the metal surface. An advantage of this method lies in the fact that it allows one to take into account the interactions between special individual pits in an explicit manner. It becomes possible to decrease the number of unknown parameters which describe the interaction between individual pits by applying this method [38]. The Monte Carlo simulation describes all 3 stages of propagation damage – nucleation, propagation, and repassivation of stable pits.

2.6.1.1 Modelling pit nucleation

To keep track of each stable pit on the metal surface, the following deterministic Monte Carlo model was used [31]. Initially, it is assumed that there are no stable pits on the metal surface. The probability of a pit nucleating in stable form during the time step dt is given by:

$$P_{nucl} = \frac{N(t+dt) - N(t)}{N_0 - N(t)} \quad (2.15)$$

where, N_0 is the total number of stable pits that can nucleate on the metal surface of a said area. Pits are numbered by the index $k = 1, 2, \dots, N_0$, so that each pit can be tracked individually. $N(t)$ is the number of stable pits that nucleate within the time interval between 0 and t . A random number $0 \leq G_k \leq 1$ is generated for each pit k that has not yet been born. If $G_k \leq P_{nucl}$, a pit is considered to have been born with a penetration depth of $x = 0$; otherwise, it is considered not to have been born and will be examined again in the following step [31]. The number of stable pits $N(t)$ is calculated using the point defect model (PDM), as described by Macdonald et al. [34] in the following sections.

The PDM has been designed for predicting the nucleation rate of metastable pits and stable pits [82-86]. The PDM assumes that oxide films or passive films formed on metal surfaces in contact with oxidising environments are bilayer structures including a highly (point) defective barrier layer. This highly defective barrier layer grows into the metal and an outer layer is formed by the hydrolysis of cations dispatched via the barrier layer or via transformation of the outer surface of the barrier layer itself [38]. As the PDM is able to explain all the experimental data for passivity-related breakdown of metals, it can be regarded as a suitable deterministic model for the nucleation of metastable pits on a metal surface [87].

Mathematically, the condition for the initial formation of the cation vacancy condensate can be represented as follows [82]:

$$(\zeta_{ca} - \zeta_m)(t - \tau) \geq \xi \quad (2.16)$$

where ζ_{ca} is the flux of cation vacancies across the barrier layer at the breakdown site, ζ_m is the annihilation flux, t is the time, τ is the dissolution time, and ξ is the critical areal concentration of the vacancies.

On any metal surface with a distribution of “weak points”, many potential breakdown sites appear. Therefore, Shibata [88] and Fratesi [89] suggested that the breakdown voltage obtained by examining the data can be treated as having normal distribution. According to Macdonald [86], the PDM assumes the breakdown sites are described by a normal distribution function which is:

$$\frac{dN(D)}{dD} = -A \exp\left[-\frac{(D-\bar{D})^2}{2\sigma_D^2}\right] \quad (2.17)$$

In the equation (2.17), $N(D)$ is the number of breakdown sites that have diffusivities greater than D , which represents the diffusivity of the population of the breakdown

sites. \bar{D} and σ_D are the average value and standard deviation, respectively. As the parameter A does not depend on D and $N_{mp,0}$ is defined as the total number of breakdown sites, the normalisation of diffusivity distribution using the condition $N(0) = N_{mp,0}$ yields:

$$N(D) = N_{mp,0} \operatorname{erfc}\left(\frac{D-\bar{D}}{\sqrt{2}\sigma_D}\right) / \operatorname{erfc}\left(-\frac{\bar{D}}{\sqrt{2}\sigma_D}\right) \quad (2.18)$$

As the cation vacancies are transported across the barrier layer from the layer-solution interface to the metal-layer interface by electro-migration, the cation vacancy flux density, ζ_{ca} , becomes proportional to D , which is the diffusion coefficient of the vacancies:

$$\zeta_{ca} = DB \quad (2.19)$$

Combining equation (2.19) and equation (2.16), the criterion for metastable pit nucleation is given as follows:

$$D \geq D_{cr} = \frac{\xi + \zeta_m(t-\tau)}{B(t-\tau)} \quad (2.20)$$

Equation (2.20) illustrates that the nucleation of metastable pits occurs only on those sites that have $D \geq D_{cr}$ within the observation time t . From equations (2.18) and (2.20), the following equation is generated:

$$N(t) = N_0 \operatorname{erfc}\left(\frac{a}{t-\tau} + b\right) / \operatorname{erfc}(b) \quad (2.21)$$

where τ is the dissolution time, $a = \xi / (B\sqrt{2}\sigma_D)$, and $b = (\frac{\zeta_m}{B} - \bar{D}) / (\sqrt{2}\sigma_D)$. Additionally, the dissolution time, τ , is identified as the time taken for the cap over the vacancy condensate to thin sufficiently for rupture to occur from the point of initial cation vacancy condensation [87].

2.6.1.2 Modelling pit propagation

A stable pit propagation can be modelled using Faraday's Law, as described by Macdonald and Engelhardt [38]. At each time step, the pit depth of the j -th stable living pit, a_j , can be calculated sequentially by:

$$a_j(t + dt) = a_j(t) + K_V i_j(t) dt \quad (2.22)$$

where K_V is the electrochemical equivalent of the metal that transforms the corrosion current density at the pit's internal surface into the rate of metal removal. In the above equation, the parameter i_j is defined by Tafel's law for the active metal dissolution current density as:

$$i_j = i_0 \exp\left(-\frac{\alpha F \Delta\phi_j}{RT}\right) \quad \text{at } \Delta\phi_j < \Delta\phi_{cr} \quad (2.23 \text{ a})$$

$$i_j = 0 \quad \text{at } \Delta\phi_j \geq \Delta\phi_{cr} \quad (2.23 \text{ b})$$

where $\Delta\phi_j$ is the averaged potential drop on the active surface, α is the transfer coefficient of the metal dissolution reaction, i_0 is the exchange current density, T is the Kelvin temperature, F is Faraday's constant, and R is the gas constant. $\Delta\phi_{cr}$ is the difference between corrosion and repassivation potentials. The pit can continue to grow only when the metal potential at the bottom of the pit, E , is larger than the potential of repassivation, E_{rp} . The relationship shown in formula is $E = E_{corr} - \Delta\phi_j > E_{rp}$ or $\Delta\phi_j < E_{corr} - E_{rp}$.

As Macdonald and Engelhardt [29] pointed out, the average potential drop on the active surface of a hemispherical pit can be determined by the following equation:

$$\Delta\phi_j = \frac{b a_j i_0}{\kappa} \exp\left(-\frac{\alpha F \Delta\phi_j}{RT}\right) + \sum_{k \neq j} \frac{i_0 \alpha_k^2}{\kappa d_k} \exp\left(-\frac{\alpha F \Delta\phi_k}{RT}\right) \quad (2.24)$$

In this equation, the index k denotes the pits on the surface while the pit of interest is denoted by the index j , and these pits are assumed to be as far away as possible from

each other. Further, a_k is the radius of the hemispherical pit, κ is the conductivity, d_k is the distance between the centres of particular pit and surrounding pit, and b is a constant equal to 2.1. In this equation, the contribution of each pit is considered independently. Noting that $\Delta\varphi_j$ indicates the potential drop from some point within the pit and a remote point on the external surface, the first term on the right side of the equation describes the contribution of the central pit to the total potential drop [90] while the second term describes the contribution of all other pits on the corroding surface [91]. $\Delta\varphi_k$ in the second term on the right side of the equation is assumed to be known and equal to the previous values for the iteration sense. During each time step, a pit is considered to stop growing if $\Delta\varphi_j > \Delta\varphi_{cr}$; otherwise, the pit is assumed to keep growing. After each time step is finished, the repassivated or dead pits are removed from the population of actively growing pits.

2.6.1.3 Modelling pit repassivation

According to the mechanism of pitting corrosion, pits can repassivate while they are growing. Macdonald and Engelhardt [29] considered the probability of pits repassivating accidentally. They assumed that the probability of a pit repassivating during each time step is proportional to the dimension of this step.

The probability of repassivation is given by:

$$P_\gamma = \gamma dt \quad (2.25)$$

where γ is the delayed repassivation constant. Practically, for the j -th living pit in each time step, the random number $0 \leq G \leq 1$ is generated. If $G > P_\gamma$, the pit is considered to be alive on entering the next time step; otherwise, the pit is considered to be passivated and will not grow in the further consideration.

2.6.2 Empirical models

According to Velázquez et al. [12, 15, 92], the generally accepted form of the dependence of maximum pit depth on exposure time was originally developed by Romanoff [76]:

$$d_{max} = kt^v \quad (2.26)$$

This equation is based on long-term corrosion data from pipes in a range of soils studied by Romanoff [76] years ago. The k and v in the equation are constant regression parameters, and v falls in the range of 0.3–1.0 [93]. However, the present study aims to find a complete and accurate predictive model for pit growth on buried oil and gas pipelines. Therefore, a similar equation to define the maximum pit depth is given as:

$$d_{max}(t) = k(t - t_0)^\alpha \quad (2.27)$$

This model differs from the previous equation because of the use of the initiation time t_0 , which is regarded as an unknown parameter to be determined as part of the analysis.

A multivariate and non-linear regression analysis based on equation (2.27) was conducted by Velázquez et al [12]. They assumed that the maximum pit depth was the dependent variable, and the pipeline age, soil, and pipe characteristics were the independent variables. Then, they determined the best correlation between the exponent and proportionality parameters and the soil and pipe variables [94-95] (the meaning of symbols is shown in Table 2.1 and Table 2.2):

$$k = k_0 + k_1rp + k_2ph + k_3re + k_4cc + k_5bc + k_6sc \quad (2.28)$$

$$\alpha = \alpha_0 + \alpha_1pp + \alpha_2wc + \alpha_3bd + \alpha_4ct \quad (2.29)$$

Variable, symbol (units)	Probability density function			
	Clay (110)	Clay loam (61)	Sandy clay loam (79)	All (250)
Max pit depth, d_m (mm)	GEV (2.25, 3.90)	GEV (1.88, 2.97)	GEV (1.25, 0.99)	GEV (1.84, 2.92)
Resistivity, re ($\Omega \cdot m$)	Weibull (62, 4275)	Weibull (28, 566)	Lognormal (49, 2363)	Lognormal (50, 2931)
Sulphate, sc (ppm)	Gamma (131, 12566)	Lognormal (208, 65549)	Weibull (144, 9836)	Lognormal (154, 25328)
Bicarbonate, bc (ppm)	Lognormal (19, 639)	Lognormal (23, 548)	Lognormal (14, 36)	Lognormal (19, 436)
Chloride, cc (ppm)	Lognormal (53, 4709)	Lognormal (45, 2946)	Lognormal (22, 559)	Lognormal (41, 3135)
Water content, wc (%)	Normal (24, 47)	Weibull (25, 27)	Normal (22,33)	Normal (24, 38)
pH, ph	Gumbel (5.94, 0.97)	Gumbel (6.36, 0.77)	Normal (6.23, 0.637)	Gumbel (6.13, 0.84)
Pipe/soil potential, pp (V)	Normal (-0.86, 0.04)	Normal (-0.81, 0.04)	Normal (-0.92, 0.023)	Normal (-0.86, 0.04)
Bulk density, bd (g/ml)	Normal (1.22,0.003)	Gumbel (1.32, 0.0005)	Gumbel (1.39, 0.002)	Normal (1.30, 0.007)
Redox potential, rp (mV)	Uniform (2.14, 348)	Uniform (19, 301)	Uniform (20, 339)	Uniform (2.14, 348)

Table 2.1: Statistical fitting of the observed corrosion data [12]

Coating type (<i>ct</i>)	Score	Coating probability by soil category			
		Clay	Clay loam	Sandy clay loam	All
Bare pipe	1.0	0.102	0.119	0.194	0.118
Asphalt enamel	0.9	0.019	0.017	0.039	0.024
Wrap-tape	0.8	0.421	0.288	0.429	0.382
Coal-tar	0.7	0.449	0.542	0.273	0.443
FBE	0.3	0.009	0.034	0.065	0.033

Table 2.2: Scoring model for pipeline coating type [12]

The regression coefficients k_i and α_i are given in Table 2.3 with the value determined for the pit initiation time t_0 for each soil category. As Velázquez et al. [12] pointed out, the pit depth model described by equations (2.28) and (2.29) is dependent on the pH value, pipe coating type, pipe-to-soil potential, bulk density, water content, and dissolved chloride content.

Parameter (variable, symbol)	Soil category			
	Clay	Clay loam	Sandy clay loam	All
k_0	5.51×10^{-1}	9.84×10^{-1}	5.99×10^{-1}	6.08×10^{-1}
α_0	8.85×10^{-1}	2.82×10^{-1}	9.65×10^{-1}	8.96×10^{-1}
t_0 (years)	3.05	3.06	2.57	2.88
k_1 (redox potential, rp)	-8.98×10^{-5}	-1.06×10^{-4}	-1.82×10^{-4}	-1.80×10^{-4}
k_2 (pH, ph)	-5.90×10^{-2}	-1.15×10^{-1}	-6.42×10^{-2}	-6.54×10^{-2}
k_3 (resistivity, re)	-2.15×10^{-4}	-2.99×10^{-4}	-2.12×10^{-4}	-2.60×10^{-4}
k_4 (chloride, cc)	8.38×10^{-4}	1.80×10^{-3}	8.62×10^{-4}	8.74×10^{-4}
k_5 (bicarbonate, bc)	-1.28×10^{-3}	-4.88×10^{-4}	-6.78×10^{-4}	-6.39×10^{-4}
k_6 (sulphate, sc)	-5.33×10^{-5}	-2.09×10^{-4}	-1.13×10^{-4}	-1.22×10^{-4}
α_1 (pipe/soil potential, pp)	4.93×10^{-1}	4.61×10^{-1}	5.12×10^{-1}	5.19×10^{-1}
α_2 (water content, wc)	3.72×10^{-3}	1.69×10^{-2}	4.50×10^{-4}	4.65×10^{-4}
α_3 (bulk density, bd)	-1.01×10^{-1}	-9.87×10^{-2}	-1.58×10^{-1}	-9.90×10^{-2}
α_4 (coating type, ct)	4.67×10^{-1}	5.67×10^{-1}	4.34×10^{-1}	4.31×10^{-1}

Table 2.3: Regression coefficients for the maximum pit depth model [12]

The pitting rate of the model could be obtained by taking the time derivative of the equation (2.27). Therefore, the time dependence of the maximum pit growth rate is modelled as:

$$v_m(t) = k'(t - t_0)^{\alpha'} \quad (2.30)$$

In the empirical model, the statistical method is used for estimating the probability distributions of pit depth and pit growth rate with a huge amount of data. A fairly long time period of experimentation is needed for corrosion data collection. Equations (2.28) to (2.30) are used together with the information from Tables 2.2–2.4 to simulate pit depth and pit growth rate distributions for different exposure times. For this model, the statistical distributions are associated with corrosion data, which means the normal, lognormal, and maximal generalised extreme value (GEV) distributions are fit to the simulated data [96]. The distribution that can fit all the data best is selected to predict the pit depth and pit growth. In the majority of pitting corrosion cases, the GEV distribution was found to be the best choice [12].

By using this empirical model, the probability distributions of pitting corrosion depth and growth rate in underground pipes can be investigated in a range of soils. The Monte Carlo simulation is used to investigate the probabilistic distributions of pit depth and pit growth rate. To analyse such a huge amount of data, GEV distribution is used to fit the data, and the statistical method also contributes to the model. The shape parameters of the statistical method are determined by the Monte Carlo simulation.

2.6.3 Mechanical model

Pitting corrosion involves a complicated mechanism that leads to the loss of material at highly localised pits [20]. According to Velázquez et al. [15], pit depth is dependent on many factors, namely pH value, concentration of chloride, temperature, and other mechanism parameters. In such a situation, a practically feasible approach is to design a model that can use connected parameters to represent the actual mechanisms that affect pit growth [20]. For modelling and studying pit growth, pit morphology is a significant input parameter. The potential generated from the electrochemical reaction in the pit is decided by its surface factors, namely size and shape [77-79]. Rajasankar and Iyer [20] built a model with pitting current potential and temperature to describe the corrosivity of the environment and activation energy of the metal/alloy to represent

its resistance to pitting. Further, for comprehensibility, the model simulated constant volume growth in the pit's growth period. This simulation was acceptable based on the recommendations of Harlow [68] and Zhang [97]. For this model, it is acceptable to use Faraday's Law, which shows the relationship between time and metal dissolution as:

$$\frac{dv}{dt} = f(N_m, N_e) \quad (2.31)$$

where N_m denotes the variables used to explain corrosion characteristics of metal/alloy and N_e denotes the environment-related variables. Based on the detailed discussions above, the variables for N_e and N_m are represented as:

$$N_m = \{M, n, \rho\} \quad (2.32 \text{ a})$$

$$N_e = \{I_p\} \quad (2.32 \text{ b})$$

I_p , M , n , and ρ in equation (2.32) represent the pitting current density, molecular weight, valence, and mass density of the metal/alloy, respectively. According to the laws of basic electrochemistry [98-99], metal dissolution can be expressed as:

$$\frac{dv}{dt} = \frac{MI_p}{nF\rho} \quad (2.33)$$

The Arrhenius equation gives the mathematical expression to evaluate the pitting current as:

$$I_p = I_{po} \exp\left[-\frac{\Delta H}{RT}\right] \quad (2.34)$$

where I_{po} is the pitting current constant or exchange current density, and ΔH is the activation energy of the alloy. According to equations (2.33) and (2.34), the relationship of pit shape is:

$$\frac{dv}{dt} = \frac{MI_{po}}{nF\rho} \exp\left[-\frac{\Delta H}{RT}\right] \quad (2.35)$$

As Rajasankar and Iyer [20] pointed out, the theory of pit growth is almost clearly understood according to the electrochemical and mechanical properties of the environment-material system. However, the dissolution of a metal/alloy is associated with pit shape. Figure 2.23 shows the basic shape of a pit.

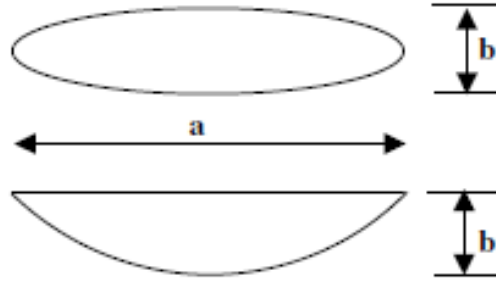


Figure 2.23: The shape of a pit [20]

Based on Figure 2.23, the volume of a pit could be calculated as:

$$v = \frac{2}{3} \pi a b^2 \quad (2.36)$$

The changing rate of the volume could be evaluated as:

$$\frac{dv}{dt} = \frac{2}{3} \pi \left[\frac{da}{dt} b^2 + 2ab \frac{db}{dt} \right] \quad (2.37)$$

Combining equations (2.35) and (2.37), we get:

$$\frac{2}{3} \pi \left[\frac{da}{dt} b^2 + 2ab \frac{db}{dt} \right] = \frac{M I_{po}}{n F \rho} \exp\left[-\frac{\Delta H}{RT}\right] \quad (2.38)$$

Using m as an aspect ratio of pit depth and diameter, i.e. $m = a/b$, equation (2.38) can be rewritten as:

$$2\pi m^2 a^2 \frac{da}{dt} = \frac{M I_{po}}{n F \rho} \exp\left[-\frac{\Delta H}{RT}\right] \quad (2.39)$$

Using integration, the total time for pit growth could be evaluated as:

$$t_c = \frac{2}{3} \pi m^2 \frac{n F \rho}{M I_{po}} \exp\left(\frac{\Delta H}{RT}\right) (a_c^3 - a_i^3) \quad (2.40)$$

where a_i is the initial pit size and a_c is the pit's critical size. This equation can be rewritten as an expression of the size of the pit at time t :

$$a = [a_i^3 + \frac{3}{2} \frac{M I_{p0}}{n F \rho} \frac{t}{\pi m^2} \exp(-\frac{\Delta H}{RT})]^{1/3} \quad (2.41)$$

Therefore, equation (2.41) can be used to estimate pit size. Also, it can predict the pit growth rate during the pit growth period.

For the chosen set of probability density functions, $f(x)$, of the model parameters, the cumulative distribution function (cdf) of pit size is expressed as:

$$F(a) = Prob(a \geq a_{TP}) = \int_{a \geq a_{TP}} f(x) dx \quad (2.42)$$

$t=TP$

where $F(a)$ denotes the probability of the pit size at target period (TP) to be less than or equal to the given pit size a .

According to Rajasankar and Iyer [20], it is logical to investigate the possibility of pit growth from a cluster of constituent particles. A power-law-type relationship to estimate the probability of the formation of a particle is $Prob\{np = p\} = 0.725p^{-2.41}$. In this relationship, p ($= 1, 2, \dots$) denotes the number of particles in a cluster. Similarly, the pitting current coefficient, I_{p0} , is also determined empirically as a function of particle density: $I_{p0} = (p + 1)6.5 \times 10^{-5}$. By using the law of total probability, for a general case of a cluster with " p " particles, under the condition of $Prob\{np = p\} > 0$ for $p > 0$, the probabilistic pit size is given by:

$$Prob\{a_p\} = Prob\{np = 1\}Prob\{a|np = 1\} + Prob\{np = 2\}Prob\{a|np = 2\} + \dots + Prob\{np = i\}Prob\{a|np = i\} + \dots + Prob\{np = p\}Prob\{a|np = p\} \quad (2.43)$$

The main requirement to ensure the validity of the disintegration in equation (2.43) is $Prob\{np = i\} > 0$ for all $i > 0$. This requirement is simply fulfilled in the case of a particle cluster that can be easily interpreted from equation $Prob\{np = p\} = 0.725p^{-2.41}$. Therefore,

$$Prob\{a_p\} = \sum_{i=1}^p Prob\{np = i\}Prob\{a|np = i\} \quad (2.44)$$

where $Prob\{a|np = i\}$ is the conditional probability of the pit size for a given particle cluster.

Based on the above, the expression for cdf of pit size can be rewritten as:

$$F(a) = \sum_{i=1}^p Prob\{np = i\}Prob\{a \geq a_{TP}|np = i; TP\} \quad (2.45)$$

Owing to the condition of the clusters, the expression to evaluate pit size needs to be written as:

$$a = [a_i^3 + \frac{3MI_{po}(p)}{2nF\rho} \frac{t}{\pi m^2} \exp(-\frac{\Delta H}{RT})]^{1/3} \quad (2.46)$$

which shows that pitting current is the only quantity that depends on the cluster size.

The cumulative distribution function values of pit size expressed in equations (2.45) and (2.46) provide the basis for determining the probabilistic features of pit growth. In this model, cluster probability can be determined in a straightforward manner while the probability of other quantities needs to be determined under the conditional situation of cluster density.

2.7 Overview of nonlinear stress analysis using finite element method

The FEM was used in this thesis to analyse the effect of critical pit depth on reinforcing tapes with cable internal pressure. The reported measured tensile strength of reinforcing tapes at failure was 548 MPa and yield point was 158 MPa. Therefore, stress analysis is needed to determine whether the reinforcing tapes work on areas showing plastic behaviour. Moreover, if the reinforcing tapes work on areas of plastic behaviour,

the plastic deformation region must be pointed out as it can illustrate the situation of plastic strain. The theories and methods presented in this section will be used in Chapter 6 for a further discussion on the stress behaviour of reinforcing tapes subjected to internal oil pressure.

The FEM was developed independently by engineers, physicists, and mathematicians. The theory of applying energy principles to structural analysis problems was proposed by Argyris and Kelsey [100] in 1960. Later in the same year, Clough introduced the term “Finite Element Method” [101]. In the late 1960s and 1970s, significant progress was made in the field of finite element analysis (FEA). With the improvements in the speed and memory of computers, this method was significantly upgraded. In the field of solid mechanics, this method is not limited to the elastic analysis of plane stress and plane strain problems but also successfully applied to the analysis of 3D problems, stability and vibration problems, and non-linear analysis [102-107].

FEA is a numerical technique that is widely used in engineering analysis because of its flexibility and diversity. In this method, all the complications of the problems, such as shape differences, boundary conditions, and applied loads are preserved as they are but the solving methods are approximated. Initially, FEA was used as a method of stress analysis when designing aircrafts. It started as an extension of the matrix method of structural analysis. Now, FEA is used not only in the analysis of solid mechanics but also in the analysis of fluid flow, electric and magnetic fields, heat transfer, and other fields. In addition, this method is widely used for the analysis of beams, plates, shells, and rock mechanics by civil engineers. Moreover, both static and dynamic problems can be solved by FEA [108].

There are some basic unknown factors in engineering issues such as displacement in solid mechanics, velocities in fluid mechanics, and electric and magnetic potentials in electrical engineering, and temperatures in heat flow. The behaviour of a structure can

be estimated once the issues are identified. Furthermore, these basic unknown factors are infinite. FEA decreases such infinite unknowns to a finite number by dividing the problem area into small parts called elements and by presenting the unknown variables in terms of assumed approximating functions for each element. The points in terms of field variables defined by approximating functions are called nodes or nodal points. Therefore, the unknown factors are the field variables of the nodal points for FEA. The next step in FEA is to build up element properties for each element after setting the elements and nodal unknowns. In solid mechanics, the force-displacement and stiffness characteristics of each individual element need to be found. The kind of relationship is given by:

$$[k]_e \{\delta\}_e = \{F\}_e \quad (2.47)$$

where $[k]_e$ is the element stiffness matrix, $\{\delta\}_e$ is nodal displacement vector of the element, and $\{F\}_e$ is the nodal force vector [108].

Element properties are used to gather global or structure properties to generate system equations $[k] \{\delta\} = \{F\}$. Then, the boundary conditions are applied. The nodal unknowns are calculated by these simultaneous equations. Then, the values of stresses, strains, and moments that are commonly required in solid mechanics' problems can be obtained by using the nodal values with additional calculations. Therefore, the steps of FEA are as follows [108]:

- a) Select suitable field variable and elements
- b) Discretise the continua
- c) Select approximating functions
- d) Find the element properties
- e) Assemble element properties to get global properties
- f) Impose the boundary conditions
- g) Solve the system equations to get the nodal unknowns
- h) Make additional calculations to get the required values

2.7.1 Elastic model

The general linear elastic relationship between stress and strain is known as Hooke's Law. The uniaxial form is:

$$\sigma = E\varepsilon \quad (2.48)$$

It covers both anisotropic and isotropic elastic materials. The general proportionality constant between stress and strain in 3 dimensions is a 4th-order tensor called stiffness. The 3D linear elastic model must be of the form:

$$\sigma_{ij} = C_{ijkl}\varepsilon_{kl} \quad (2.49)$$

In addition, the rate of this constitutive law can be shown as:

$$\dot{\sigma}_{ij} = C_{ijkl}^{\sigma} \cdot D_{kl} \quad (2.50)$$

where D_{kl} is the rate of deformation. Because of poor reflection of the movement of objects when using $\dot{\sigma}_{ij}$, the Jaumann rate is introduced to the constitutive law. The relationship between Jaumann rate and strain rate can be shown as:

$$\sigma_{ij}^{\nabla} = C_{ijkl}^{\sigma J} \dot{\varepsilon}_{kl} \quad (2.51)$$

In equation (2.51), $C_{ijkl}^{\sigma J}$ is defined as 4th-order elastic tensor and the form is:

$$C_{ijkl}^{\sigma J} = 2GI_{ijkl} + K\delta_{ij}\delta_{kl} \quad (2.52)$$

where $G = E/2(1 + \nu)$ is the shear modulus and $K = E/3(1 - 2\nu)$ is the bulk modulus. For I_{ijkl} , it is the 4th-order symmetric deviatoric tensor:

$$I_{ijkl} = \frac{1}{2}(\delta_{ik}\delta_{jl} + \delta_{il}\delta_{jk}) - \frac{1}{3}\delta_{ij}\delta_{kl} \quad (2.53)$$

For any symmetrical partial tensor s_{ij} and symmetry tensor ε_{ij} :

$$C_{ijkl}^{\sigma J} s_{kl} = 2G s_{ij} \quad (2.54)$$

$$I_{ijkl} \varepsilon_{kl} = \varepsilon'_{ij} \quad (2.55)$$

where ε'_{ij} is the partial tensor of symmetry tensor ε_{ij} . The equation (2.51) can be expressed as:

$$s_{ij}^{\nabla} = 2G\dot{\epsilon}'_{ij} \quad (2.56)$$

$$\dot{\sigma}_m = K\dot{\epsilon}_{kk} \quad (2.57)$$

where s_{ij}^{∇} is the Jaumann rate of deviatoric stress, and $\dot{\sigma}_m$ is the rate of change of hydrostatic stress, hence:

$$\dot{\epsilon}'_{ij} = \dot{\epsilon}_{ij} - \frac{1}{3}\dot{\epsilon}_{kk}\delta_{ij} \quad (2.58)$$

where $\dot{\epsilon}'_{ij}$ is the deviatoric strain rate, and $\dot{\epsilon}_{kk} = \dot{V}/V$ is the volume strain rate [109].

2.7.2 Elastoplastic model

The elastoplastic model uses experimental data to identify deformation beyond the elastic limit. For the elastoplastic materials, the uniaxial tensile test curve is shown in Figure 2.24.

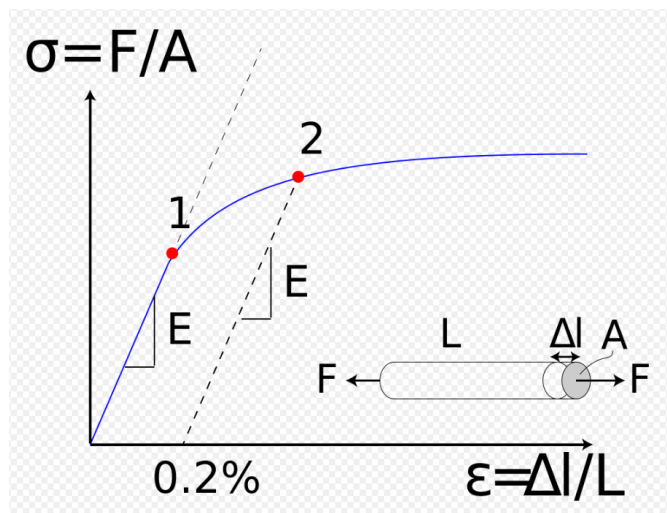


Figure 2.24: Stress-strain curve of uniaxial tensile test

(https://en.wikipedia.org/wiki/Stress%E2%80%93strain_curve)

It is assumed that yielding occurs only if the stresses σ satisfy the general yield criterion [110]:

$$F(\sigma, \kappa) = 0 \quad (2.59)$$

where κ is a “hardening” parameter.

Von Mises [111] pointed out that the basic behaviour defining plastic strain increments is related to the yield surface. If $d\varepsilon^p$ indicates the increment in plastic strain, then:

$$d\varepsilon^p = d\lambda \frac{\partial F}{\partial \sigma} \quad (2.60)$$

or, for component n ,

$$d\varepsilon_n^p = d\lambda \frac{\partial F}{\partial \sigma_n} \quad (2.61)$$

Here, $d\lambda$ is a proportionality constant that is undetermined. The rule is known as the normality principle because equation (2.60) can be explained as requiring the normality of the plastic strain increment “vector” to the yield surface in the space of n stress and strain dimensions.

By separately identifying a plastic potential, the limitations of the above rule can be removed using:

$$Q = Q(\sigma, \kappa) \quad (2.62)$$

which defines the plastic strain increment similar to equation (2.60), written as:

$$d\varepsilon^p = d\lambda \frac{\partial Q}{\partial \sigma} \quad (2.63)$$

The particular case of $Q = F$ is known as associated plasticity. The plasticity is non-associated when the relation is not satisfied.

During microscopic increment in stress, the changes in strain are assumed to be divisible into elastic and plastic parts. Hence,

$$d\varepsilon = d\varepsilon^e + d\varepsilon^p \quad (2.64)$$

The elastic strain increments are related to stress increments by a symmetric matrix of constants, i.e. D . Therefore, equation (2.64) can be combined with equation (2.63) as:

$$d\varepsilon = D^{-1}d\sigma + \frac{\partial Q}{\partial \sigma}d\lambda \quad (2.65)$$

The plastic increment in the strain will be present only when the “elastic” stress increment

$$d\sigma^e \equiv Dd\varepsilon \quad (2.66)$$

puts the stress outside the yield surface in the plastic loading direction. On the other hand, this stress change is such that if unloading occurs, then no plastic straining will be present. When plastic loading is occurring, the stresses on the yield surface are given by equation (2.59). This can be written as:

$$dF = \frac{\partial F}{\partial \sigma_1}d\sigma_1 + \frac{\partial F}{\partial \sigma_2}d\sigma_2 + \dots + \frac{\partial F}{\partial \kappa}d\kappa = 0 \quad (2.67)$$

or

$$\left\{ \frac{\partial F}{\partial \sigma} \right\}^T d\sigma - Ad\lambda = 0 \quad (2.68)$$

in which it makes the following substitution:

$$A = -\frac{\partial F}{\partial \kappa} \frac{d\kappa}{d\lambda} \quad (2.69)$$

Therefore, equation (2.65) and equation (2.68) can be written in a single matrix form as:

$$\begin{Bmatrix} d\varepsilon \\ 0 \end{Bmatrix} = \begin{bmatrix} D^{-1} & \left\{ \frac{\partial Q}{\partial \sigma} \right\} \\ \left\{ \frac{\partial F}{\partial \sigma} \right\}^T & -A \end{bmatrix} \begin{Bmatrix} d\sigma \\ d\lambda \end{Bmatrix} \quad (2.70)$$

The indeterminate constant $d\lambda$ can then be removed. This results in an accurate expansion that determines the stress changes in terms of imposed strain changes with

$$d\sigma = D_{ep}^* d\varepsilon \quad (2.71)$$

and

$$D_{ep}^* = D - D \left\{ \frac{\partial Q}{\partial \sigma} \right\} \left\{ \frac{\partial F}{\partial \sigma} \right\}^T D \left[A + \left\{ \frac{\partial F}{\partial \sigma} \right\}^T D \left\{ \frac{\partial Q}{\partial \sigma} \right\} \right]^{-1} \quad (2.72)$$

The elastoplastic matrix D_{ep}^* takes the place of the elasticity matrix D_T in incremental analysis. This matrix is symmetric only when the plasticity is associated. The matrix is defined even for ideal plasticity when $A = 0$. If hardening is considered, attention must be given to the nature of the parameter κ on which the shifts of the yield surface depend.

With “work hardening” material κ taken to be the amount of plastic work done during plastic deformation:

$$d\kappa = \sigma_1 d\varepsilon_1^p + \sigma_2 d\varepsilon_2^p + \dots = \sigma^T d\varepsilon^p \quad (2.73)$$

Using the flow rule, it is alternatively

$$d\kappa = d\lambda \sigma^T \frac{\partial Q}{\partial \sigma} \quad (2.74)$$

On substituting equation (2.74) with equation (2.69), it can be seen that $d\lambda$ disappears and it can be written as:

$$A = \frac{\partial F}{\partial \kappa} \sigma^T \frac{\partial Q}{\partial \sigma} \quad (2.75)$$

This assumes a determinate form if the explicit relationship between F and κ is known. A similar explanation is used for different hardening assumptions.

For some of the concepts that consider the Huber–von Mises yield surface with an associated flow rule, this is given by

$$F = \left[\frac{1}{2}(\sigma_1 - \sigma_2)^2 + \frac{1}{2}(\sigma_2 - \sigma_3)^2 + \frac{1}{2}(\sigma_3 - \sigma_1)^2 + 3\sigma_4^2 + 3\sigma_5^2 + 3\sigma_6^2 \right]^{\frac{1}{2}} - \sigma_y \equiv \bar{\sigma} - Y \quad (2.76)$$

in which the suffixes 1, 2, and 3 refer to the normal stress components and 4, 5, and 6, to shear stress components in a general 3D stress state. In the above equation, $\bar{\sigma}$ is the second stress invariant.

On differentiation, it can be found that

$$\frac{\partial F}{\partial \sigma_1} = \frac{3s_1}{2\bar{\sigma}}, \quad \frac{\partial F}{\partial \sigma_2} = \frac{3s_2}{2\bar{\sigma}}, \quad \frac{\partial F}{\partial \sigma_3} = \frac{3s_3}{2\bar{\sigma}}, \quad \frac{\partial F}{\partial \sigma_4} = \frac{3s_4}{2\bar{\sigma}}, \quad \frac{\partial F}{\partial \sigma_5} = \frac{3s_5}{2\bar{\sigma}}, \quad \frac{\partial F}{\partial \sigma_6} = \frac{3s_6}{2\bar{\sigma}} \quad (2.77)$$

where the dashes stand for deviatoric stresses:

$$s_1 = \sigma_1 - \frac{\sigma_1 + \sigma_2 + \sigma_3}{3} \quad (2.78)$$

The quantity $Y(\kappa)$ is the uniaxial stress at yield. If a plot of the uniaxial test giving $\bar{\sigma}$ versus the plastic uniaxial strain ε'_u is available and if simple work hardening is assumed, then

$$d\kappa = Y d\varepsilon_u^p \quad (2.79)$$

and

$$-\frac{\partial F}{\partial \kappa} = \frac{\partial Y}{\partial \kappa} = \frac{\partial Y}{\partial \varepsilon_u^p} \frac{1}{Y} = \frac{H}{Y} \quad (2.80)$$

where H is the slope of the plot at the particular value of $\bar{\sigma}$. On substituting this in equation (2.75), the following is obtained:

$$A = H \quad (2.81)$$

where H is known as the plastic modulus. This reconstructs the well-known Prandtl–Reuss stress-strain relation.

Plastic behaviour evaluated by irreversibility of stress paths and the development of permanent strain changes after a stress cycle can be described in a variety of ways. Another general and simple form is presented which assumes a priori the existence of an incremental relationship

$$d\sigma = D^* d\varepsilon \quad (2.82)$$

in which the matrix D^* depends not only on the stress σ and the state parameter κ but also on the direction of the applied stress (or strain) increment $d\sigma$ (or $d\varepsilon$). The dependence of D^* has 2 directions: loading and unloading. If in the general stress space it promotes the “loading” direction by a unit vector n given at every point, it can describe plastic loading and unloading by the sign of the projection $n^T d\sigma$. Hence,

$$n^T d\sigma > 0 \quad \text{for loading} \quad (2.83 \text{ a})$$

$$n^T d\sigma < 0 \quad \text{for unloading} \quad (2.83 \text{ b})$$

while $n^T d\sigma = 0$ is a neutral direction in which only elastic straining occurs.

Chapter 3. A critical analysis of pitting corrosion data of underground power transmission cables in the open literature

In this chapter, the pitting data obtained from open literatures as well as those measured by the Mechanical of Materials laboratory at the University of Leicester are presented. The pitting data for different cables are shown in Section 3.1. The measurement procedures to extract pit depth distribution are illustrated in Section 3.2 and the distribution of pit depth in different samples is shown in Section 3.3. The idea is to present a complete set of data and to determine the type of conclusions that can be obtained by examining at the data without any modelling. Also, this complete set of data is used to validate a model for long-term corrosion failure of underground cables.

3.1 Review of underground cables

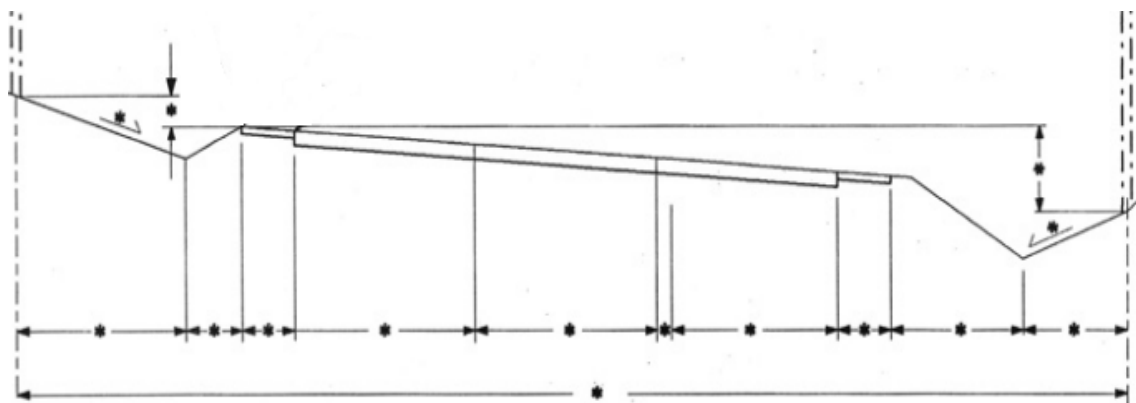


Figure 3.1: An example of route profile

(<https://connect.ncdot.gov/projects/construction/ConstManRefDocs/ENGINEERING%20CONTROL%20-%20VERIFICATION%20OF%20OVERHEAD%20MOUNTED%20SIGNS.pdf>)

f)

When the route plan is settled, a route profile is decided based on the static pressures in a cable system. Figure 3.1 shows the height of the cable at each point along the route. Based on report, it is easier to consider pressure as meters head of oil above a reference point in hydraulic design. Hence, the height of route shown in Figure 3.1 reflects the oil pressure and the route position of the underground power cable. The unit is chosen as the pressure in meters head of oil at any point in the route is the difference in the height of that point from the highest point without any pressure from the tanks. Normally, at the left hand end the cable is terminated by an outdoor sealing end while at the right-hand side of the profile the hydraulic section ends at a stop joint.



Figure 3.2: Excavation of underground cables

(<http://www.caseyelectricalservice.com.au/hydro-excavation/>)

If oil leakage of underground cables is detected, the failure cables can be dug out. Figure 3.2 gives a general view of the excavations carried out in pursuit of the oil leak.

A schematic drawing of the cable is given in Figure 3.3. A central oil duct is inside a copper conductor that carries the load current. The conductor is insulated using successive layers of oil impregnated paper tapes. Lead alloy is extruded to form a metallic sheath in order to retain the oil inside the cable. Due to the creep characteristics, the lead sheath is not able to hold the internal pressure alone [112], so reinforcing tin-bronze tapes are wound over it after a bitumen impregnated bedding tape has been applied.

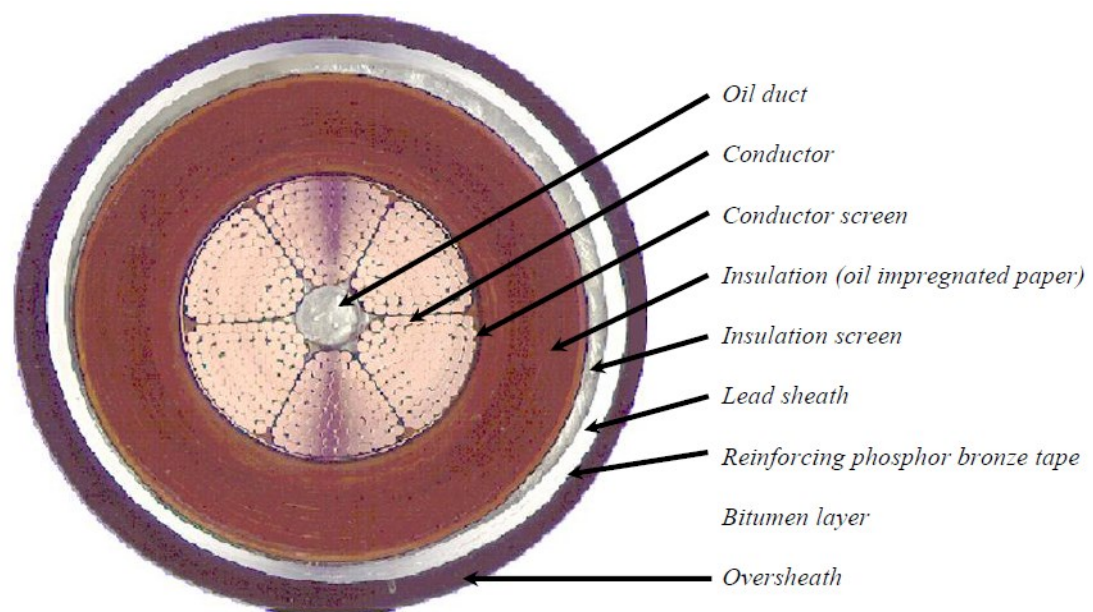


Figure 3.3: Schematic drawing of the power transmission cable. The tape is wrapped around the lead sheath [3]

The failure mechanism of reinforcing tin-bronze tapes is based on the assumption that corrosion fatigue will reduce the tapes strength to the point where they can no longer withstand the load imposed by the internal oil pressure within the cable and by the temperature variations due to the current rating. Once the tapes have failed the cable will fail within a few months' time. A sample of in service failed tape is shown in Figure 3.4. The outer surface of the tape is generally significantly stained and discoloured. Green and grey/black corrosion products are evident on the top surface. The inner tape

surfaces are relatively clean with only slight black discolouration, similar to that on the other side, along the edges of the tape. The staining is consistent with ingress of water into the cable reacting with the outside environment and diffusing around the edges of the tape to the inner side producing the characteristic tide marks. Removal of contamination products by inhibited HCl solution shows a typical pit distribution in a heavily corroded area of sample (Figure 3.5). Pits are randomly located on the surface of the failed tape. A sample of tape close to the fracture was cut into many pieces in a direction perpendicular to the applied load, i.e. along the tape width. The typical piece size is approximately 5 cm X 25.4 mm X 0.15 mm. The pieces were metallographically prepared as described earlier. Cross sections of the tape sample showed many shallow saucer and hemispherical pits with variable depths and widths. Figure 3.6 shows pits 20 μm deep and also 40 μm wide; it also shows how some pits coalesce to form bigger ones. Table 3.1 shows maximum pit depth examined from different circuits.



Figure 3.4: Optical image of outer and inner surface of the corroded tin-bronze reinforcing tape. The outer surface (a) is highly discoloured while the inner surface (b) shows only slight discolouration at the edges [3]

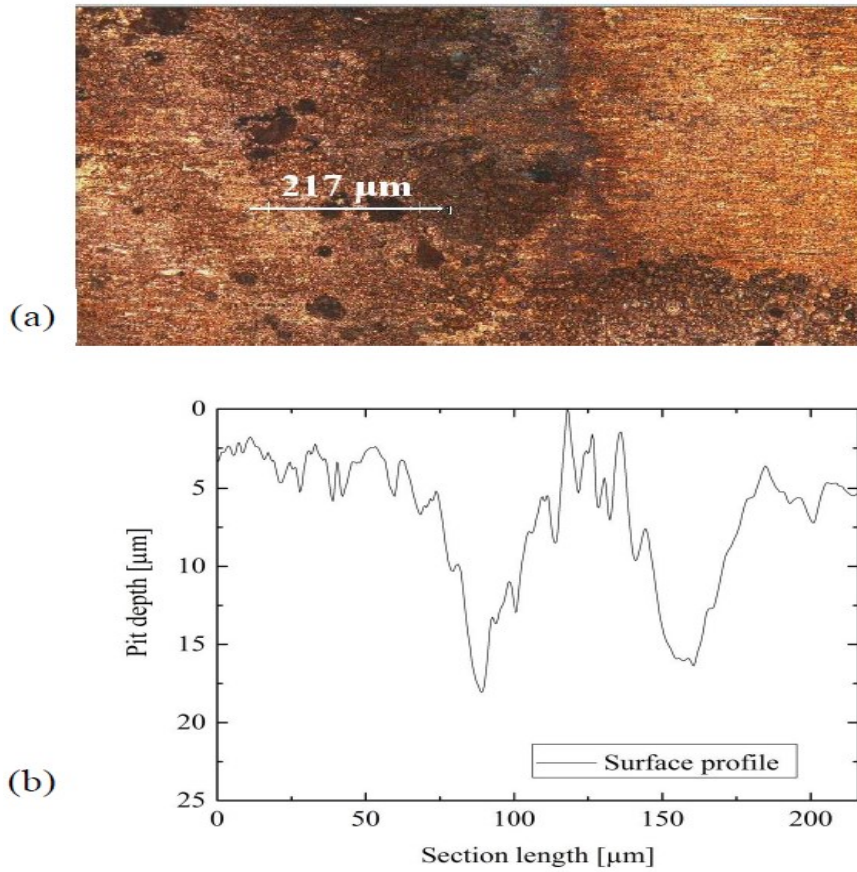


Figure 3.5: Pits on the outer surface of the tape cut through a line (a), and corresponding profile from 3D optical microscope (b) [3]

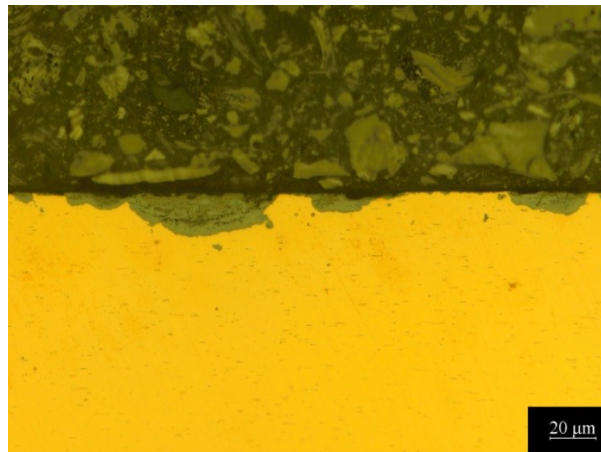


Figure 3.6: Cross section showing several pits with variable shape, taken perpendicularly to the longitudinal axis of the tape [3]

3.2 Process of copper dissolution and procedure to extract pit depth distribution

Before extracting pit depth from reinforcing tin-bronze tape, the mechanism of copper dissolution is presented first. The processes of copper dissolution in NaCl solution has been given major attention in the literatures [113-117]. This complicated and successive reaction relating to anodic dissolution is described in Figure 3.7.

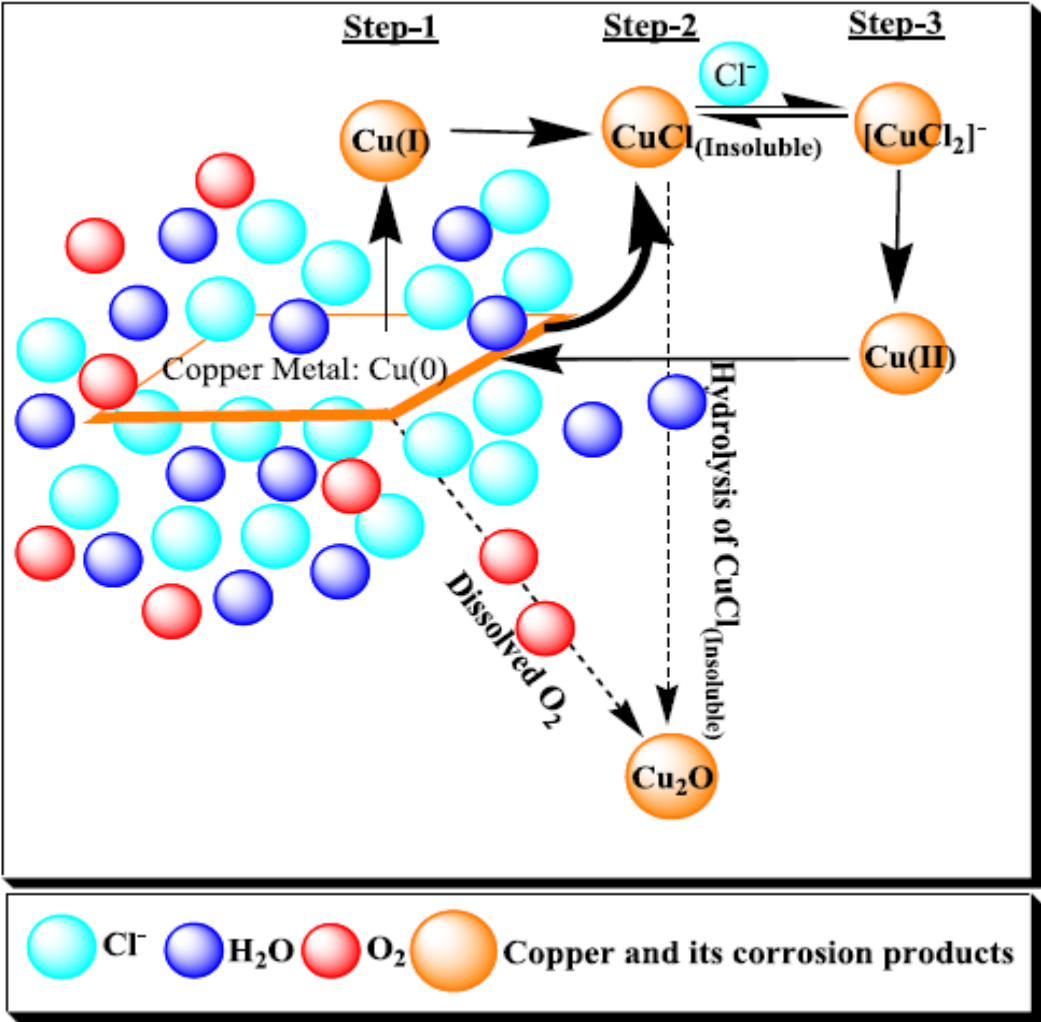
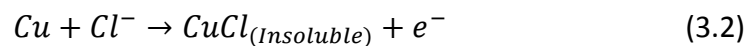


Figure 3.7: The mechanism of copper dissolution (anodic reaction) in NaCl solution

The anodic dissolution kinetics of Cu metal in NaCl solution are explained in 3 steps with their corresponding potential range as follows [118]:

Step 1: Active dissolution region (Oxidation of Cu (0) to Cu (I))

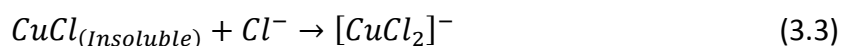
Cu ionized via an electron transfer in the existence of Cl^- as multiplex ions from test solution (3.5 wt.% NaCl), resulting the formation of insoluble cuprous chloride, $CuCl_{(insoluble)}$. In addition, a linear relationship between the potential and current density can be presented because of active dissolution. As a result, corrosion current density of blank copper gently rises to a relative high value with increasing anodic potential. Such result is due to the oxidation of Cu to Cu^+ which is explained in equations (3.1) and (3.2).



Step 2: Transition region (insoluble $CuCl_{(insoluble)}$ film formation and limiting current region)

Equation (3.2) indicates the formation of insoluble $CuCl_{(insoluble)}$ film formation under the assault of Cl^- , causing in low current density from the peak value. This ensures that prevention of Cu dissolution by a temporary passivating film of $CuCl_{(insoluble)}$.

Step 3: Conversion of the soluble copper (I) chloride complex



Equation (3.3) expresses the degradation of $CuCl_{(insoluble)}$ film and direct transformation into soluble $[CuCl_2]^-$ (cuprous chloride) complex at the interface of Cu metal due to poor stability and attachment ability of $CuCl_{(insoluble)}$. Finally, the consequent cuprous chloride

$[\text{CuCl}_2]^-$ complex diffuses into bulk of the solution and the corrosion current density again increases from minimum value to high anodic current density at high anodic potential.

Gnanasambandam and Foresta conducted experiments to investigate the pit depth of tape samples. Pit depth data extraction has 3 steps: tape cleaning, sample preparation, and pit depth measurement. With these 3 procedures, the methods discussed in the ASTM standard are outlined in the following [119].

i. Tape cleaning

ii. Sample preparation

The tape images before and after the cleaning are shown in Figure 3.8 (a) and 3.8 (b), respectively, and the mounted sample is shown in Figure 3.8 (c).

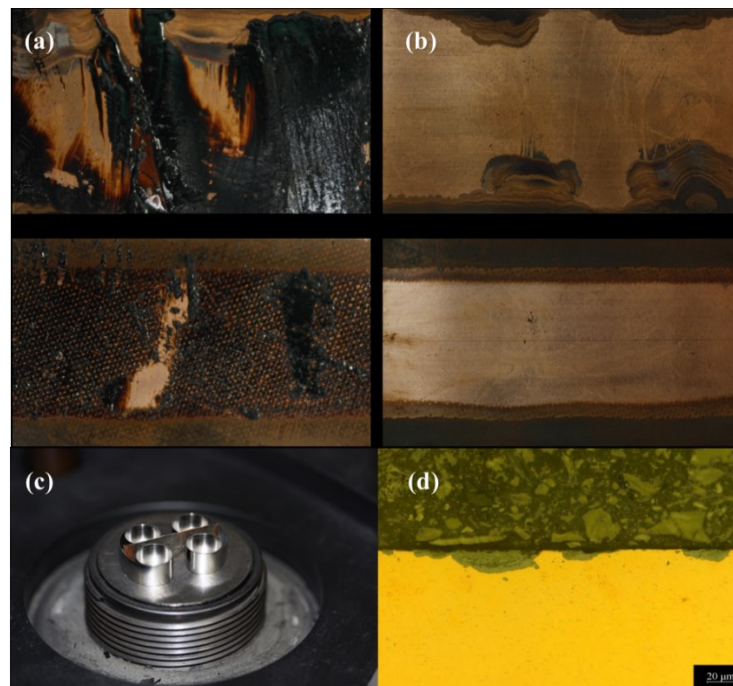


Figure 3.8: (a) Outer and inner surface of the tape covered with bitumen. (b) Outer and inner surface of the tape after bitumen removal with pentane. (c) Tape in the mounting machine. (d) Cross-sectional view of the corrosion pits taken perpendicularly to the longitudinal axis of the tape [1]

iii. Pit depth measurement

The procedure specified in the ASTM standard G46 [120] to measure pit depth.

3.3 Experimental pit depth distribution and analysis

Using Foresta's measurement [3], pit depth can be extracted from the various samples of reinforcing tapes by metallographic methods. The number of pits extracted was in the order of 10^3 . The samples from different sections of circuits had different pit depth distributions. Figure 3.9 shows the pit depth distribution from the ROUTE J. The sample size was about 2.5 cm × 2.5 cm, and the sample was divided to 4 smaller samples and polished to determine the pit depth. The pit depth from all the samples was greater than 10 μm as there were many particularly small pits (<10 μm) that could not be used to measure the pit depth distribution. For the 4 samples from the ROUTE J, the maximum pit depth was in the region of 35-40 μm and more than half of the pits were concentrated in the region of 10–15 μm. The reinforcing tapes taken from this circuit had been in service for more than 40 years. As the thickness of the sample was 0.15 mm, the maximum pit depth of the reinforcing tapes had reached 26.67% of the tape's thickness.

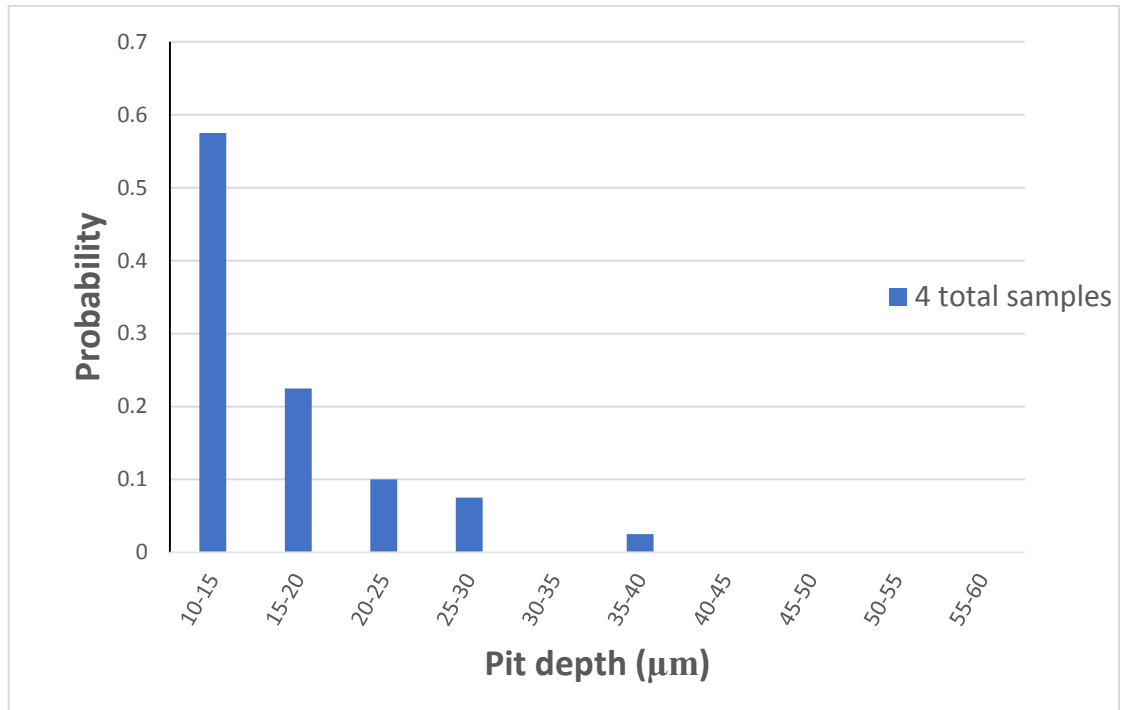


Figure 3.9: Pit depth distribution for samples from the ROUTE J circuit [3]

Figure 3.10 shows the pit depth distributions for reinforcing tape samples taken from the ROUTE F. There were 2 sets of samples from the same piece of tape and each sample was divided into 16 small pieces. The pit depth from all the samples was greater than 10 μm. The thickness of the samples was 0.15 mm. For sample A, the maximum pit depth was between 35-40 μm, reaching 26% of the tape's thickness. Most of the pits were concentrated at the region of 10–20 μm. Then, the number of pits dropped sharply for depths larger than 20 μm. For sample B, the maximum pit depth was 58 μm, which is the 38.7% of the tape's thickness. On comparing sample A and sample B, the pit depth distributions were fairly similar when the pit depth was relatively small (<20 μm). However, once the pits started growing deeper, sample A and sample B showed different maximum pit depths although these 2 samples were taken from the same section of the circuit. This may be because these 2 sets of samples had different corrosion levels. Moreover, it indicates that the samples measured may not contain the deepest pit depth of the reinforcing tapes. The sampled reinforcing tapes had been in service for more than 40 years.

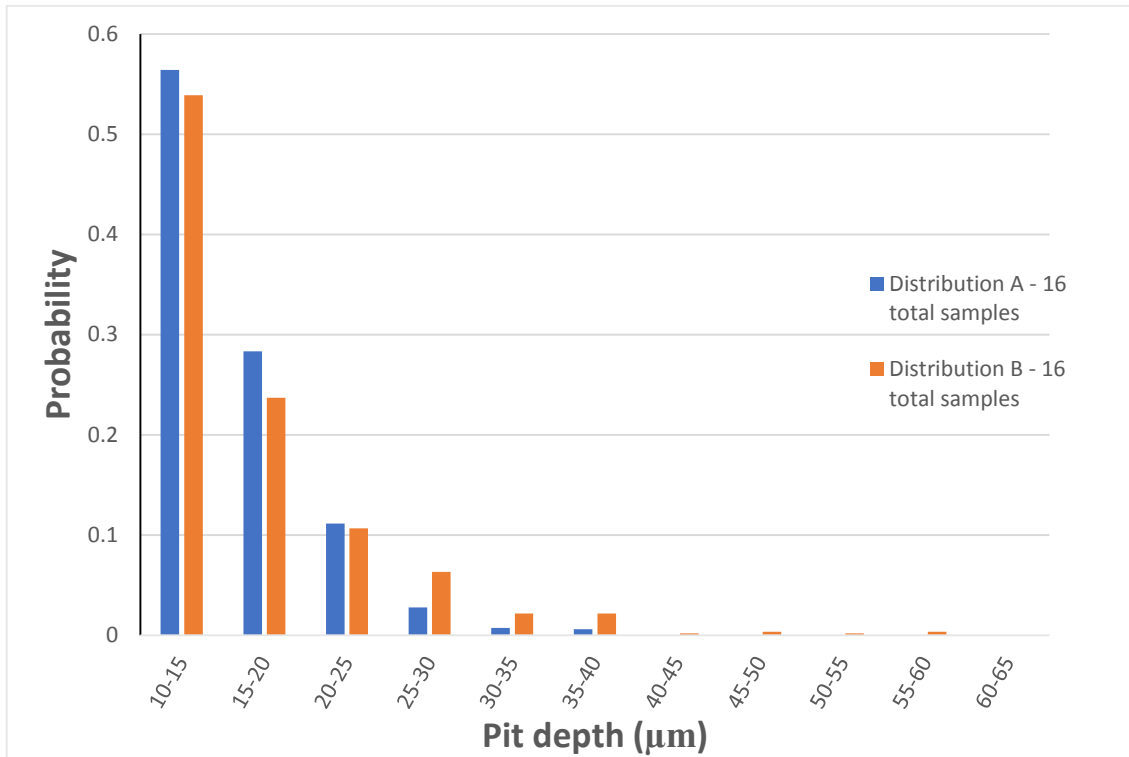


Figure 3.10: Pit depth distributions for 2 sets of samples from the same piece of tape in the ROUTE F circuit [3]

Figure 3.11 and Figure 3.12 show the pit depth distributions of samples taken from the ROUTE A. However, for this circuit, the samples were taken in different years (year 2008 and year 2014). In all, 16 samples were taken in year 2008 and 10, in 2014. The pit depth from all the samples was greater than 10 µm, and the thickness of the samples was 0.15 mm. Figure 3.11 illustrates the samples taken in 2008: The maximum pit depth is 35 µm, reaching 23.3% of the tape's thickness. Most of the pit depths were less than 20 µm, and very few pits penetrated the maximum depth. Figure 3.12 illustrates the samples taken in 2014: The maximum pit depth is 55 µm. Compared with the 2008 samples, the 2014 samples had few small pits and some of those small pits had grown to deeper pits. As mentioned in previous chapters, when the pits grow deeper, they have a higher probability of transforming to cracks, leading to the failure of reinforcing tapes. Therefore, the reinforcing tapes would face the problem of failure after being in service for a long time.

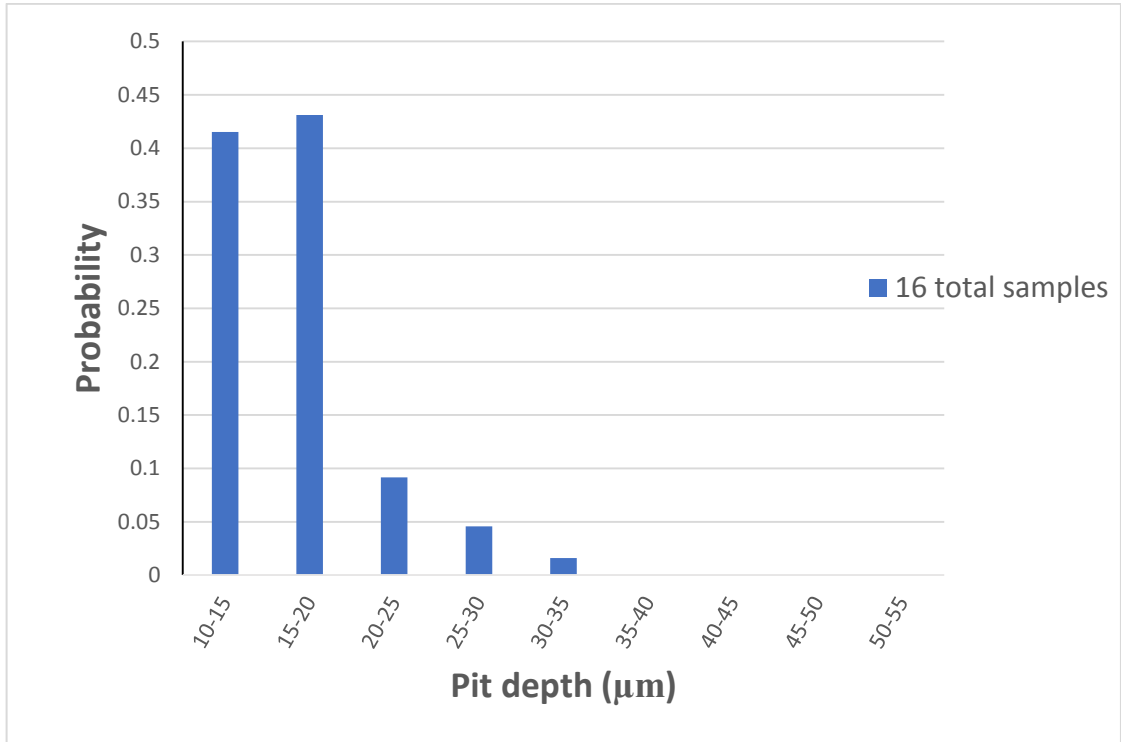


Figure 3.11: Pit depth distribution for samples from ROUTE A (year 2008) [3]

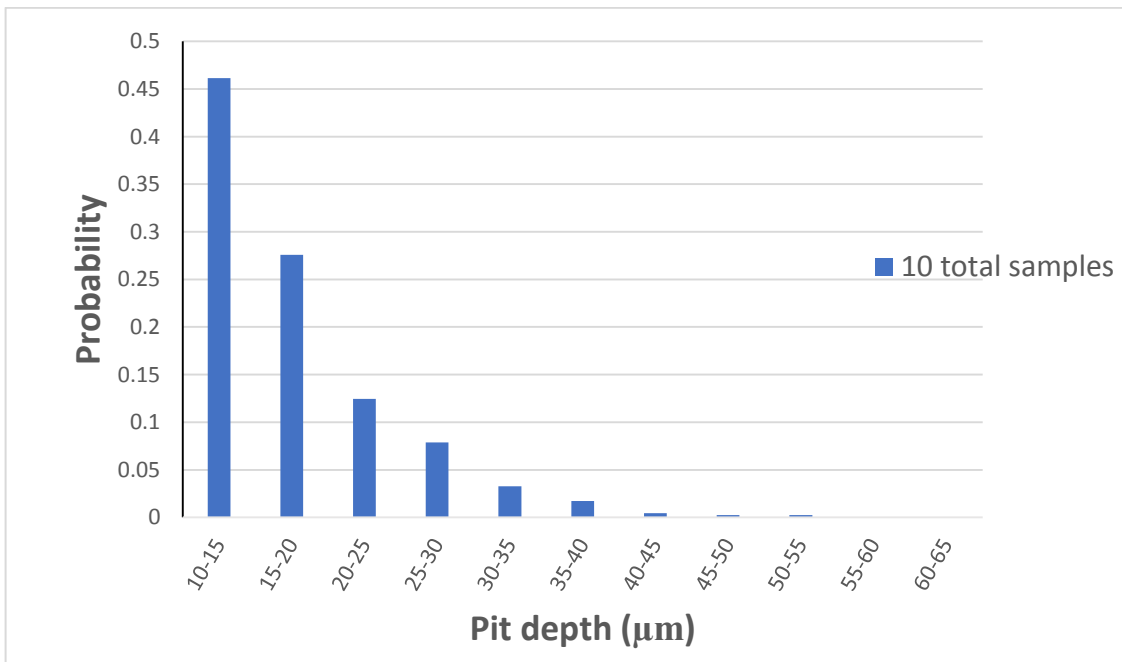


Figure 3.12: Pit depth distribution for samples from ROUTE A (year 2014) [3]

Figure 3.13 shows the pit depth distribution for samples from the ROUTE K. For simulating the distribution, 16 samples were taken from this circuit. In these 16 samples, the small pits less than 10 μm deep were counted because in some of the samples, the pits were evident, while in other sections, only generalised corrosion of small entities ($\leq 9 \mu\text{m}$) was observed. It appears that this type of corrosion lies between generalised and localised corrosion. Therefore, under this type of corrosion, the maximum pit depth was 23 μm , which was only 15.3% of the sample thickness. Figure 3.13 shows that most of the pits were concentrated at the region of 5-11 μm and only a few pits reached the deeper level. This circuit had been in service for more than 40 years. Unlike other circuits, the reinforcing tapes from the ROUTE K circuit are still in service and no significant failures occurred because of the low distribution of large pits.

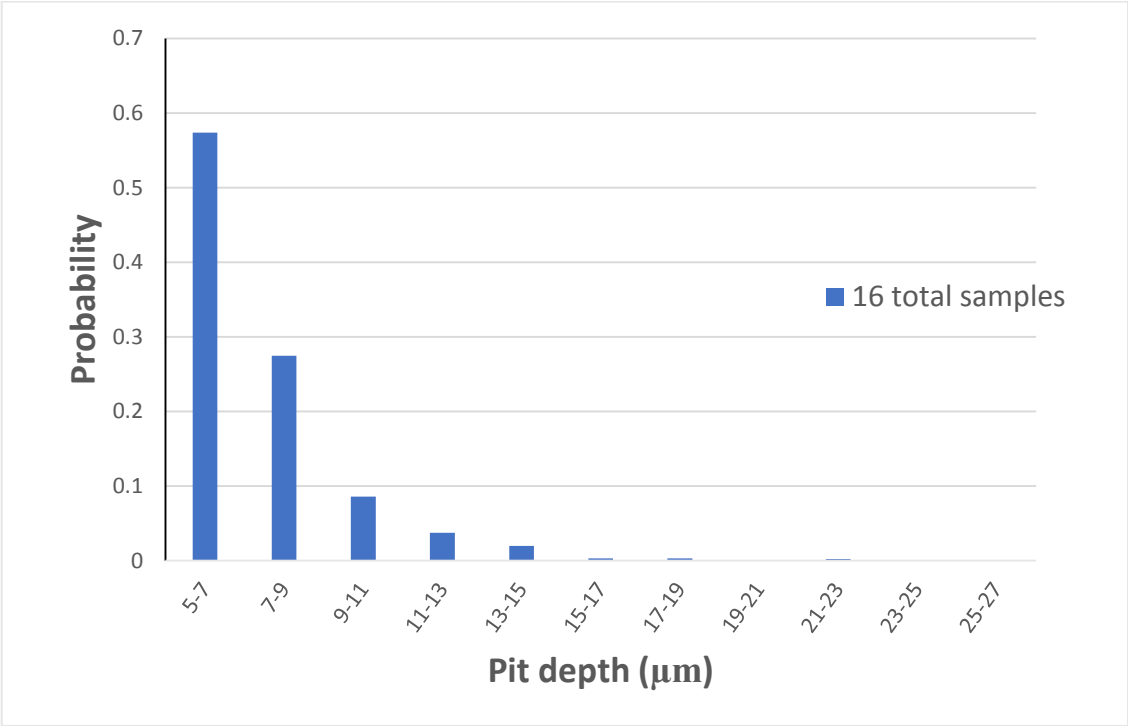


Figure 3.13: Pit depth distribution for samples from ROUTE K [3]

3.4 Key conclusions on the layout from the existing data

- a. Failed reinforcing tin-bronze tapes show highly discoloured outer surface and slightly discoloured inner surface at the edges.
- b. All fluid leakage will occur on sections with pit depth greater than 25% of tape thickness.
- c. For the reinforcing tapes from different cables and various sections, maximum pit depths are significantly distinct. The most corroded tape could be penetrated by pitting corrosion to 60% of its thickness.
- d. The difference in maximum pit depth among the cables may be caused by localised temperature, oil internal pressure, and presence of water.
- e. The maximum pit depth of tape samples may not reflect the deepest corrosion pit owing to the limitations of the measurement procedure. Moreover, the tape samples may not contain the deepest pit for the entire cable route.
- f. Pits growth rate is a time-dependent function, and pits grow with time increasing.

3.5 Summary

By examining the pitting data, the results show that for underground power transmission cables that have been in service for more than 40 years, different levels of corrosion occurred in all the reinforcing tin-bronze tapes. The worst situation of pit penetration was 38.7% of the tape thickness, indicating that the reinforcing tapes were corroded with significant pit depth. Concerning the 2 sets of samples taken in 2008 and 2014 from the ROUTE A circuit, the maximum pit depth was found to have increased with time increasing. Also, the number of relatively large pits (>20 μm) had increased with time. Based on these observations, pit growth rate is considered a time-dependent function and the pit depth increases with time increasing. For all the different circuits, the pit depth distributions are not similar because the samples of circuits are from different places. Each circuit has its own soil conditions, working environment, and

temperature. Generally, for all the circuits, the soil conditions, temperature, and water diffusion play major roles in pitting corrosion and failure of reinforcing tapes. Figure 3.10 shows that the distribution of pits in 2 different sets of samples was not same despite the samples being taken from the same circuit. These results illustrate that even for samples from the same circuit, the distribution may not be the same because of the differences in the localised environment such as water diffusion and lead sheath failure or other uncertain factors like scratches on the reinforcing tapes when they were set up. Although the pitting corrosion data may not be accurate, they can reflect the failure probability of each cable.

Chapter 4. The Monte Carlo model of pitting corrosion

To predict pitting corrosion, a computational model will be used that details the mechanisms of pitting corrosion and the Monte Carlo method. Here, the aim is to simulate the pit depth with a reliable mechanism and to use the Monte Carlo method to reduce the uncertainty during the pitting corrosion process. The literature review identified that the computational model developed by Engelhardt and Macdonald [29] can simulate the processes of pit nucleation, propagation, and repassivation, and therefore the model used in this chapter is based on that of Engelhardt and Macdonald [29], who simulated pitting corrosion with an aluminium alloy. Moreover, Newton's method is added to this computational model to complete the root finding aspect. The parameters are not complicated for this computational model; most of them depend on the properties of the reinforcing tape, which means that unlike the model developed by Velázquez et al. [12], the parameters used in this computational model can be obtained conveniently. The difference between Engelhardt and Macdonald's work and the Monte Carlo model is that this computational Monte Carlo model is used to check if the model is valid for long-term pitting growth data, while Engelhardt and Macdonald's model simulated short-term pitting corrosion for only 300 days.

After simulating the MC model, the results of the computational model are compared with the experimental data measured in the laboratory. After comparing these two sets of data, several parameters of computational model were changed to identify how they were affecting the prediction of the results because experimental data from different cables and pit depth distributions may differ. Therefore, the computational results need to be examined by means of different samples to evaluate whether the unique parameters are suitable for different cases. Moreover, the computational model will be validated by using the pit depth distribution of different service durations to determine

whether the model can simulate pit occurrence or growth, accurately for reinforcing tin-bronze tapes.

4.1 Computational methodology

It is important to note that for pitting corrosion, only a few pits or even a single pit may be alive on the corroding metal surface at the same time. In this situation, the differential equations that are equivalent to a balance equation for particles in discontinuous media for the damage function could lose their strict physical meaning. The main idea behind the Monte Carlo method for pitting corrosion is to keep track of each stable pit that has nucleation, propagation, and repassivation stages on the metal surface.

According to the mechanism of pitting corrosion, pit nucleation plays an important role during the process. Before the pit nucleates, it has to penetrate the passive film on the metal surface, but this penetration depends on the concentration of aggressive anions, the moisture concentration, and soil conditions. These environmental factors can affect the pit nucleation rate, and also bring significant uncertainties. For this reason, the Monte Carlo method is used to simulate the probability of pit nucleation for each independent pit, and thereby reduce these uncertainties. Given the probability of pit nucleation, all pits have the same nucleation priority, but they can nucleate at different dissolution times. Furthermore, the probability of pit nucleation can indicate that all pits will nucleate after a certain period of dissolution.

Pit repassivation is another significant factor that can affect pit depth during the entire pit growth process. The mechanism of pit repassivation is complicated, depending on the pitting potential, localised chemistry, chemical nature of the aggressive inclusions (sulphide or chloride), and the pit shape or size. A pit could stop growing at any time

when it meets any of the above conditions, and because of these uncertainties, the Monte Carlo method is used to simplify the process of pit repassivation. The purpose behind this method is to assume each independent pit has a same probability of pit repassivation during the entire growth process, and a random number is generated to compare the probability. The outcome of this comparison determines whether a pit will continue to grow. Since this result is random, a large amount of repeatable data can more accurately describe the mechanism of pit repassivation.

The aim of this section is to model pit growth with a reinforcing tin-bronze tape surface through three stages: pit nucleation, propagation, and repassivation. The key issue is to check if this model is valid for long-term data for pitting growth. An outline of the computational Monte Carlo method is illustrated as follows:

1. Pit nucleation: The probability that the pit that will nucleate in a stable form during the period step dt is being introduced. The parameters for the PDM (τ , a , and b) were chosen arbitrarily, and the aim was only to make sure that all stable pits had nucleated within a certain time. Then, a random number $0 \leq G_k \leq 1$ is generated for each pit that has not yet been born, and make a comparison between G_k and P_{nucl} to determine if the pit can nucleate.
2. Pit propagation: The depth of the j -th stable, living pit a_j is calculated using Faraday's Law. To calculate the value of the average potential drop $\Delta\phi_j$ faster and more accurately, Newton's method has been chosen as the principle method.
3. Pit repassivation: The probability of repassivation is given by $P_\gamma = \gamma dt$, where γ is the delayed repassivation constant. Then, for the j -th living pit for each time step, the random number $0 \leq G \leq 1$ is generated. The random number G then needs to be compared with P_γ . Therefore, for a pit to be considered repassivated, the value of $a_j(t + \Delta t)$ will be equal to $a_j(t)$.

The computational model consists of three stages, shown in the flowchart (Figure 4.1) and are explained in detail below, based on Engelhardt and Macdonald [29]. The meaning of all the symbols involved is illustrated in Section 2.6.

Stage 1: Pit nucleation

Initially, it is assumed that the total number of stable pits that can nucleate on a metal surface of a total area is N_0 , and the probability of a pit that will nucleate in a stable form during the time step dt is given by:

$$P_{nucl} = \frac{N(t+dt) - N(t)}{N_0 - N(t)} \quad (4.1)$$

$N(t)$ is the number of stable pits that can nucleate within a time interval of between 0 and t . The number of stable pits $N(t)$ is calculated by the following equation:

$$N(t) = N_0 \operatorname{erfc}\left(\frac{a}{t-\tau} + b\right) / \operatorname{erfc}(b) \quad (4.2)$$

where τ is the dissolution time, and a and b are the constant values. The parameters for the PDM (τ , a , and b) are chosen arbitrarily and the aim behind this is to make sure that all stable pits have nucleated within one year. Because the value of dissolution time is uncertain, three different values (three days, 100 days, and 300 days) have been chosen in the computational simulation model to determine the best dissolution time for this Monte Carlo model. Then, a random number $0 \leq G_k \leq 1$ is generated for each pit k that has not yet been born. Comparing G_k with P_{nucl} , there are two conditions that need to be considered:

i. A pit is considered to have been born with a pit depth of $x=0$ $G_k \leq P_{nucl}$ (4.3 a)

ii. It has not been born, and will be examined in the next time step $G_k > P_{nucl}$ (4.3 b)

Stage 2. Pit propagation

For the following each time step, the depth of the j -th stable, living pit, a_j , can be calculated using Faraday's Law:

$$a_j(t + dt) = a_j(t) + K_V i_j(t) dt \quad (4.4)$$

In the above equation, the parameter i_j is defined by Tafel's law for the active metal dissolution current density as:

$$\text{i. } i_j = i_0 \exp\left(-\frac{\alpha F \Delta \phi_j}{RT}\right) \quad \text{at } \Delta \phi_j < \Delta \phi_{cr} \quad (4.5 \text{ a})$$

$$\text{ii. } i_j = 0 \quad \text{at } \Delta \phi_j \geq \Delta \phi_{cr} \quad (4.5 \text{ b})$$

The value of $\Delta \phi_j$ is determined by a numerical solution of the equation:

$$\Delta \phi_j = \frac{b a_j i_0}{\kappa} \exp\left(-\frac{\alpha F \Delta \phi_j}{RT}\right) + \sum_{k \neq j} \frac{i_0 a_k^2}{\kappa d_k} \exp\left(-\frac{\alpha F \Delta \phi_k}{RT}\right) \quad (4.6)$$

Based on the experiment data of extraction of pits on the corroded reinforcing tape, the sample size was about 5 cm x 2.5 cm, and 2,346 pits were found in this sample. Assuming that there are no overlapping pits, the area of each can be calculated as 730 μm x 730 μm . To simplify the Monte Carlo model, the area of each pit is defined as 1000 μm x 1000 μm without interaction and the pits are located in the centre of these squares with total number equals to 100. The Cartesian coordinates X_i and Y_j are declared as the position of each pit which the point (X_i, Y_j) lies in the centre of the square and the index $i, j = 1, 2, \dots, 10$. Therefore, the distance between two pits can be

defined as $d_k = 1000 \times \sqrt{(X_i - X_m)^2 + (Y_j - Y_n)^2} \mu\text{m}$ where $i \neq m$ and $j \neq n$.

Newton's method has been chosen as the principle method of solving this equation [121]. Using Newton's method, equation (4.6) can similarly be considered in the form

$x = a \cdot \exp(bx) + c$, where x stands for the value of $\Delta\phi_j$. Then, the equation can be rewritten as follows:

$$F(x) = a \exp(bx) - x + c \quad (4.7)$$

The derivative $F'(x)$ is written as:

$$F'(x) = ab \exp(bx) - 1 \quad (4.8)$$

According to equation (4.6), it shows that $a > 0, b < 0$. In this situation, $F'(x)$ is always less than 0, which means $F(x)$ is a monotonically decreasing function. In the interval $[0, +\infty]$, for $x = 0, F(0) = a + c > 0$, while for the positive infinite of $x, F(x)$ is less than 0. In other words, the value of the function $F(x)$ at one endpoint of the interval is positive, and at the other endpoint it is negative. For the function $F(x)$, there is only one root $\hat{x} \in (a, b) : F(\hat{x}) = 0$. By combining equations (4.7) and (4.8), the calculation of the average potential drop can be rewritten as:

$$x^{(p+1)} = x^{(p)} - \frac{a \exp(bx^{(p)}) - x^{(p)} + c}{ab \exp(bx^{(p)}) - 1} \quad (4.9)$$

In stage 2, $x = 0$ is chosen as the starting point, and the value of $x^{(p)}$ is then iterated step by step. The total number of steps for iteration has been chosen as 20 for each time step. Once the value of $\Delta\phi_j$ has been estimated, the values of i_j and $a_j(t + \Delta t)$ can be calculated in the following time step.

Stage 3: Pit repassivation

For each time step, the programme needs to consider the probability of pit repassivation. This is given by $P_\gamma = \gamma dt$, where γ is the delayed repassivation constant. Practically speaking, for the j -th living pit in each time step, the random number $0 \leq$

$G \leq 1$ is generated. Furthermore, the random number G needs to be compared with P_γ .

i. The pit is considered alive when entering the next time step $G > P_\gamma$
(4.10 a)

ii. The pit is considered to have passivated and stopped growing $G \leq P_\gamma$
(4.10 b)

Therefore, when a pit is considered to have stopped growing, the value of $a_j(t + \Delta t)$ is equal to $a_j(t)$.

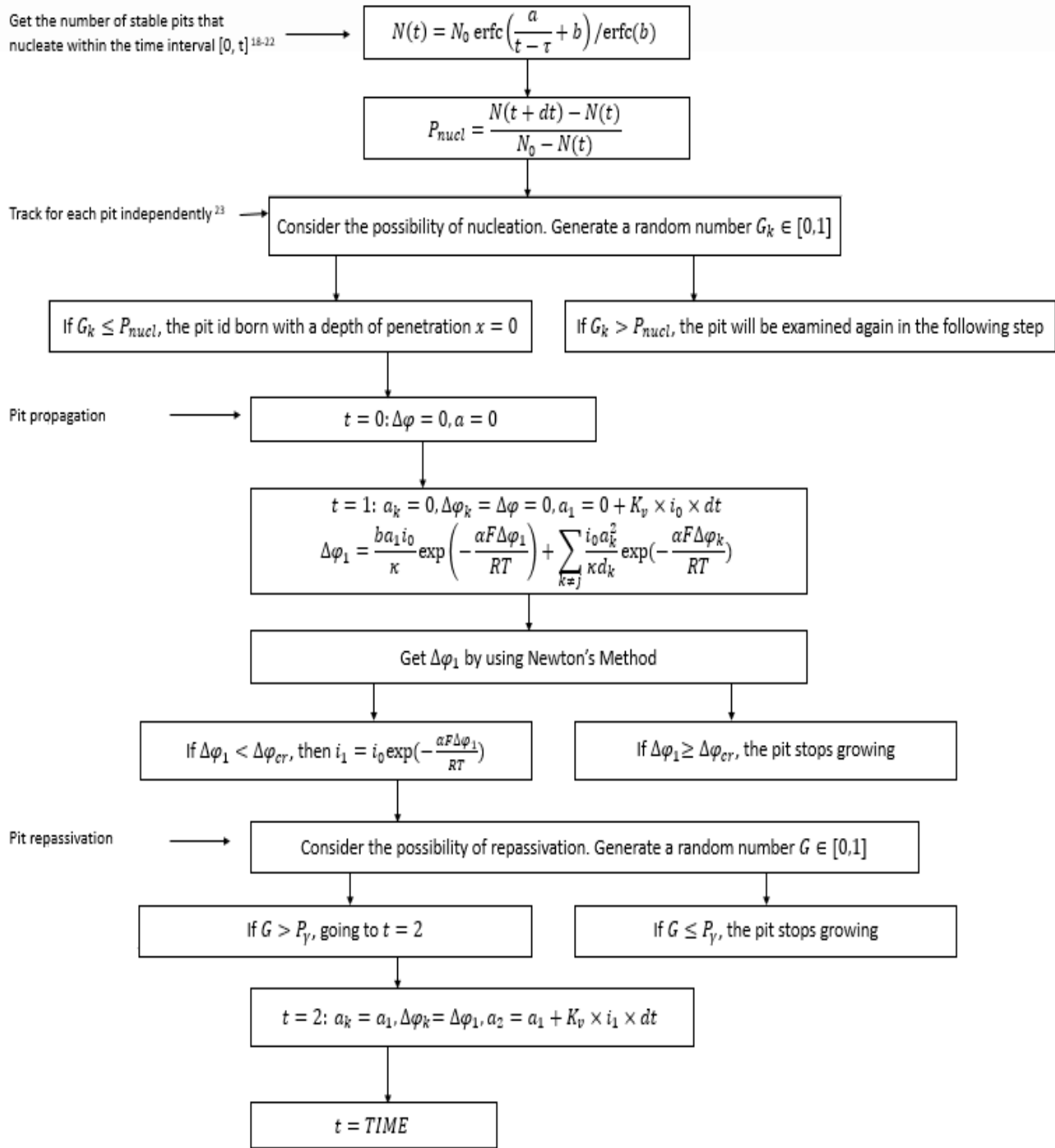


Figure 4.1: The flow chart of programmes for tracking each individual pit

4.2 Material properties

The computational model using the Monte Carlo method is performed to calculate the pit depth by looking at all three stages of growth – nucleation, propagation, and repassivation (which decides whether the pits continue to grow or stop randomly). In the Monte Carlo simulation model, the initial conditions of pit depth and potential drop are 0, while the initial current density is equal to the exchange current density ($a = 0, \Delta\varphi = 0$ and $i = i_0$). The other parameters of the reinforcing tapes that need to be known for the model calculations are shown in Table 4.1.

i_0	0.15 A m^{-2}
K_v	$2.834784 \times 10^{-5} \text{ m}^3 (\text{A} * \text{day})^{-1}$
α	1
κ	$0.2 \times 10^{-4} \text{ A (V} * \text{m)}^{-1}$
$\Delta\varphi_{cr}$	0.2 V
T	298.15 K
γ	0.166 day^{-1}
b	2.1
F	$96,485.3365 \text{ C mol}^{-1}$
R	$8.3144621 \text{ J K}^{-1} \text{ mol}^{-1}$
Time	14,600 days

Table 4.1: Parameter values for model calculations

In Table 4.1, i_0 is the exchange current density [122]; K_v is the electrochemical equivalent volume of copper [123]; α is the anodic transfer coefficient; and κ is the conductivity of localised water. The value of $\Delta\varphi_{cr}$ is assumed by King et al. [124] and Sourisseau et al. [125]. Furthermore, b is a constant value [31]; T is the Kelvin

temperature, F is Faraday's constant, and R is the gas constant. The value for the delayed repassivation constant, γ , is illustrated by Engelhardt and Macdonald [29].

4.3 Results comparison and Monte Carlo model validation

In this Monte Carlo simulation, pitting corrosion is assumed to occur on the reinforcing tin-bronze tapes under the condition of low water concentration. In addition, the total time for pit growth is equal to 14,600 days (40 years), and the $\Delta t = 1$ day. Furthermore, the simulation is to be run 1,000 times and each time, the total number of pits is 100, to obtain more acceptable and accurate results.

In order to track the deepest value the pit depth can reach, the pit repassivation stage is ignored and the pit is assumed to continue growing as the time increases. Figure 4.2 shows how the pit grows without pit repassivation. After 560 days of growth, the pit can reach a maximum pit depth of 150 μm . In previous sections, it was shown that in empirical models, the pit depth follows the equation $d_{max} = kt^{\nu}$. The value of power ν is between 0.3 and 1. By adding the trendline to the results, it can be seen from Figure 4.2 that the analogous function of the curve is $F(x) = 3.7611x^{0.583}$. Compared to the empirical equation, the power 0.583 is placed within the interval [0.3, 1]. When results are acceptable, as Figure 4.2 shows, the pit growth rate is not constant. If pit repassivation is considered, the pit can stop at any time in the 560 days. In other words, the pit depth can be located at any point at the curve of 'the MC results' when pit repassivation occurs.

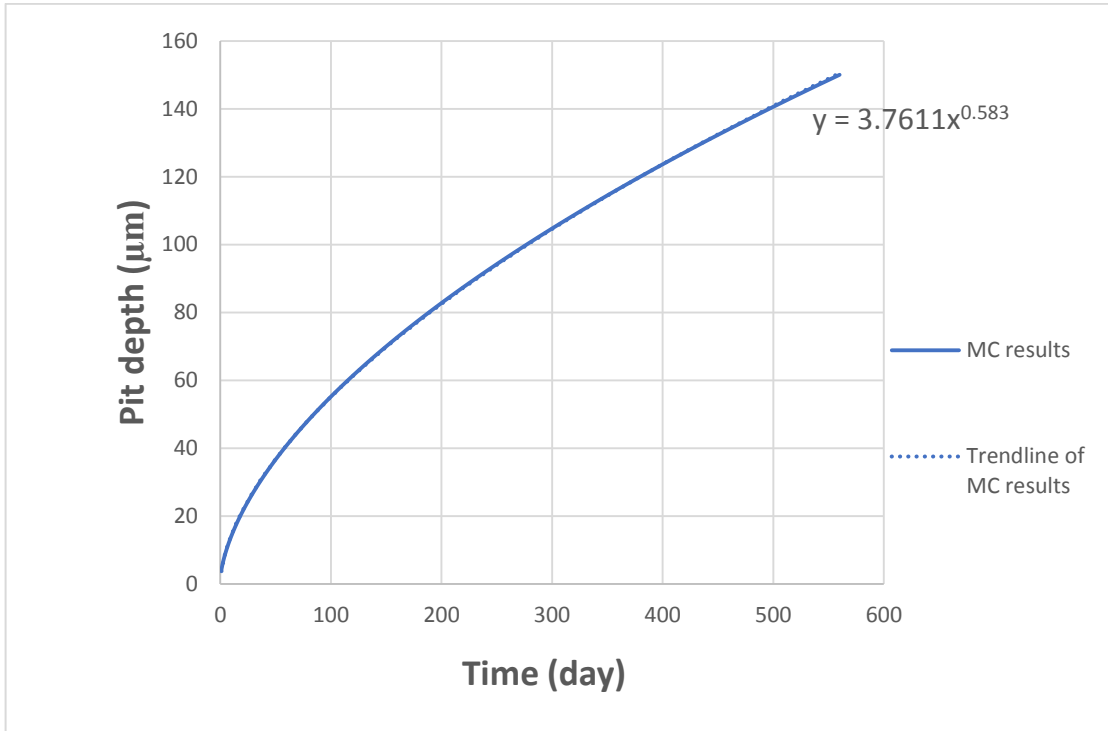


Figure 4.2: Pit depth without repassivation occurring

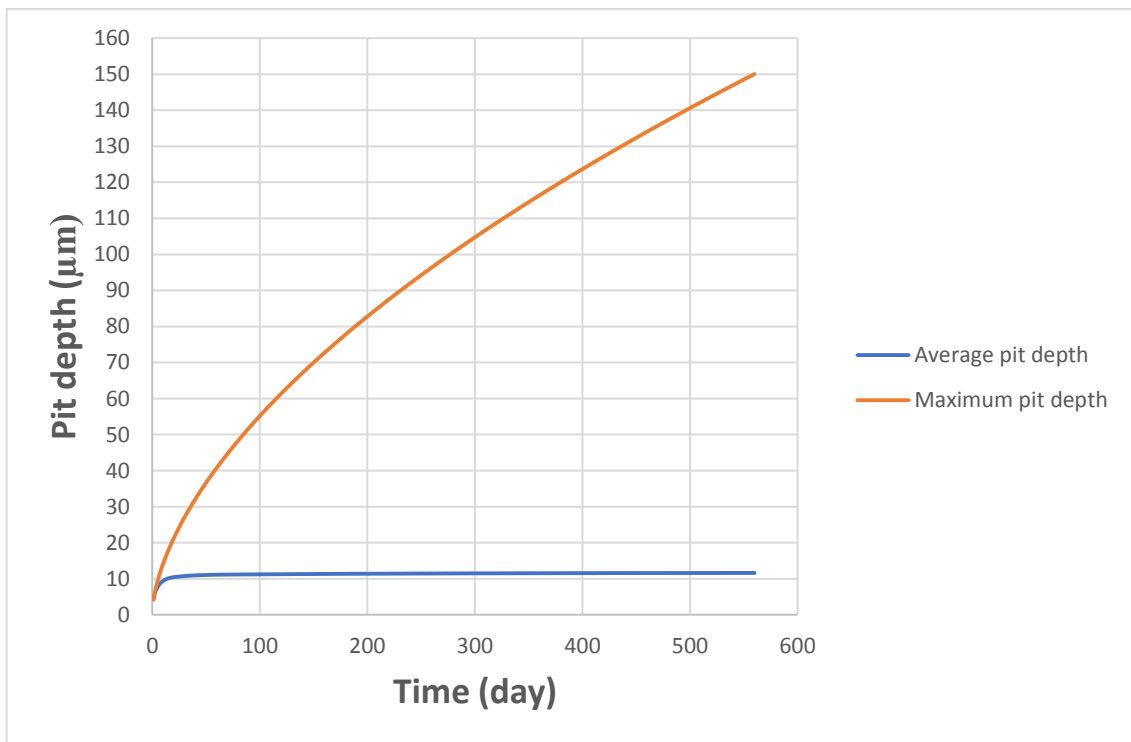


Figure 4.3: A comparison between maximum and average pit depth

Figure 4.3 shows a comparison of results between maximum and average pit depth for a given simulation time 560 days by using Monte Carlo simulation. The total number of pits for simulating is 10^5 . It can be clearly seen that the maximum pit depth indicates the pit continue growing as the time increases without repassivation. Comparing with the maximum pit depth, the average pit depth has significantly difference value and much lower than the maximum pit depth. This comparison shows that for such large amount of pits, most of the pits can only reach to a small depth or even without growing due to pit repassivation. In addition, the results in Figure 4.3 illustrate that the vast majority of pits can only grow for a short period of time, and then stop growing under the influence of repassivation. Figure 4.4 clearly shows that the all the pits can propagate at the beginning, and then most of the pits repassivate in a short period of time. After about 100 days, almost all the pits have stopped propagating and only a few pits can continue growing in the following simulation time. This figure illustrates the reason why the average pit depth is much smaller than the maximum value in Figure 4.3 from another side.

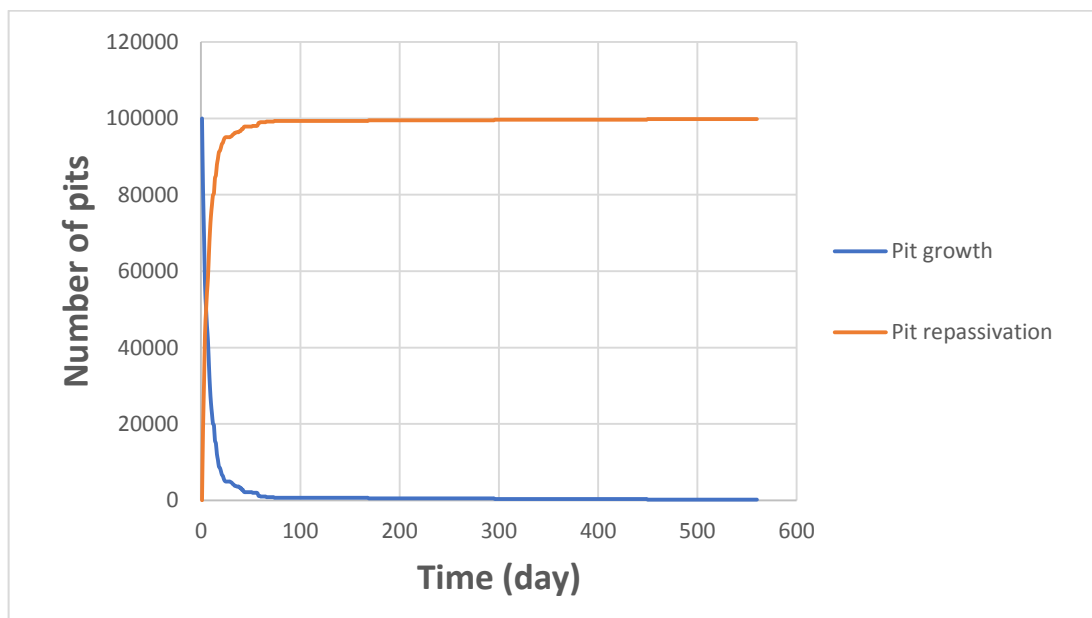


Figure 4.4: Number of pits for pit growth and pit repassivation within 560 days

Figure 4.5 shows the results of the pit depth distribution after applying the pit repassivation stage using the Monte Carlo simulation. It can be clearly seen that most of the pit depths are concentrated in the region of 10-25 μm in a pit growth time of 14,600 days, which means that the pits stop growing before they have reached to the deepest value of pit depth (75 μm). According to this distribution, few pits can reach the deepest depth, and most only grow to a depth of 40 μm before they are repassivated. Furthermore, no pits exist in the region of 50-70 μm , therefore each independent pit has a high probability of reaching a depth of from 10 to 25 μm , and there is a significantly low probability that it will continue growing without repassivation occurring. As a result, when a pit has a relatively small depth, it can repassivate more easily, and once a pit reaches a deeper depth, it has a higher probability of continuing to grow without stopping.

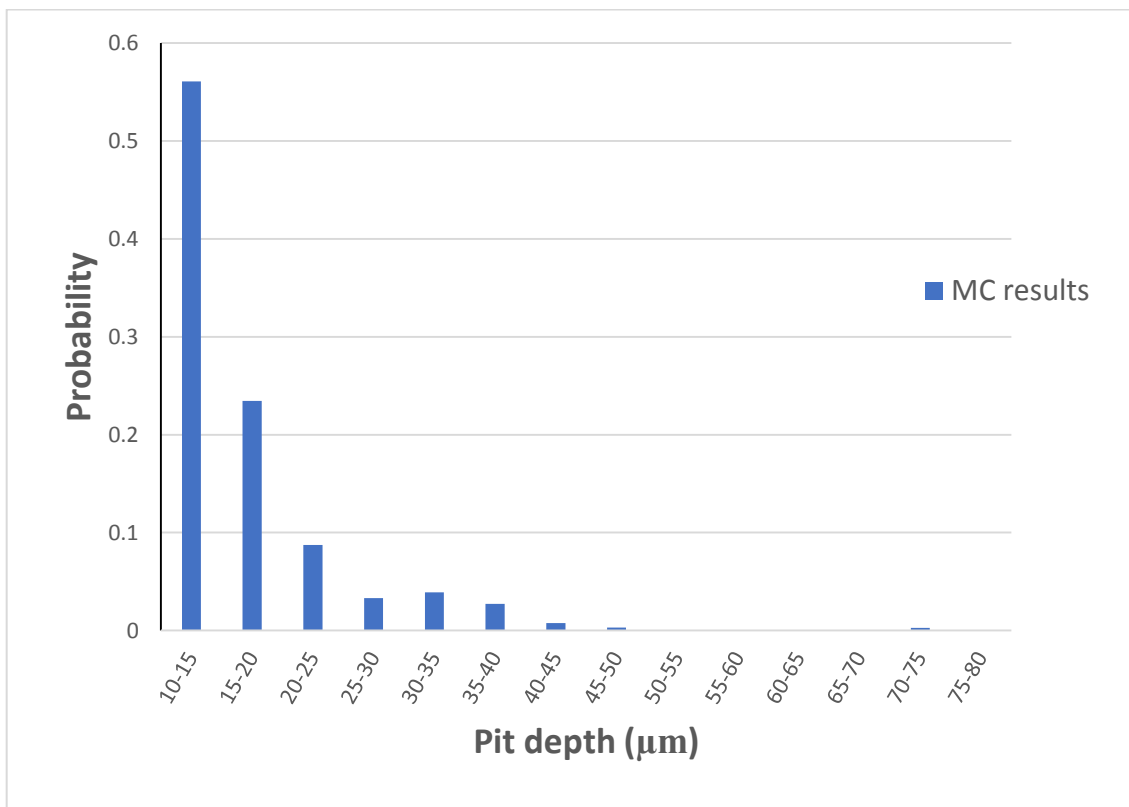


Figure 4.5: The pit depth distribution of Monte Carlo simulation results

Tape samples from different locations on the failed cables are examined to find out the pit depth distribution, using metallographic methods outlined by Mr Foresta. Two sets of data are taken for the same tape surface of a service age 40 years from the ROUTE F circuit, as shown in Figure 3.9. There are two sets of data from a total of 16 samples taken from the same piece of tape; the total number of pits on these datasets are 553 and 826, respectively, and the pits are only counted when they have a depth larger than 10 μm . The results emphasise that similar pit depth distributions are observed in the samples taken from same tape in different parts, which gives further confidence in a comparison with the simulation model.

Pit growth is modelled using the Monte Carlo method, as explained in Section 4.1. At known time $t = 14600$ days and total number of pits = 1000×100 , the critical parameters are set as dissolution time = 100 days, temperature = 298.15 K, and repassivation constant = 0.166; this is used to match the failed tapes pit depth distribution shown in Figure 4.5. Similarly, the pits are only counted when the depth is larger than 10 μm .

Figure 4.6 shows the pit depth distributions of two sets of samples from the ROUTE F circuit against the distribution of the Monte Carlo method. Figure 4.5 shows that the maximum pit depth can reach 75 μm . However, only a few pits can reach that maximum value, and no pit occurs with a depth from 50 μm to the maximum depth. As discussed in Chapter 3, the experimental data may not completely reflect the maximum pit depth for the corroded reinforcing tapes, and therefore in order to facilitate a comparison between the experimental data and the computational data and to reduce the source error, the pit depth distributions are simplified to between a depth of 10 and 80 μm . It can be observed that there is a trend of pit growth, such as the appearance of a relatively high probability for the smaller pits, but this probability decreases sharply with an increased depth of pit, which is consistent with both the simulated and experimental pit depth distributions. It proves that the model can predict the distribution of pit depth effectively in the critical parameters of dissolution time,

temperature, and repassivation constant (which decides whether all the pits continue to grow or stop randomly).

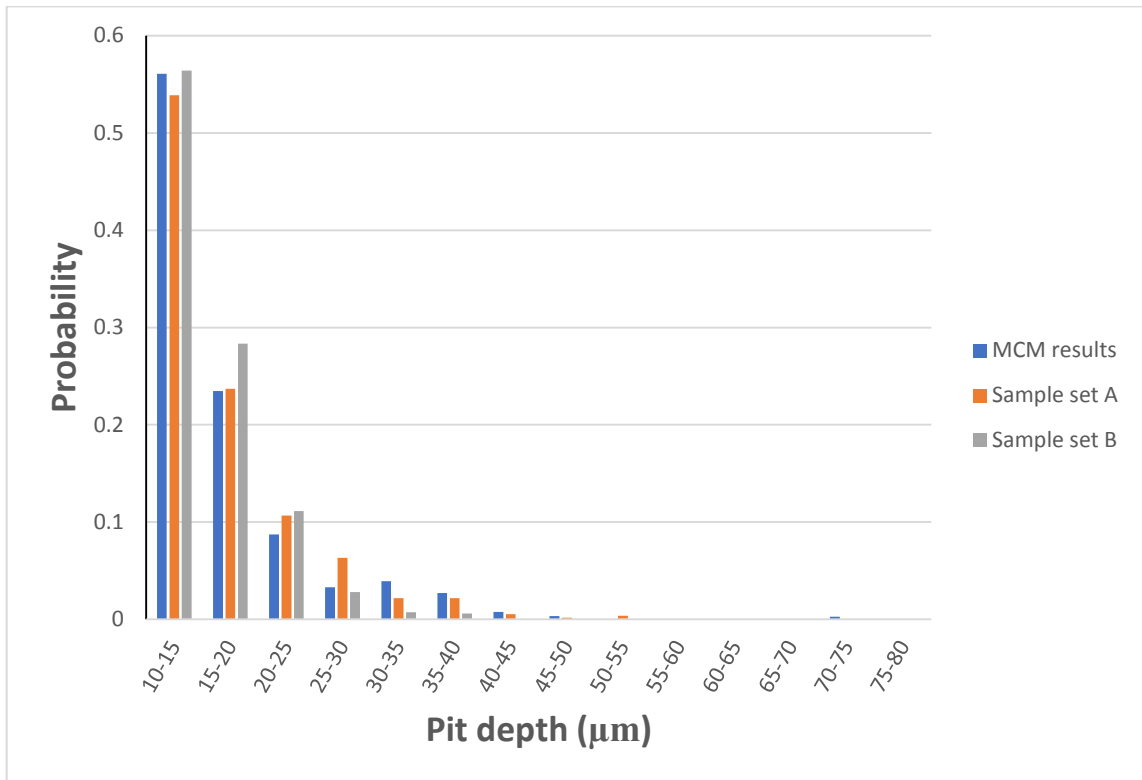


Figure 4.6: Two sets of samples [3] compared with the Monte Carlo method (MCM) results

In order to validate the computational model, it has been tested with experimental data from four total samples taken from the ROUTE J circuit. For this circuit, experimental data is available for tape samples taken with a service age of 50 years. Figure 4.7 shows the pit depth distributions of samples taken from ROUTE J circuit, as compared to the Monte Carlo results. It illustrates that these two pit depth distributions have a similar downward trend when the pit depth increases, although the pit depth distributions from the experimental and computational data show a slight difference, when the pits are large than 30 µm. Because the pit depth distributions of experimental and computational data have a similar trend and there is a relatively low difference in the

distributions, it can be said that the computational model is suitable for predicting the pit depth of the reinforcing tapes.

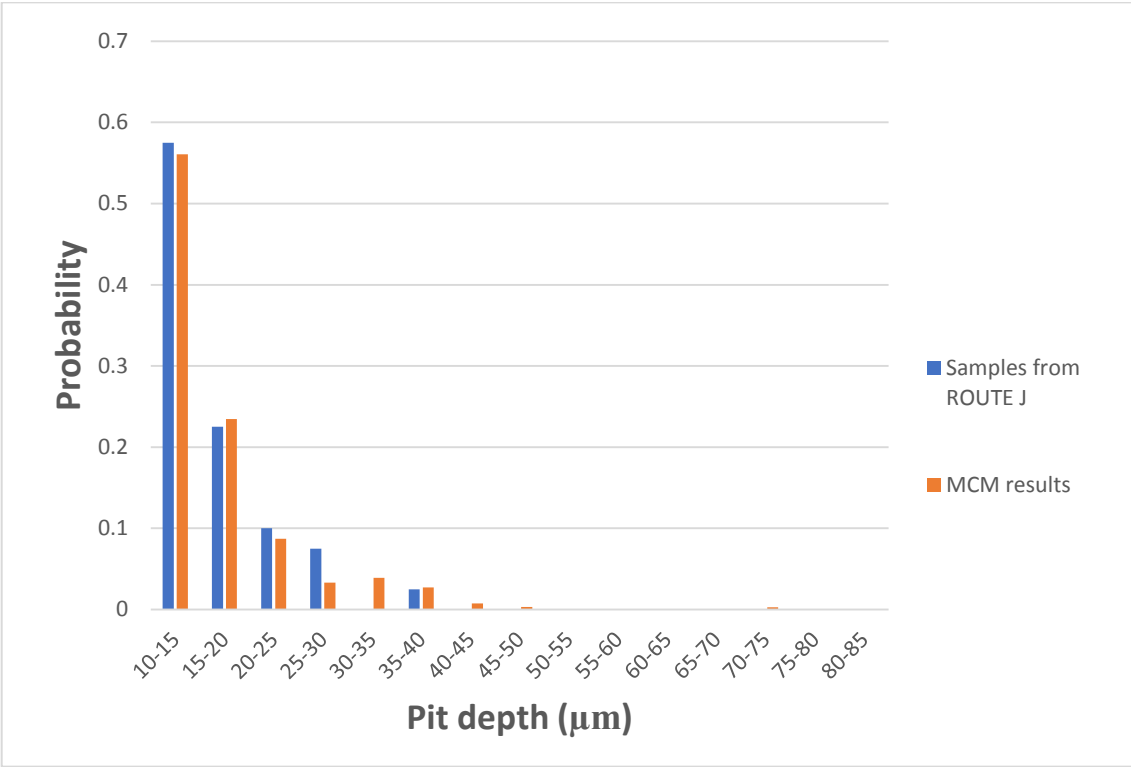


Figure 4.7: A comparison between pit depth distribution samples from the ROUTE J circuit [3] and the Monte Carlo simulation

To further validate the computational model, it has been tested with two sets of samples from the same circuit to capture the pit depth evolution over two time intervals. For these samples from the same circuit, experimental data is available for tape samples taken at two service lives, such as 38 years (16 samples) and 44 years (10 samples). These data provide an opportunity to validate the model of predicting the pit depth, and to find the evolution of the pit depth distribution over time. Figures 4.8 and 4.9 show the comparison between the pit depth distributions of a reinforcing tape with service ages of 38 and 44 years, respectively, and their corresponding simulations. In these figures, the number of pit depths is counted within every 5 µm depth interval. All

the parameters are critical values in the model and the parameter repassivation constant, γ , is varied to match the experimental data, while variation in the location is captured in the parameter γ . The best fit between the data occurred with a repassivation constant value γ equal to 0.166; this will be discussed in the following section. The simulation results are consistent with the experiment pit depth distributions at two different service lives, so it can be concluded that the computation model is capable of predicting the pit depth distribution of the reinforcing tapes.

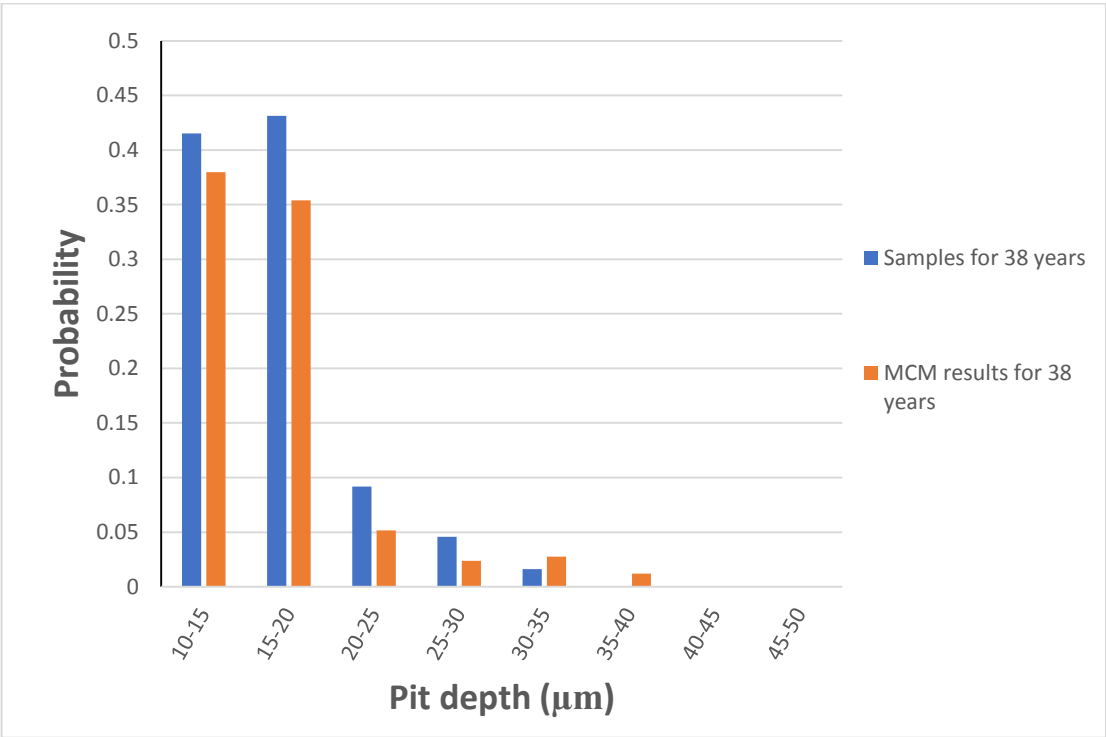


Figure 4.8: Comparison between the experiment [3] and MCM pit depth distribution of reinforcing tape of 38 years of age

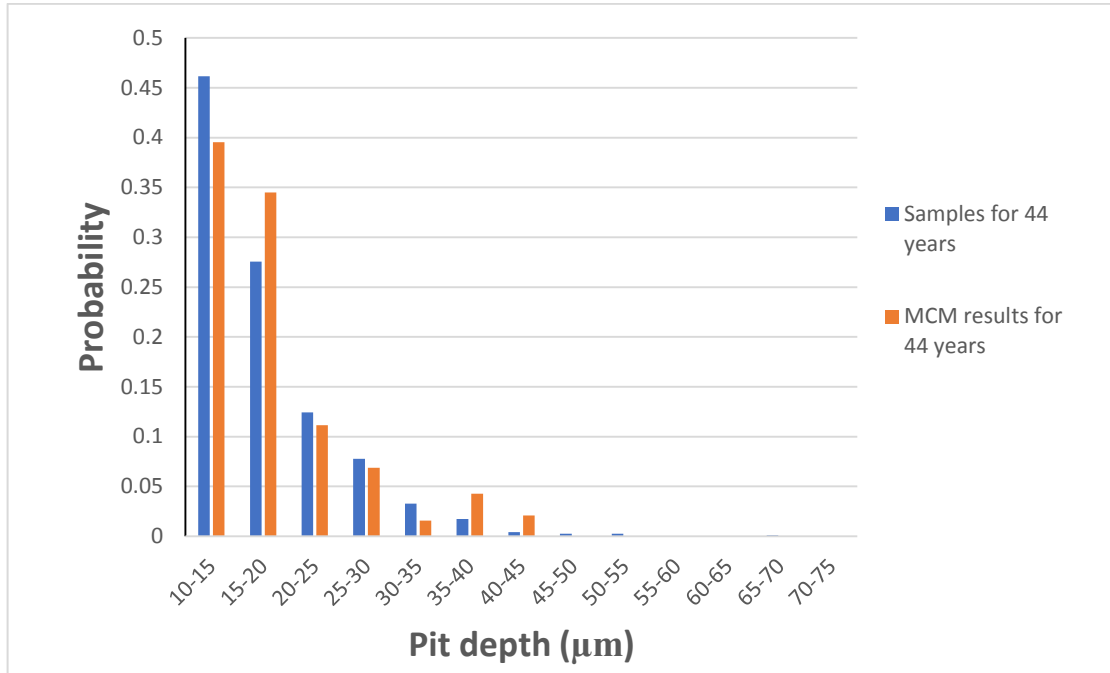


Figure 4.9: Comparison between the experiment [3] and MCM pit depth distribution for reinforcing tape of 44 years of age

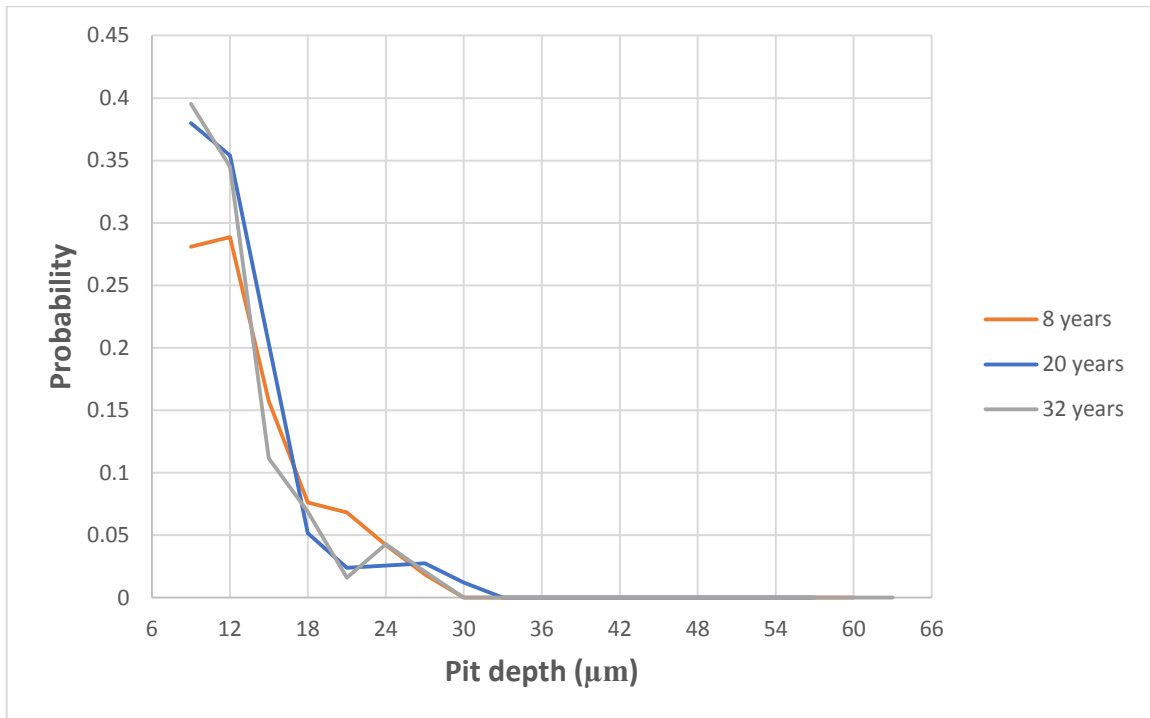


Figure 4.10: Monte Carlo model pit depth distributions for different simulation years (8 years, 20 years, and 32 years)

Figure 4.10 shows the pit depth distributions for different years by applying Monte Carlo model, and the pits are only counted when they have a depth larger than 9 μm . The repassivation constant value γ was chosen as 0.166. This repassivation constant value has been validated by Figure 4.8 and Figure 4.9. In Figure 4.10, it can be clearly observed that the distribution of small pit depth of 8 years is relatively lower than the distributions of 20 years and 32 years. Such difference because of various simulation time. For the short period of simulation time, most pits only penetrate to the small depth which less than 6 μm . In such case, these small pits ($< 6 \mu\text{m}$) will not be counted to show the distribution. Therefore, the distribution of pit depth between 9 μm to 12 μm is lower than the long period of simulation time which is observed in Figure 4.10. It also can be observed that there is a trend of pit growth, such as the appearance of a relatively high probability for the smaller pits, but this probability decreases sharply with an increased depth of pit, which is consistent with three different simulation time (8 years, 20 years, and 32 years). In Figure 4.10, it can be observed that there is little difference between the pit depth distributions of 20 years and 32 years. With such results, it can be point out that most of the pits have repassivated within 20 years and only a few pits are still alive and able to continue growing. As the pits can only penetrate 30% of the tape thickness, the reinforcing tape will not suffer significant failure without applying internal pressure/stress. Therefore, FEM will be used to analyse the failure situation with the combination of pitting corrosion and applied internal pressure in Chapter 5.

4.4 Parametric study of the Monte Carlo model

When modelling the pit depth of reinforcing tin-bronze tapes, several parameters are not decided by the materials because when they are changed, they may affect the accuracy of the simulation results. One of the important factors for pit initiation is the dissolution time, which as mentioned in Section 4.1, is an uncertain parameter. Therefore, three values of the dissolution time are chosen in the simulation model to check which time is the best for the Monte Carlo model. The dissolution time varies

from three to 300 days to study the impact of this factor on the pit depth, and Figure 4.11 shows how the distribution of the pit depth changes with different values. To obtain this figure, pit depths larger than 74 μm are ignored because few pits are distributed in the range from 74 μm to 117 μm , as shown above, and those neglected values would not affect the results of the dissolution time. When the dissolution time is changed from three days to 300 days, however, it can be observed that there is some difference between the distributions from 9 μm to 19 μm . When the pit depth is over 24 μm , there is little difference between these three dissolution times; by looking at the dissolution times of three days and 100 days, the two curves are fairly similar from the start point until the end. Based on this result, a dissolution time of between three and 100 days could be chosen as the initial value. In the computational model, 100 days is chosen as the standard dissolution time for the simulation.

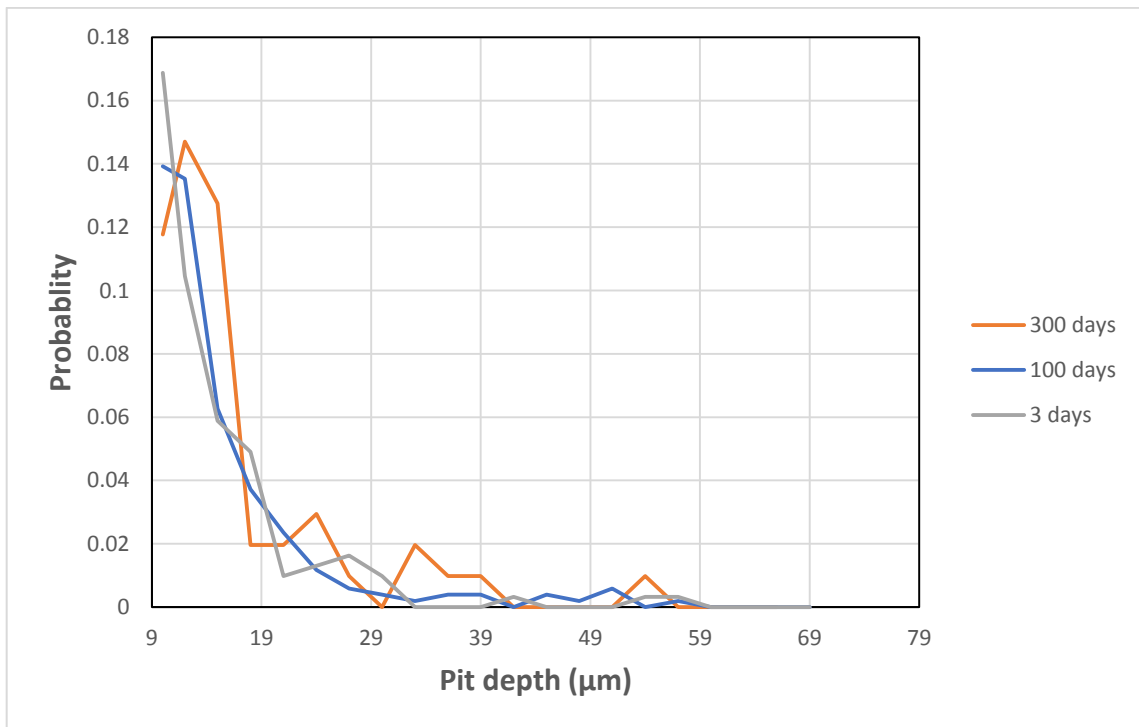


Figure 4.11: Pit depth distribution with different dissolution times (three, 100, and 300 days)

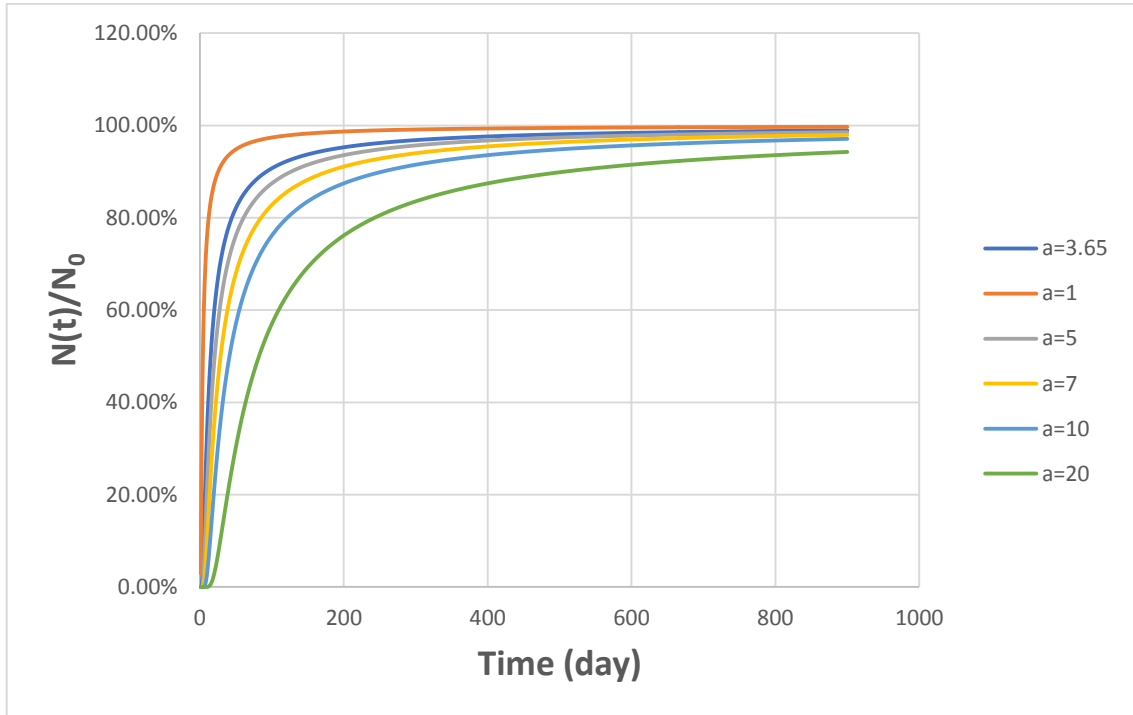


Figure 4.12: Number of stable pits ($N(t)$) increasing with time under different value of a ($a=1, 3.65, 5, 7, 10, 20$)

Another important factor for pit initiation is ' a ' which is used for PDM. Figure 4.12 shows the number of stable pits growing with time for different value of ' a '. It clearly illustrates that the smaller the value of ' a ', the less time all the pits are needed to become stable pits. As mentioned above, after the dissolution time, all the pits would become stable around one year. Therefore, the value of ' a ' can be defined in the domain between 1 and 5 which is based on the Figure 4.12. In this Monte Carlo model, 3.65 is chosen for the value of ' a ' to simulate the pit initiation stage.

The temperature could be another factor influences the growth of pits. In the computational model, other parameters were kept constant and the temperature varied from 273.15 K to 308.15 K, based on the literature detailing data and studies on the effect of temperature on pit growth. The computational model does not consider the nucleation stage and repassivation stages in order to explicitly show the difference

in temperature. This means that the pit can continue growing without any hindrance. Figure 4.13 shows the effect of temperature on pit growth and can be observed that there is less variation in pit growth between the highest and lowest temperatures after 600 days. This illustrates that temperatures in the range of 273.15-308.15 K do not alter the rate of pit growth, and 295.15 K can be chosen as an optimal parameter for the model.

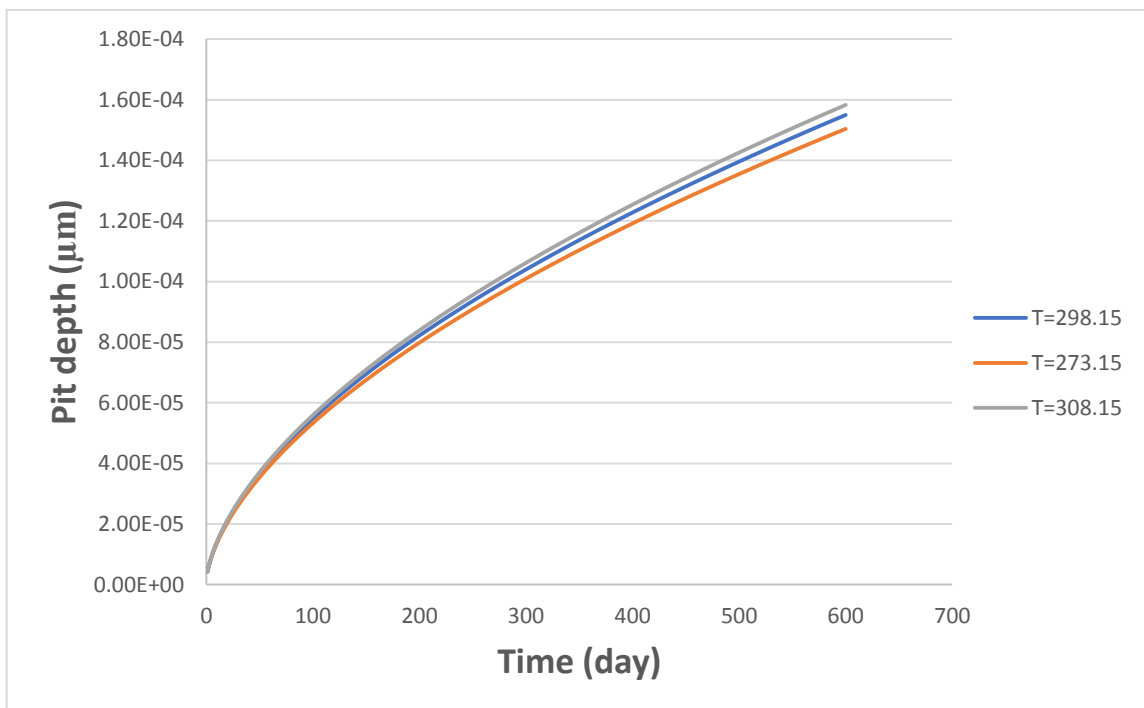


Figure 4.13: A comparison of pit depth between three temperatures

The parameter of the repassivation constant, γ , is used to determine whether or not the pit will stop growing. As Engelhardt and Macdonald [32] pointed out, this repassivation constant is equal to 0.066 for aluminium alloys. In order to find the effect of repassivation on pit growth, the computational model varies the value of γ to 0.066 and 0.266 by keeping other parameters constant. Figure 4.14 shows the difference between the experiment data and the simulation results; RC stands for the repassivation constant. In this figure, the samples are taken from the ROUTE F circuit. The idea of choosing these samples is because the computational model fits these

experimental data perfectly. When $RC = 0.066$, the pits are much easier to grow than to stop, and it can be observed clearly that the simulation curve shows there are plenty of pits that can reach over a depth of $30\ \mu\text{m}$. However, when $RC = 0.266$, it can be observed from the simulation curve that the pits are comparatively difficult to grow for a long duration, and the maximum pit depth is just $20\ \mu\text{m}$. Figure 4.14 shows that both the repassivation constant values, 0.066 and 0.266 , are not suitable for the ROUTE F circuit. From Figure 4.6, it can be seen that the best fit value of RC is 0.166 . Similarly, as shown in Figure 4.8 & 4.9, the best fit value of RC should be 0.166 for the ROUTE A circuit as well. The parameter γ plays an important role in pit growth, and it also changes according to environmental conditions. The best fit for this Monte Carlo model is to choose 0.166 as the repassivation constant. To predict the pit depths of reinforcing tapes in different circuits, various values should be chosen for the repassivation constant.

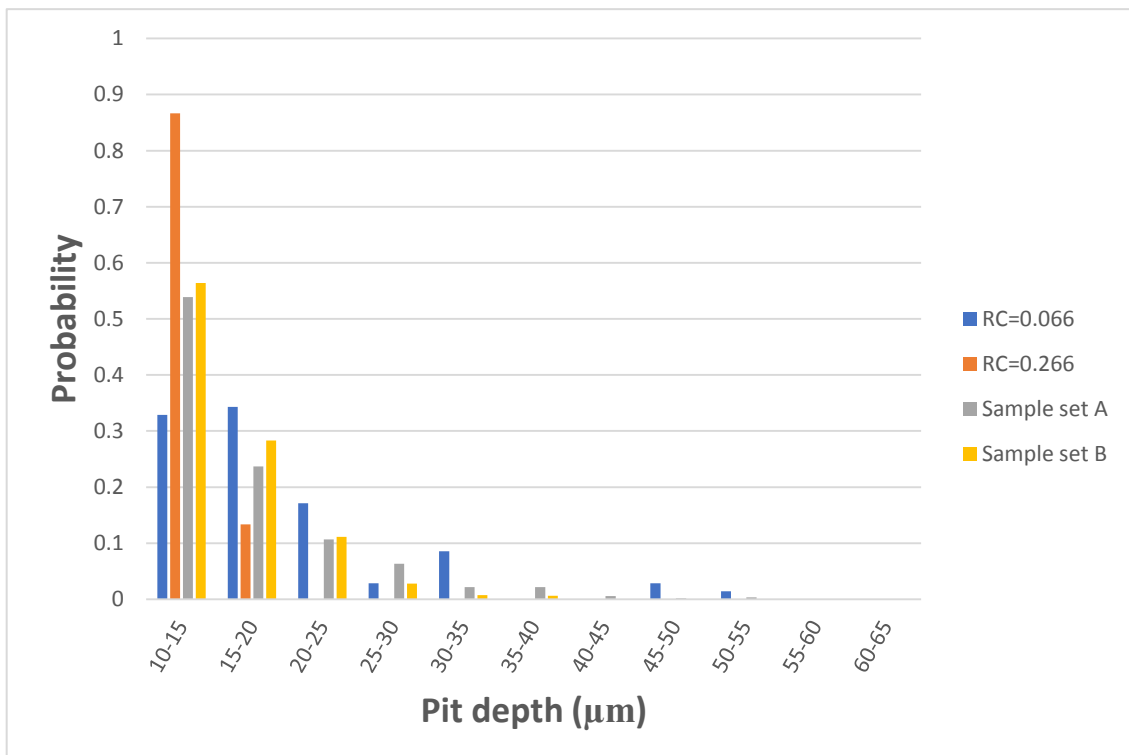


Figure 4.14: A comparison between the experimental [3] and computational pit depth distributions with different γ values

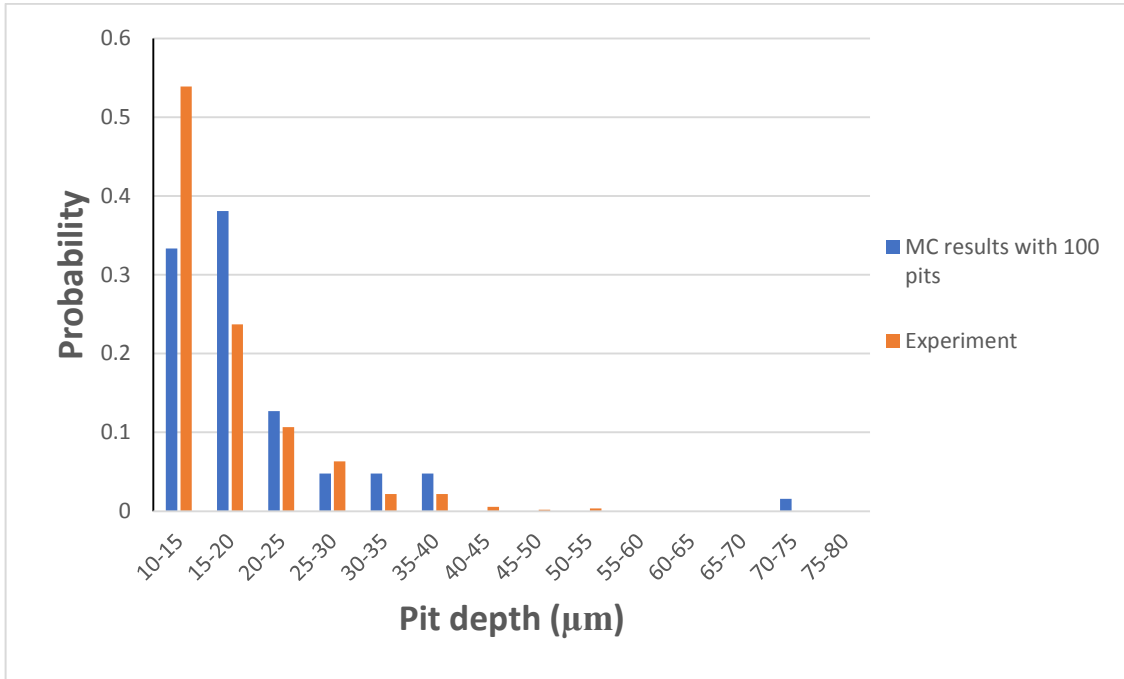


Figure 4.15: A comparison between experiment data (Courtesy of Mechanical of Material group) and Monte Carlo simulation results with 100 pits

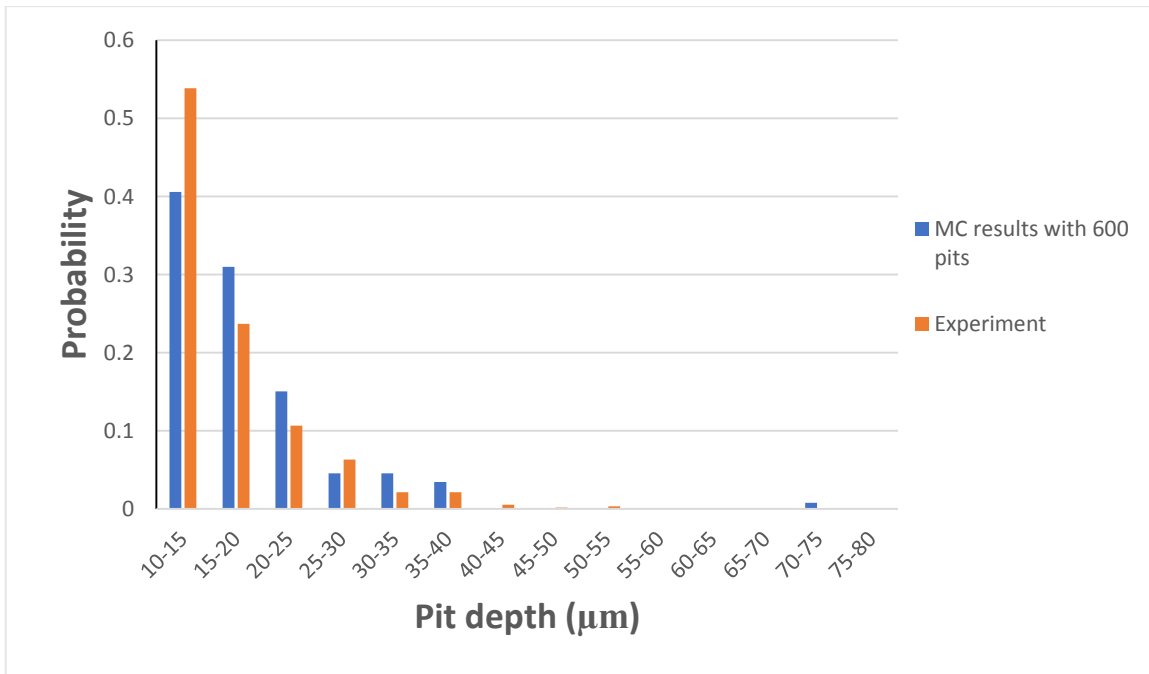


Figure 4.16: A comparison between experimental results (Courtesy of Mechanical of Material group) and Monte Carlo simulation results with total 600 pits

Figure 4.15 and Figure 4.16 show the distributions between experiment data and Monte Carlo simulation results which based on a random number of the repassivation part. It can clearly see from Figure 4.15 that Monte Carlo simulation results do not completely fit with the experiment data. Just in the domain of 20-35 μm , the probabilities of experiment data and simulation results are almost identical. For other domains, although the probabilities are not the same, the distributions are specifically similar in most instances. Figure 4.15 illustrates that for experiment data and MCM results, the pitting depth most concentrate in the domain of 10-45 μm . Beyond this domain, only a few pits could reach to the extremely deep values. However, this result is gotten from Monte Carlo method as running only once which cannot explain if the simulation results approximately fit with experiment data. In such situation, the Monte Carlo simulation ran for 6 times to get the average results. Then the average results were compared with experiment data to see if these two kinds of data can fit well. Figure 4.16 illustrates that the average value of Monte Carlo simulation still mainly concentrates in the domain of 10-45 μm . However, there are also several pits could reach to the depth over 70 μm . For the experiment data, all the pitting depths are less than 55 μm . As the Monte Carlo simulation is depended on the random parameter of delayed repassivation constant, all the pitting depths are not predictable. According to the Figure 4.16, the results of Monte Carlo simulation model still can fit the experiment data ideally even they are unpredictable. In other words, the Monte Carlo method could be used to simulate the pits propagation and pit repassivation which even has few differences against the experiment data.

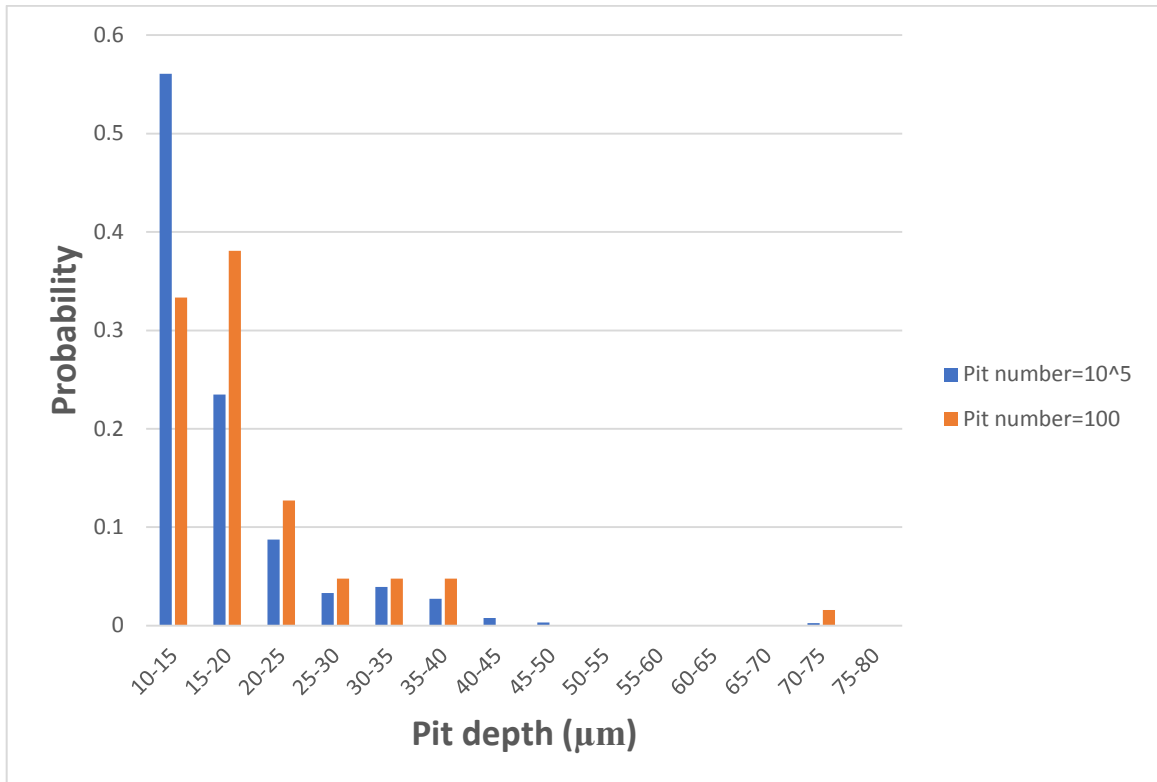


Figure 4.17: A comparison between two different set of total number of pits

Figure 4.17 shows two set of distributions by using 100 and 10^5 pits to simulate the pit depth. From Figure 4.15 and Figure 4.16, they show that the Monte Carlo model can fit the experiment data by only using total 600 pits. However, the idea of Monte Carlo model is to input large amount of data to make the results more accurate and reliable. Therefore, 10^5 pits are used to simulate the pitting corrosion process, and then make a comparison with 100 pits to identify the difference of pit depth distribution. It can be observed from Figure 4.17 that there is a trend of pit growth, such as the appearance of a relatively high probability for the smaller pits, but this probability decreases sharply with an increased depth of pit, which is consistent with both total 100 and 10^5 pits of pit depth distributions. But there has a relatively large difference between these two set of pits. Such difference because of the amount of input number of pits. When the input data is huge enough, the results of average value is more acceptable. Hence, for simulating the pitting corrosion process, the result of 10^5 pits is more acceptable and accurate than the result of only 100 pits.

4.5 Summary

The computational model based on the Monte Carlo simulation can be used to predict the pit depth of reinforcing tin-bronze tapes of underground power cables. In this model, 10^5 pits have been used to simulate the pit depth, and each pit is tracked independently and randomly. The results are therefore based on a huge amount of data, and show the statistic distribution of pit depths for over 40 years. The curve of the pit depth-time shows that the computational model can fit the empirical model and, the results of the pit depth distribution therefore are in a reliable range.

In Section 4.3 and 4.4, the results were compared with the experimental data to verify the accuracy of the computational model. The pit depth distribution shows that most of the pits repassivate before they can reach the maximum depth during the entire growth time. When the pit depth is relatively small, repassivation occurs much more easily, while deeper pits tend to continue growing. As the pits can only penetrate 30% of the tape thickness, the reinforcing tape will not suffer significant failure without applying internal pressure/stress. Hence, finite element method will be used to make the judgment of failure situation with the combination of pitting corrosion and applied internal pressure. Based on the experimental data, the best dissolution time for the computational model is 100 days, which means that all the pits have nucleated within 100 days. Also, for the pit initiation, the PDM parameter ' α ' is chosen as 3.65, which means that all the nucleated pits become stable within one year. However, these values are determined by the experimental data, and they may change if different conditions or materials are used.

It has been shown that the Monte Carlo model for finding the corrosion pit depth can be successfully used to simulate pit nucleation, propagation, and repassivation. By using this model, the distribution of pit depth of reinforcing tin-bronze tapes can be simulated

with consistent experimental results. The dissolution time and environment temperature do not affect the pit depth significantly, while the standard value of dissolution time is 100 days and the temperature 298.15 K. The parameter ' a ' which is used in pit nucleation stage could be affect the time that all the pits transfer to stable pits. Basically, for this Monte Carlo model, all the pits become stable within one year. Hence, the range of the value ' a ' can vary from 1 to 5 and 3.65 is chosen for this model which is same in Engelhardt and Macdonald's model [28]. The important parameter that needs to be considered is the delayed repassivation constant. As discussed from the results, this repassivation constant might be changed for different circuits because circuits are buried in different locations with varying environments. However, the value of the repassivation constant will not change sharply, according to the experimental and computational models; the range of the value can vary only from 0.066 to 0.266. Because the computational model is validated by different sets of experimental data, the model can predict the pit depth and find the evolution of pit depth distribution over time for the reinforcing tin-bronze tapes. In this way, the model can be extended to find the useful remaining life of the cables.

Chapter 5. Stress analysis around representative pits in failed cables

In this chapter, the failure mechanisms of cables are considered as pitting corrosion with oil internal pressure. For the reinforcing tapes penetrated by pitting corrosion, the asset life of the cables is determined by the critical pit depth and probability of failure. When stress is applied to the tapes, a COMSOL model is used to analyse the failure condition of tape based on pit depth and applied stress. It shows that less average applied stress is needed to satisfy the failure condition when the pits grow deeper. Hence, with the pits occur on the reinforcing tin-bronze tapes, the higher working stress can lead to the tapes much easier to fail. For the reinforcing tin-bronze tapes with a critical pit depth, a COMSOL model is used to simulate the area of plastic deformation zones with various applied stresses. By comparing reinforcing tape with different applied stress, it can be seen that a large area is found when the reinforcing tapes will fail, while a relatively small area occurs when the tapes have not reached the failure level.

5.1 Review of failure models

For the tin-bronze reinforced tapes that are used for oil-filled power cables, the internal oil pressure, thermal loading, and corrosion are the most important factors that influence the corrosion fatigue failure of the tapes. For these factors, the internal pressure of the cable is considered to play the most vital role during the reinforcing tape failure process. This process consists of six stages, as presented in Figure 5.1. In the third and fourth stages, the pit grows and transforms into a crack due to fatigue load. In case of cable failure, the fatigue load is assumed to be internal oil pressure. The corrosion fatigue model is described as follows [3].

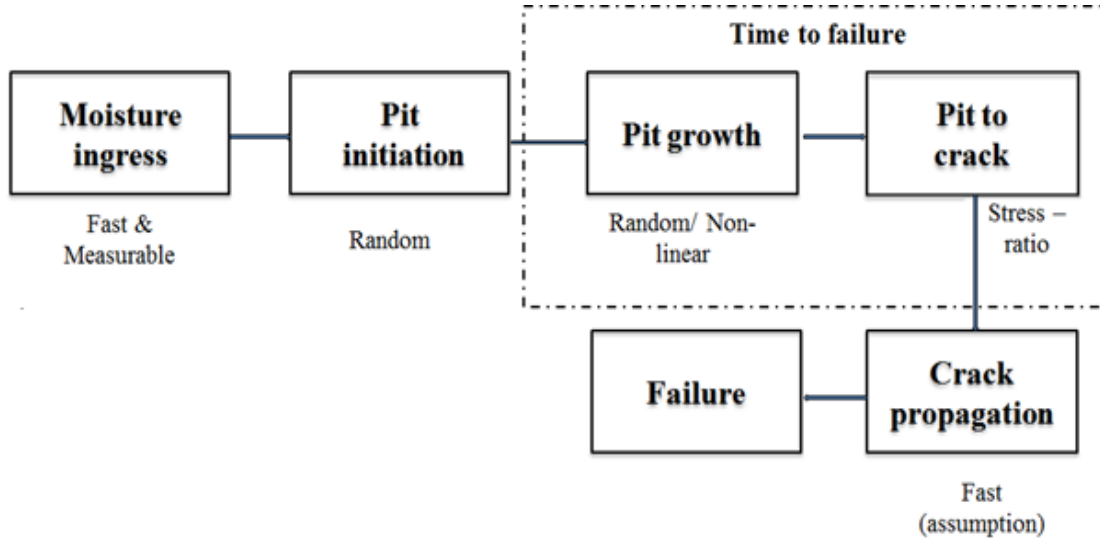


Figure 5.1: Stages of the corrosion fatigue failure process of reinforcing tape corrosion, and the key events contributing to the life of the cable [3]

The pit growth rate is given by:

$$\frac{dx}{dt} = \frac{\beta x}{t} = \beta \alpha^{\frac{1}{\beta}} x^{(1-\frac{1}{\beta})} \quad (5.1)$$

For the constant values of α and β (<1), according to equation (5.1), the smaller pits grow quickly, while the deeper pits grow more slowly.

The crack growth rate is given by:

$$\frac{dx}{dt} = C \Delta \sigma^p x^q \quad (5.2)$$

where x is the crack length, C is a constant for the same type of crack, and $p = 2q$ and q are material constants. As Gnanasambandam et al. [110] pointed out, using the field data, observations show that the mean stress influences the failure, rather than the stress amplitude. In order to simulate the oil-filled power cable failure that can be observed in field data over a long period of time, it should be necessary to modify equation 5.2 similarly to the ripple loading, with mean stress and daily alternating stress $\Delta \sigma$, as shown below:

$$\frac{dx}{dt} = C(\sigma_{mean} + \Delta\sigma)^p x^q \quad (5.3)$$

The pit transforms into a crack of the same size when:

$$\left| \frac{dx}{dt} \right|_{Pit} = \left| \frac{dx}{dt} \right|_{Crack} \quad (5.4)$$

By equating equations (5.2) and (5.3), the above equation can be rewritten as:

$$\frac{x^\beta}{t} = C(\sigma_{mean} + \Delta\sigma)^p x^q \quad (5.5)$$

The critical depth at which the crack growth rate exceeds the pit growth rate is then given by:

$$x_{crit} = \left(\frac{\beta}{C(\sigma_{mean} + \Delta\sigma)^p t_f} \right)^{\frac{1}{q-1}} \quad (5.6)$$

where t_f is the time to failure of the cable. The critical pit depth is described as a function of the applied mean stress, the alternating stress, and the environmentally exposed conditions. Unique curves can be plotted for the pit and crack growth rate as a function of pit size, which will depend upon the values of α and C , respectively, as shown in Figure 5.2.

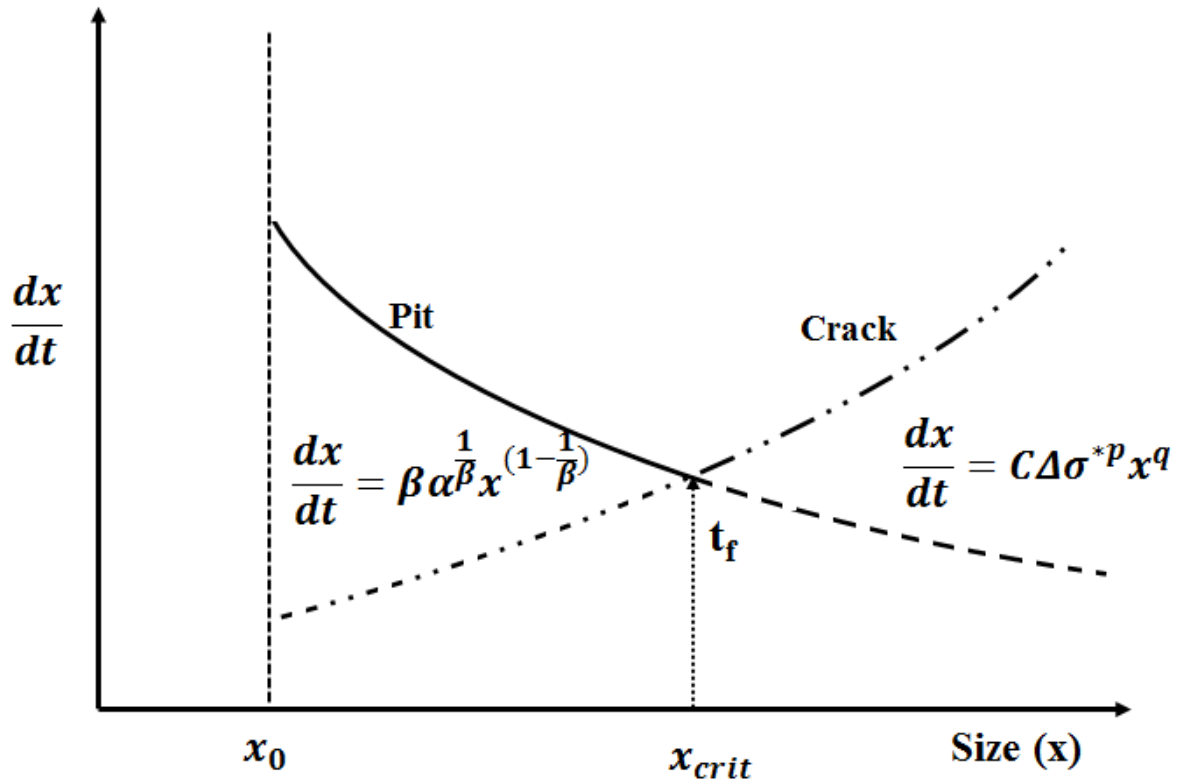


Figure 5.2: An illustration of the pit-to-crack transition for a single pit that has specific values of the growth rate parameters α and C , while the time to reach x_{crit} is the time of failure (t_f) for the cable [3]

From equation (5.6), it can be assumed that at time $t = 0$, the initial pitting depth is x_0 . At time $t = t_f$, the critical size is reached at which the pit transforms into a crack. To estimate the cable failure time (t_f), three phases need to be followed: using Monte Carlo simulations to derive the pit growth parameter from the failed tape pitting depth distribution and find the critical pitting depth; obtaining the crack growth parameters from the failure conditions that are already known; and calculating the probabilistic failure life.

For the first phase of the method, the decisive step in pit growth modelling is finding the critical pit depth for failure. As Gnanasambandam et al. [3] have pointed out, the

critical pit depth is determined by the value of p_{crit} , which is defined as a critical probability of failure above which the cable is considered unsafe. The value of p_{crit} is chosen to be a very small number, and is guided by the real failure data. The critical pit depth (x_{crit}) can be calculated either by numerical or analytical methods. Numerically, x_{crit} is calculated in such a way that the area under the pit depth probability distribution curve above x_{crit} to infinity is equal to p_{crit} . Using the analytical solution, it is also possible to calculate x_{crit} by integrating the three-parameter GEV probability density function (PDF) for the parameter α from x_{crit} to infinity. Then, x_{crit} can be calculated as:

$$x_{crit} = \left(\sqrt{\frac{-1}{\ln(1-p_{crit})}} - 1 + \mu \right) * t^{0.33} \quad (5.7)$$

The second phase is calculating the crack growth parameters C , p , and q . These parameters are calculated by equating the pit growth rate to the crack growth rate for known cases of failure and their corresponding mean, and alternating stress conditions using equation (5.5). The accuracy of the crack growth parameters (C and p) depends on two major parameters: x_{crit} and measured stresses. Since the choice of p_{crit} determines the critical pit depth, the effect of x_{crit} on the derived parameters is tested by varying the value of $p_{crit} \pm 20\%$ and calculating the corresponding x_{crit} .

The final phase is to calculate the time to failure (t_f) for the cable using all parameters (α , β , C , p , and q) derived from the known cases of failure. For a given time, the possible critical pit depth is calculated from equation (5.6). Then, p_{crit} is calculated from equation (5.7) as:

$$p_{crit} = 1 - \exp\left(\frac{-1}{\left(\frac{x_{crit}}{t^{0.33}} - \mu + 1\right)^2}\right) \quad (5.8)$$

When the calculated $p_{crit} = 0.001$, the corresponding time is the t_f of the cable.

5.2 Alternative failure criteria based on pitting corrosion

Based on the previous sections, if it is assumed that there is no interaction between the pits (through the electric potential) then there is an analytical solution to the probability density function for the growing-repassivating pits, the pit depth growth with time can be described as:

$$x(t) = \alpha t^n \quad (5.9)$$

where $x(t)$ is the depth of a pit at time t , and time is taken from the onset of nucleation. Alternatively, given the pit depth of a growing pit, the time taken is:

$$t = \left(\frac{x}{\alpha}\right)^{\frac{1}{n}} \quad (5.10)$$

Hence, the rate of pit depth growth is:

$$\frac{dx}{dt} = \alpha n t^{n-1} \quad (5.11)$$

Based on the model in Chapter 4, the fraction of pits repassivated per day is taken to be γ . The fraction that keeps growing is therefore $(1 - \gamma)$. The fraction of pits that are still growing at a time t after they have nucleated is:

$$P_{grow} = (1 - \gamma)^t \quad (5.12)$$

The rate of change of growing pits then can be found by taking logs:

$$\ln(P_{grow}) = \ln(1 - \gamma)t \quad (5.13)$$

And differentiating with respect to time:

$$\frac{1}{P_{grow}} \frac{dP_{grow}}{dt} = \ln(1 - \gamma) \quad (5.14)$$

Therefore, the rate of growing pits is:

$$\frac{dP_{grow}}{dt} = \ln(1 - \gamma) \cdot (1 - \gamma)^t \quad (5.15)$$

Based on above content, the probability density function (PDF) for pit depth can be defined as:

$\phi(x)dx = \text{fraction of non - growing pits with pit depth between } x \text{ and } x + dx$

Or, given the mapping between t and x above:

$\phi(x)dx = \text{fraction of pits that stop growing between times } t \text{ and } t + dt \text{ after nucleation}$

Hence,

$$\phi(x)dx = P_{grow}(t) - P_{grow}(t + dt) = -\frac{dP_{grow}}{dt} dt \quad (5.16)$$

Then the equation can be rewritten as:

$$\phi(x) = -\frac{dP_{grow}}{dt} / \left(\frac{dx}{dt}\right) \quad (5.17)$$

Then equation (5.17) can be combined with equations (5.11) and (5.15) as:

$$\phi(t) = -\frac{\ln(1-\gamma)}{\alpha n} \cdot (1 - \gamma)^t \cdot t^{1-n} \quad (5.18)$$

Combined equation (5.18) with (5.10) and the PDF of pit depth can be written as:

$$\phi(x) = -\frac{\ln(1-\gamma)}{\alpha n} \cdot (1 - \gamma)^{\left(\frac{x}{\alpha}\right)^{\frac{1}{n}}} \cdot \left(\frac{x}{\alpha}\right)^{\frac{1-n}{n}} \quad (5.19)$$

Based on such a simple ‘non-interaction’ model, the pit depth distribution can be modelled by using parameters (α , n & γ) from Chapter 4. The values $\alpha = 3.7611$ and $n = 0.583$ are calculated from Figure 4.2, and the value $\gamma = 0.166$ is determined by the Monte Carlo model. Then the equation (5.19) can be plotted in Figure 5.3. From this figure, it clearly illustrates that most pits have the depth between 0 to 30 μm . After 30 μm , the pits have significantly low probability to reach such depth. Moreover, from this figure, it is shown that more than half of the total number of pits only have the depth focus in the domain of 0-10 μm . As discussed in Chapter 4, the repassivation delay constant γ have vary values (0.066, 0.166, and 0.266) to be used for different conditions. Figure 5.4 shows the difference of distributions between these three values. It clearly

shows that with relatively high value of γ , the maximum pit depth is relatively small. When the repassivation delay constant becomes small, the pit could reach to larger size which is approximately equal to 50 μm .

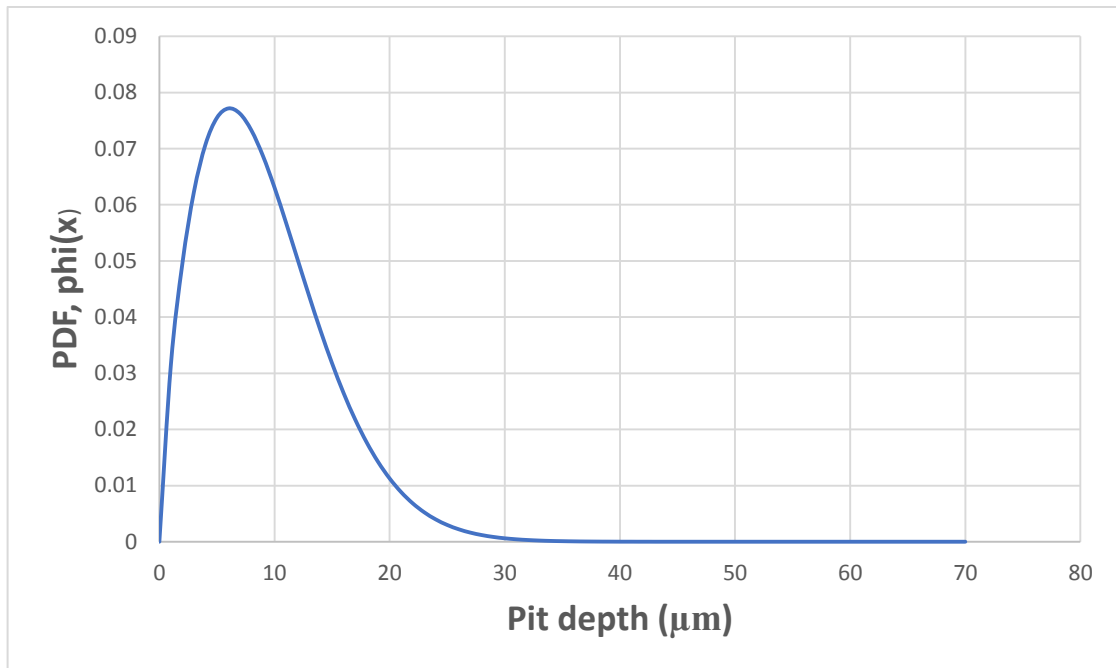


Figure 5.3: PDF of pit depth distribution with three parameters (α , n & γ)

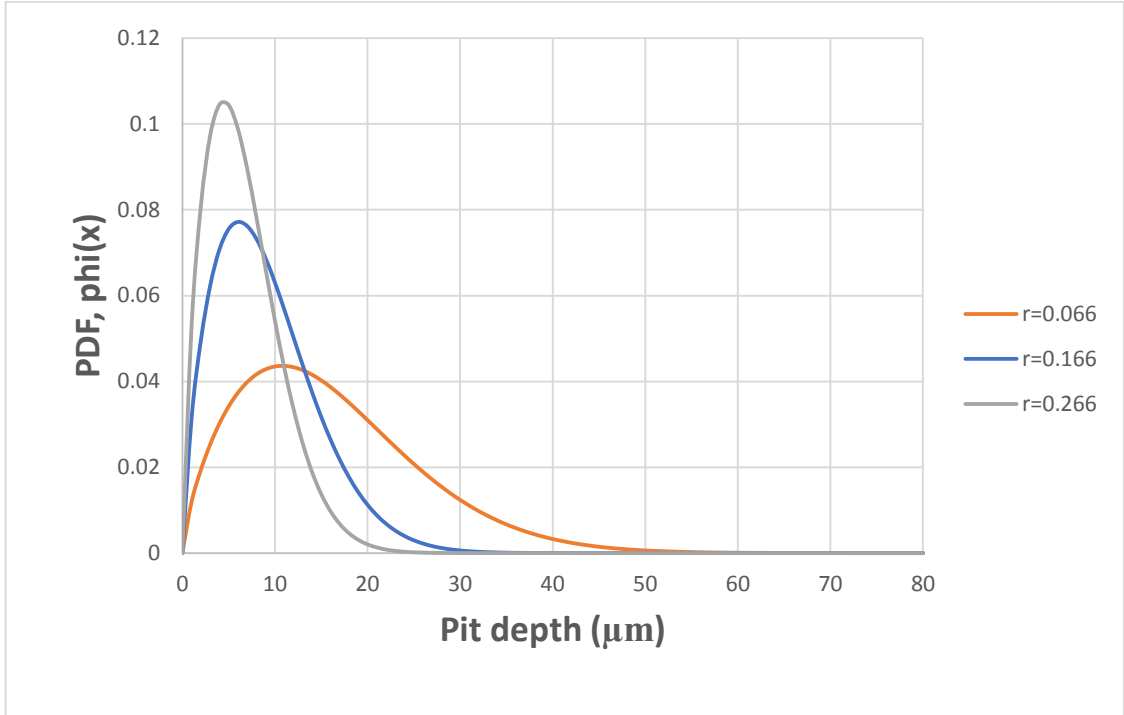


Figure 5.4: PDF of pit depth distribution with different value of γ (0.066, 0.166, and 0.266)

According to Gnanasambandam's model [3], for the GEV, the critical size of pits x_c is defined as those with a probability of p_c of existing. Hence,

$$1 - p_c = \int_0^{x_c} \phi(x) dx \quad (5.20)$$

And

$$\int_0^{x_c} \phi(x) dx = - \int_0^{t_c} \frac{dP_{grow}}{dt} dt = - \int_1^{p_c} dP_{grow} = 1 - p_c \quad (5.21)$$

is required.

Therefore, combined with equation (5.15), equation (5.21) can be rewritten as:

$$1 - p_c = - \int_0^{t_c} \frac{dP_{grow}}{dt} dt = - \int_0^{t_c} \ln(1 - \gamma) \cdot (1 - \gamma)^t dt = 1 - (1 - \gamma)^{t_c} \quad (5.22)$$

Hence,

$$p_c = (1 - \gamma)^{t_c} \quad (5.23)$$

Then,

$$t_c = \frac{\ln(p_c)}{\ln(1-\gamma)} \quad (5.24)$$

And critical pit depth can be calculated by using equations (5.9) and (5.24),

$$x_c = \alpha \left(\frac{\ln(p_c)}{\ln(1-\gamma)} \right)^n \quad (5.25)$$

By using Poisson distribution, the number of critical pits will be $p_c N_0$, where N_0 is the number of total pits. And the probability of no critical pits can be written as:

$$P(n = 0) = e^{-p_c N_0} \quad (5.26)$$

As Gnanasambandam et al pointed out [3], the reinforce tape will fail when there are one or more pits reach to the critical depth. Therefore, the probability of failure is given by the Poisson statistic as:

$$P_{fail} = 1 - \exp(-p_c N_0) \quad (5.27)$$

By using equation (5.25), equation (5.27) can be rearranged as:

$$P_{fail} = 1 - \exp\left(-N_0(1 - \gamma)^{\left(\frac{x_c}{\alpha}\right)^{\frac{1}{n}}}\right) \quad (5.28)$$

The probability of failure with critical pit depth then can be plotted in Figure 5.5, and the parameters (N_0 , α , n , and γ) are given from Chapter 4 based on Monte Carlo model. Figure 5.5 clearly shows how critical pit depth affect the failure probability of tape. It clearly demonstrates that probability of failure is reduced with increased of critical pit depth. These curves illustrate that when the critical pit depth reach to a larger value, the probability of no critical pit depth becomes bigger. Hence, more pits indicate that do not have the same depth as critical pit depth. As the result, when critical pit depth tends to a larger value, the tape has a lower chance to fail. However, such probability has different distributions with vary repassivation delay constant γ (0.066, 0.166, and

0.266). It can be seen clearly from Figure 5.5 that with relatively high value of γ ($=0.266$) the maximum critical pit depth which lead to the failure of tapes can only reach to a small value. Moreover, Figure 5.5 shows that when the critical pit depth only has a small value, all the pits are easily to reach to that depth and the reinforce tape has a significantly high probability to fail when the pits occur.

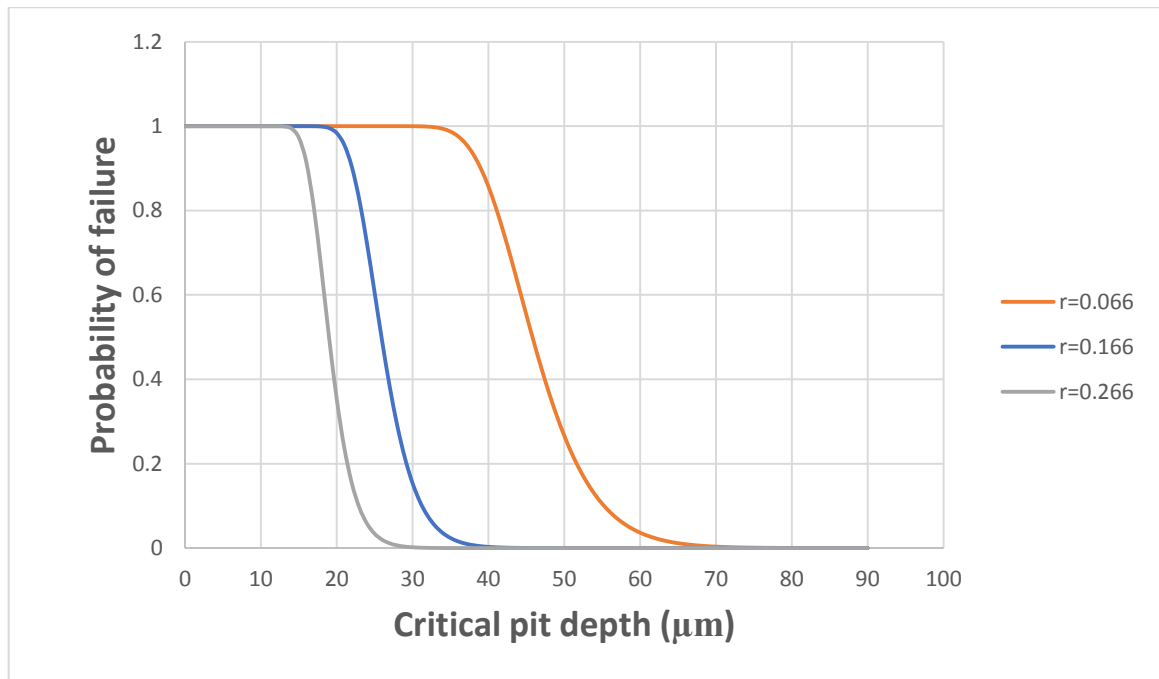


Figure 5.5: Failure probability of critical pit depth with different repassivation delay constant γ (0.066, 0.166, and 0.266)

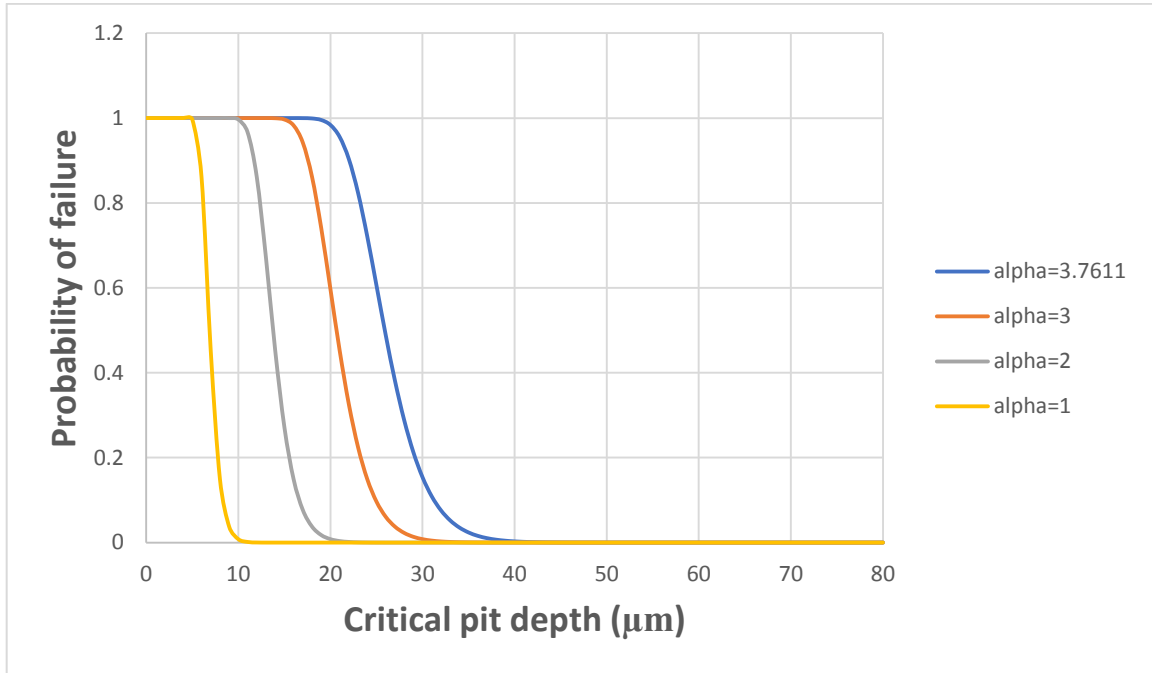


Figure 5.6: Failure probability of critical pit depth with different α (1, 2, 3, and 3.7611) which is used in pit growth model

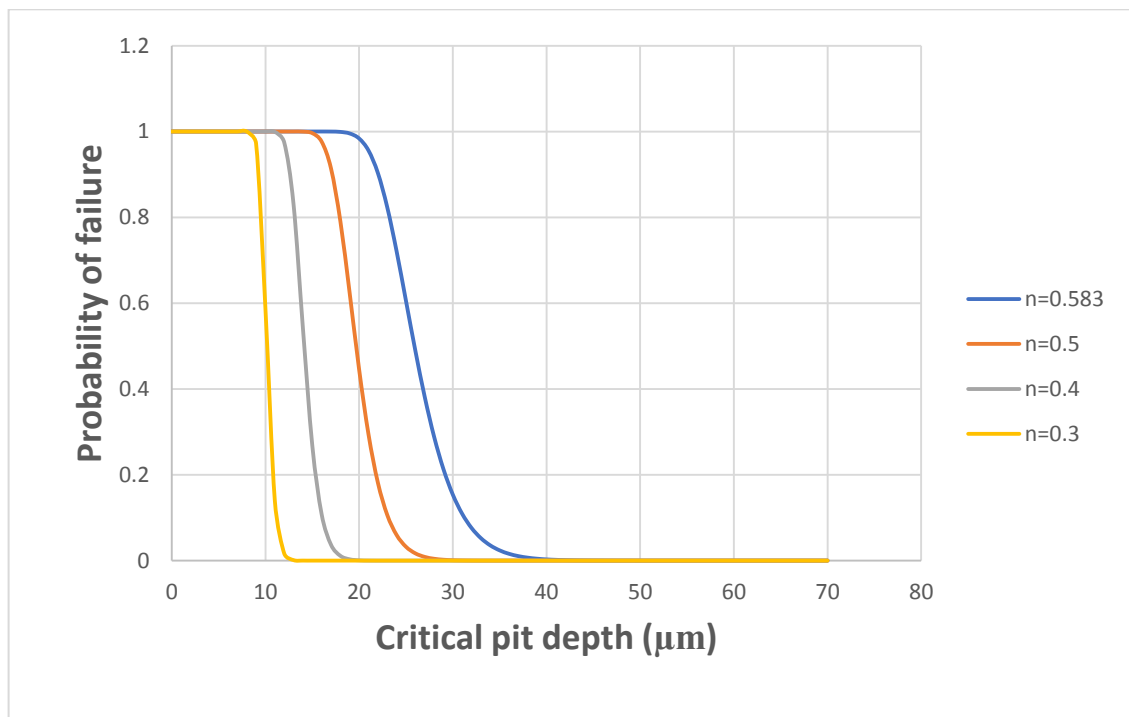


Figure 5.7: Failure probability of critical pit depth with different n (0.3, 0.4, 0.5, and 0.583) which is used in pit growth model

Figure 5.6 and Figure 5.7 show that distributions of probability of failure are affected by different values of γ and n which are used for simulating pit growth model. Figure 5.6 indicates that when α is reduced from 3.7611 to 1, the maximum critical pit depth that leading to the failure of tape decrease. Figure 5.7 also shows the similar results. As reducing the value of n from 0.583 to 0.3, the maximum critical pit depth decline. These two figures both illustrate that when the pit growth rate is reduced, the reinforcing tape is much easier to fail with relatively small critical pit depth. In other words, when pitting corrosion occurs on the tape, the pits with small depth also can be treated as reaching to the critical value and then the tape will fail.

5.3 FEM model for reinforcing tape with a critical pit depth

In section 5.2, it was illustrated that for reinforcing tape with a pit reach to a critical depth, the tape tends to be failed. Equation (5.25) shows that the critical pit depth depends on the value of $\alpha, n, \gamma,$ and p_c . As discussed in Chapter 4 and based on Gnanasambandam's model [3], $\alpha(= 3.7611)$ and $n(= 0.583)$ were simulated from the pit growth model, $\gamma(= 0.166)$ was given from pit repassivation model, and $p_c(= 0.001)$ was obtained by Gnanasambandam et al. With these values of parameters, the critical pit depth can be calculated as 31.38 μm . Based on such value, pit can reach to the critical depth after 1 or 2 years. However, the experimental data demonstrated that the tape would fail after 40 years. In this situation, the oil internal pressure is considered as an important factor lead to the failure of tape combining with pitting corrosion. Therefore, the FE model is built to investigate the relationship between oil pressure and critical pit depth.

Before the FEM model was applied, the geometry of the models needs to be decided. The thickness of the reinforcing tin-bronze tapes is approximately 150 μm . However, the distribution of the pits on the tape surface is unknown. As the experimental data

shows, a sample was chosen from the ROUTE A circuit 2. The sample size was about 5 cm x 2.5 cm, and 2,346 pits were found in this sample. Assuming that there are no overlapping pits, the area of each can be calculated by the following equation:

$$area = \frac{5 \times 2.5 \times 10^8}{2346} \mu m^2 = 532821 \mu m^2$$

Therefore, the geometry of the FEM model is 730 μm x 730 μm x 150 μm . Then, x_c can be calculated as 31.38 μm using equation (5.25), which means the pitting depth used in the FEM model is 31.38 μm . COMSOL Multiphysics 5.1 was used to simulate the computational model, and Figure 5.8 shows the geometry of the model in which the pit occurs in the centre of the plate. The thickness is 150 μm , and the stress is applied on the left- and right-hand sides of the shape. Due to the symmetry, the model only needs to analyse a quarter of the plate, and therefore the geometry of the pit on the tape can be simplified with a 2D model, as shown in Figure 5.9, while the parameters of the geometry and input boundary loads are shown in Table 5.1.

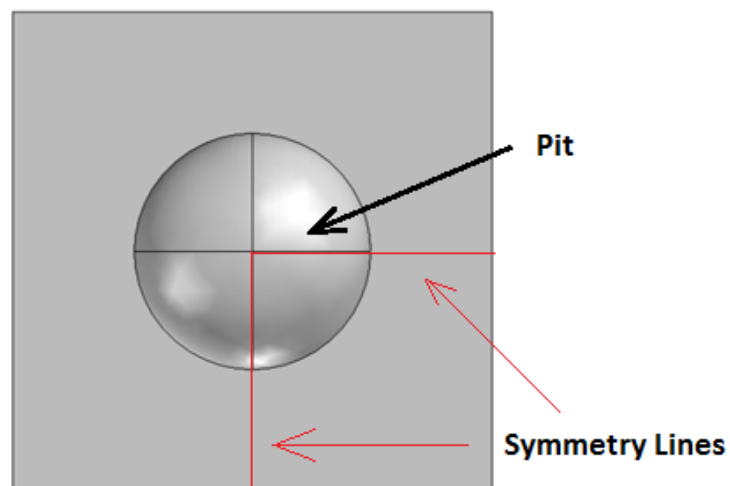


Figure 5.8: The plate geometry



Figure 5.9: The symmetry of the geometry of a pit occurs on the tape for a 2D model

Width	350 μm
Height	150 μm
Pitting depth	31.38 μm

Table 5.1: The input parameters of the model

Copper was chosen as an analytic material for the model. The FEM simulation has already been established using Solid Mechanics, and a number of boundary conditions have been automatically created. Before the boundary conditions were applied, the model was treated as a linear elastic model, after which boundary conditions were added. These are outlined in Table 5.2. The function $-(1\text{E-}6)*p$ is used for Prescribed Displacement 1 shows that the displacement in the x direction start from 0 to $1\text{E-}6$ m as the value of p has the range 0 to 1. And the function $\text{intop1}(v)$ indicates the

displacement in the y direction equal to the point of value of displacement at right-bottom corner.

Condition	Applied to	Parameters
Symmetry	Right side and Up side	
Prescribed Displacement 1	Left side	-(1E-6)*p
Prescribed Displacement 2	Bottom side	intop1(v)

Table 5.2: The constraints and loads for the model's geometry

After the boundary conditions were applied, the finite element mesh needed to be considered. The mesh refers to the sizes, shapes, and functions of the finite elements that the model is broken down into. The size of the elements relates to the distance between the nodes where numerical solutions are found, and therefore influence the resolutions of any solution. Different shapes and deformation functions may be required, depending on the geometry of the model. COMSOL can automatically define most of these parameters for simple models. For the model analysed in this chapter, the 'Free Tetrahedral' and 'normal' mesh was used. After running the finite element simulation, the results were displayed as von Mises stress. Figure 5.10 shows the distribution of the von Mises stress on the model surface.

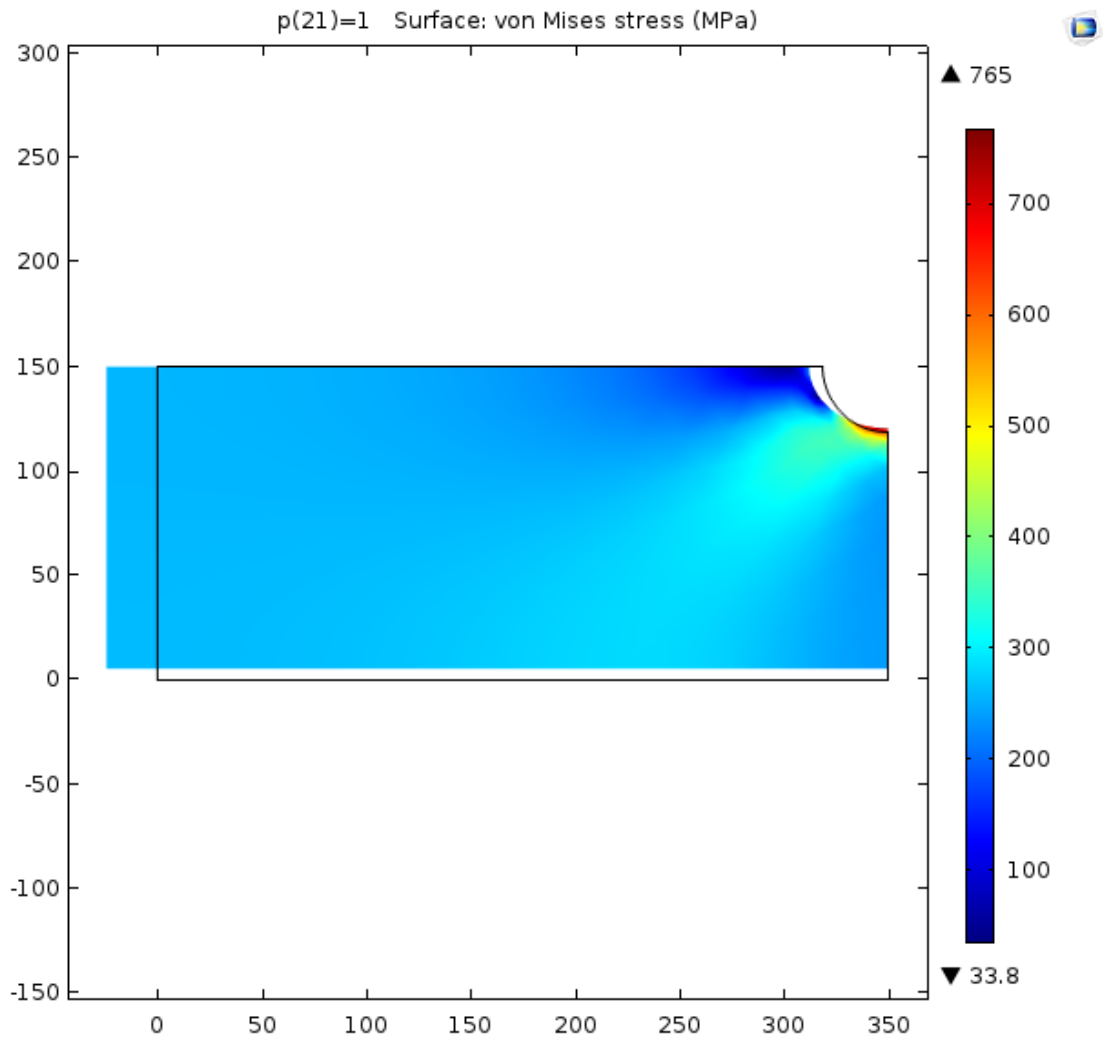


Figure 5.10: Von Mises stress of the 3D model

5.4 Mesh convergency study

The use of FEA software begins with a computer-aided design (CAD) model that represents the physical parts being simulated, as well as the knowledge of the material properties and applied loads and constraints. This information enables the prediction of real-world behaviour, often with very high levels of accuracy. The accuracy that can be obtained from any FEA model is directly related to the finite element mesh that is used. The finite element mesh is used to subdivide the CAD model into smaller domains called elements, for which a set of equations are solved. These equations approximately

represent the governing equation of interest via a set of polynomial functions defined for each element. Because these elements are made increasingly smaller as the mesh is refined, the computed solution will approach the true solution. This process of mesh refinement is a key step in validating any finite element model and gaining confidence in the software, model, and results.

Once all the materials properties, loads, and constraints are assembled into the FEA model, the analyst can begin with a preliminary mesh. Early in the analysis process, it makes sense to start with a mesh that is as coarse as possible (a mesh with very large elements). A coarse mesh requires less computational resources to solve and, although it may give a very inaccurate solution, it can still be used as a rough verification and check on the applied loads and constraints.

After computing the solution for the coarse mesh, the process of mesh refinement begins. In its simplest form, mesh refinement is the process of resolving the model with successively finer meshes, comparing the results between the different meshes. This comparison can be done by analysing the fields at one or more points in the model, or by evaluating the integral of a field over certain domains or boundaries. By comparing these scalar quantities, it is possible to judge the convergence of the solution with respect to mesh refinement. After comparing a minimum of three successive solutions, an asymptotic behaviour of the solution starts to emerge, and the changes in the solution between meshes become smaller. Eventually, these changes will be small enough that the analyst can consider the model to be converged. This is always a judgment call on the part of the analyst, who knows the uncertainties in the model inputs and the level of acceptable uncertainty in the results.

For the FEM model that is simulated by COMSOL, the element size of the mesh is chosen as 'Extra coarse' at the beginning. The 'von Mises stress' is chosen to display the stress on the model surface. Figure 5.11 shows the distribution of the von Mises stress with

the 'Extra coarse' element size for the 2D model. The maximum value of von Mises stress is picked and compared with other maximum values of stress in the finer mesh model. Then, the mesh is refined and made finer, which means the element size becomes increasingly smaller. By using COMSOL to analyse the model, the element size goes from 'Extra coarse' to 'Extra fine'. When the element size of mesh changes, the number of degrees of freedom differs; as the element size becomes smaller, the number of degrees of freedom goes larger. Figure 5.12 shows how the von Mises stress changes as the mesh becomes finer.

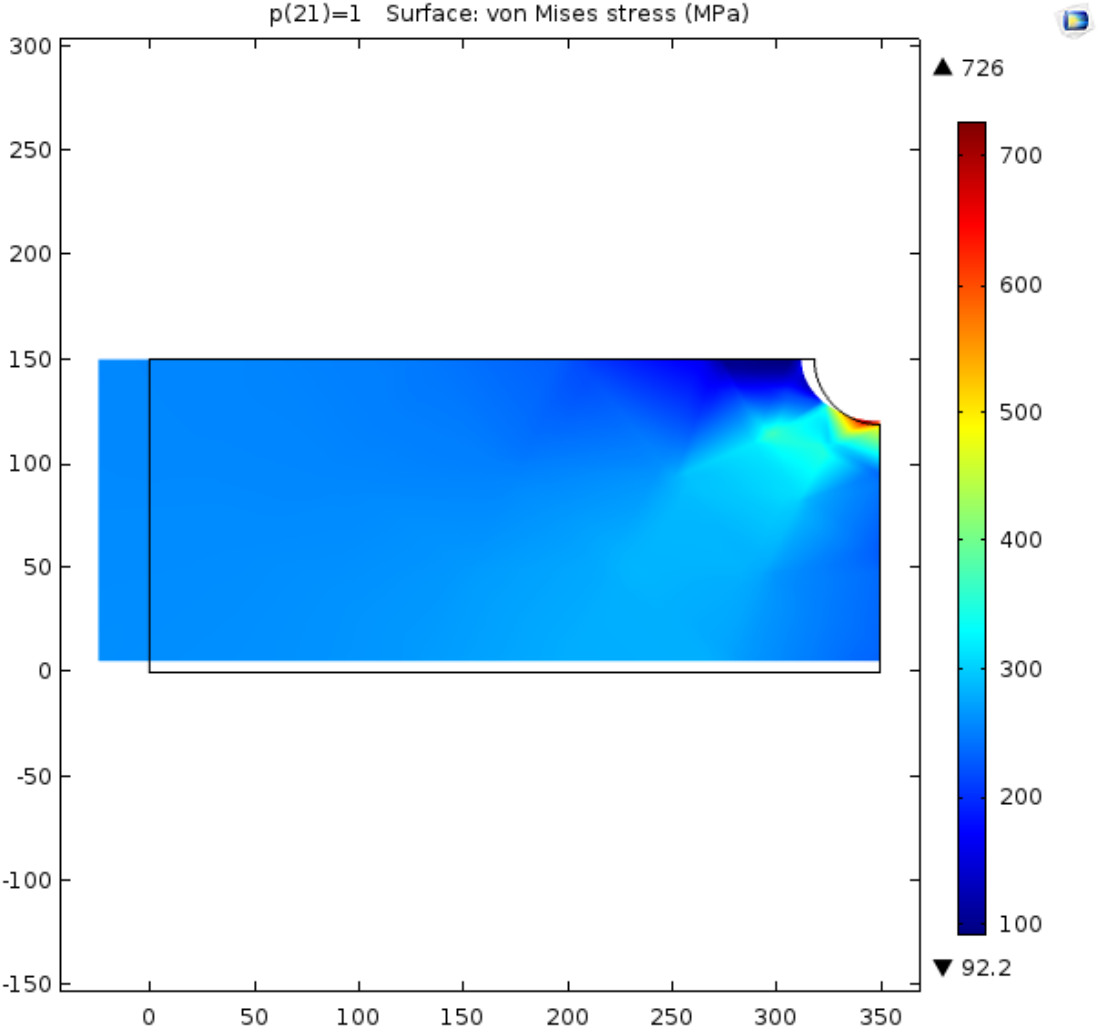


Figure 5.11: von Mises stress with the 'Extra coarse' mesh

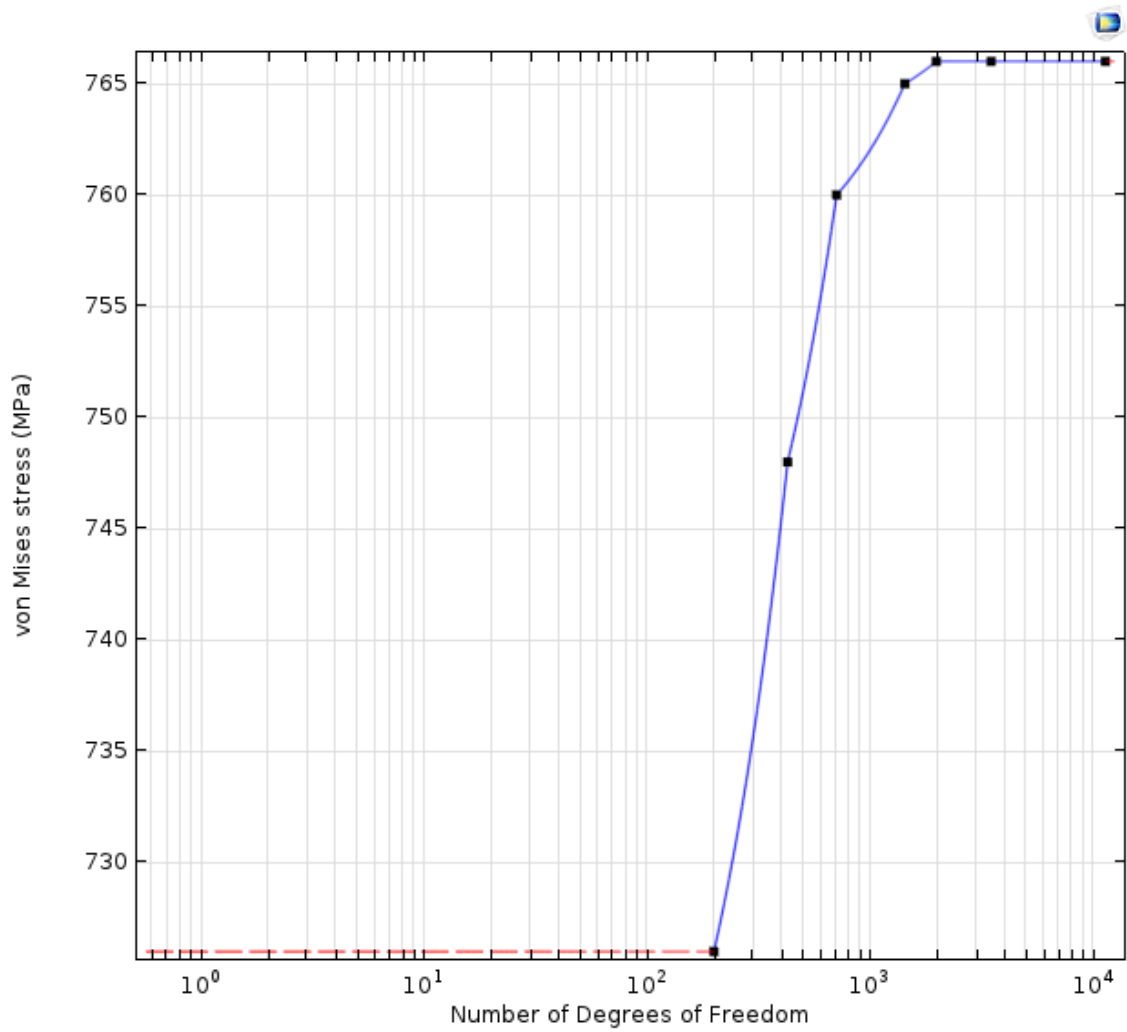


Figure 5.12: The von Mises stress with different element sizes

From Figure 5.12, it can be clearly seen that the last three von Mises stresses conform to a high degree of accuracy, which means the difference between each is less than 1%. In such a situation, it can be validated that the previously used coarser mesh is sufficiently fine, and the results can be accepted. Therefore, the COMSOL model that has been built can be used for the following analysis to gain accurate results.

5.5 An alternative failure criterion based on the Ultimate tensile strength

Based on the FEM model built in Section 5.3, Figure 5.13 shows the average applied stress in x direction against von Mises stress with the entire simulating process. In this model, it assumes that the material works with a linear elasticity environment. Hence, von Mises stress and applied stress show the linear tendencies during the model simulation in Figure 5.13. The material property indicates that the initial yield stress is 158 MPa, which means once the von Mises stress beyond 158MPa the material will work in the strain hardening region until it fails. Due to the curves shown in Figure 5.13, with 60 MPa average applied stress, the von Mises stress can reach to 158 MPa which indicates as the yield point for the material. Table 5.3 shows the working stresses of various sections of different circuits. It clearly demonstrates that all these circuits have higher working stress than 60 MPa. In such situation, the reinforcing tapes for all the circuits are operating beyond the elastic region and achieve to the hardening region. For failed cables, the material does not only work in a linear elasticity environment; plastic deformation also needs to be considered. Therefore, in order to simulate the COMSOL model accurately, it has to add a plasticity analysis to make the computational model more like the real case.

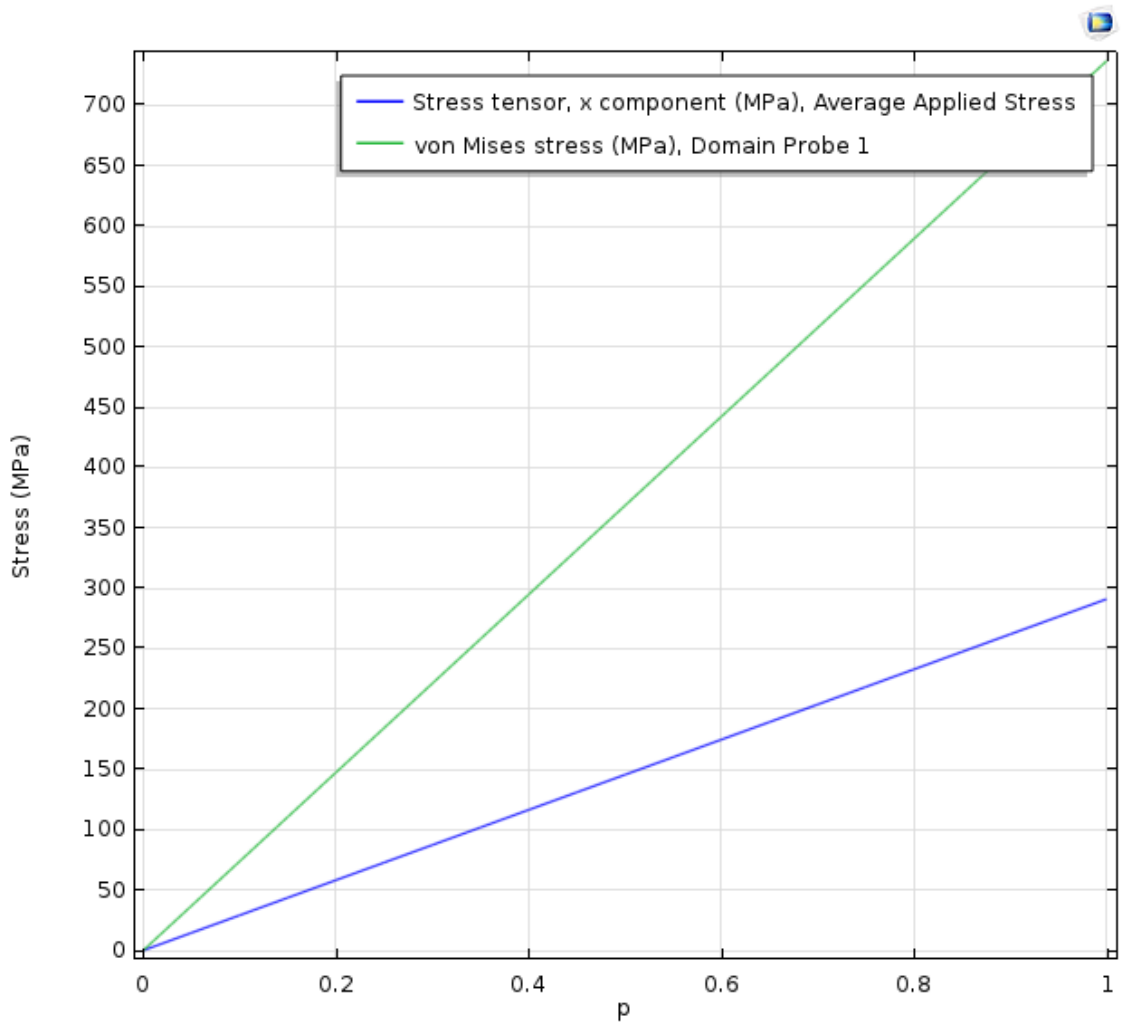


Figure 5.13: Average applied stress in x direction vs von Mises stress without plasticity added in the model

Circuit	Section	Total stress
ROUTE A circuit 1	1	114.9
ROUTE A circuit 1	18	124.87
ROUTE A circuit 1	61	145.23
ROUTE A circuit 2	18	120.07
ROUTE A circuit 2	61	145.23
ROUTE E circuit 1	94	111.8
ROUTE E circuit 2	93	116.02
ROUTE F circuit 1	100	142.78
ROUTE F circuit 1	133	134.33
ROUTE F circuit 2	96	138.2378
ROUTE F circuit 2	162	128.0158
ROUTE G circuit 1	1	144.6797
ROUTE G circuit 1	51	149.3118
ROUTE L circuit 1	9	96.49835
ROUTE L circuit 2	9	95.27955
ROUTE H	31	113.0083

Table 5.3: The working stresses of various sections of different circuits [3]

In this case of failure using an analysis of the plastic model, the parameters of the geometry of the COMSOL model can be derived from Table 5.2. For the elastic properties of the material, Young's modulus is 93 GPa, while Poisson's ratio is 0.35. For the plastic properties, the initial yield stress is 158 MPa, with a linear isotropic hardening with tangent modulus of 22 GPa. For the solid mechanics, the plasticity is added to the linear elastic material. After all the parameters and stresses have been inputted to the model, COMSOL will be able to solve the stress analysis of a failure cable. Figure 5.14 shows the average applied stress against von Mises stress with the plasticity added in the model. In this model, the critical pit depth is chosen as 30 μm .

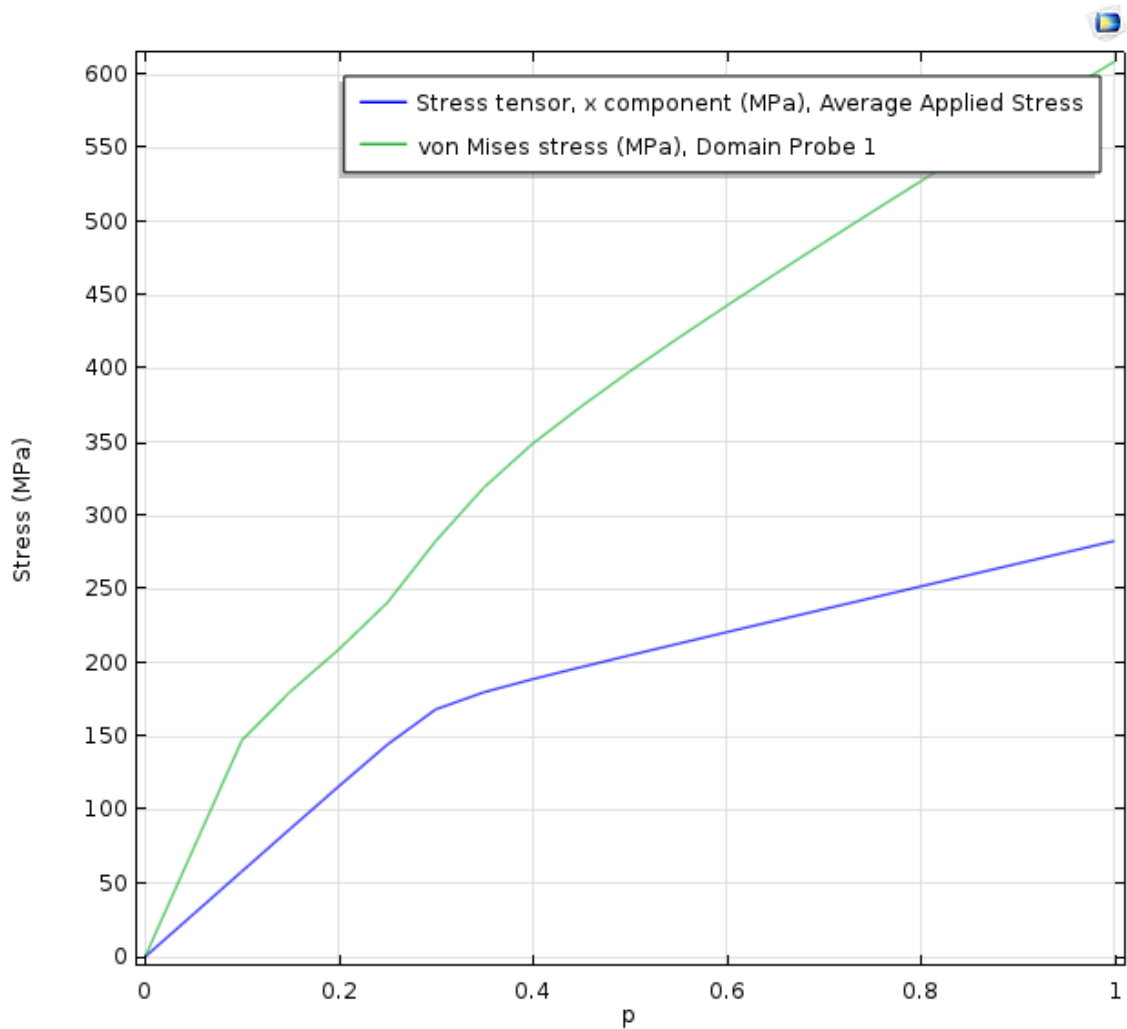


Figure 5.14: Average applied stress in x direction vs von Mises stress with plasticity added in the model

For the material failure condition based on tensile testing, the maximum von Mises stress should equal to Ultimate tensile strength (UTS). The UTS of reinforcing tape is 547 MPa which is gained from literatures. From Figure 5.14, when the von Mises stress is equal to 547 MPa, the applied stress can be calculated as 259MPa. Therefore, in this COMSOL model with critical pit depth equal to 30 μm , the failure condition can be treated as applied stress is 259 MPa. As discussed in previous sections, the critical pit depth may vary with different values gain from pitting corrosion model. Hence, after changing the critical pit depth to 90 μm , the relationship of applied stress and von Mises stress can be plotted in Figure 5.15. The value of average applied stress that satisfy with

the failure condition is 209 MPa when the critical pit depth equal 90 μm . Comparing with these two figures, it can be illustrated that with increased critical pit depth, the average applied stress that meet the failure condition turn into a relatively smaller value.

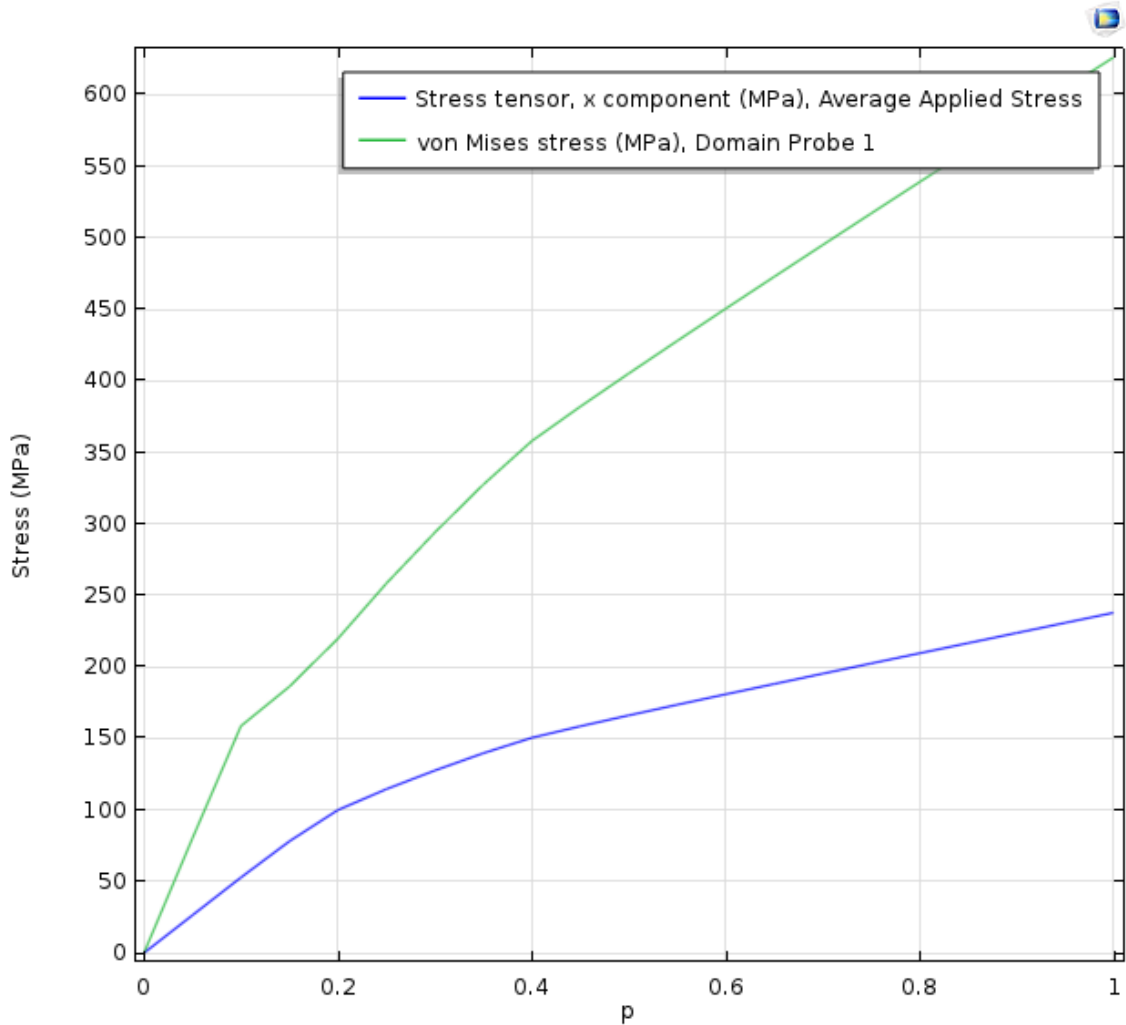


Figure 5.15: Average applied stress in x direction vs von Mises stress with plasticity added in the model and the pit depth is 90 μm

Figure 5.16 shows the tendency of average applied stress with increasing of critical pit depth. It clearly demonstrates that less average applied stress is needed to satisfy the failure condition when the pits grow deeper. Hence, with the pits occur on the reinforcing tin-bronze tapes, the higher working stress can lead to the tapes much easier

to fail. The trendline shows the applied stress to failure can be determined as a function of pit depth, and the analogous function of the curve is $F(x) = -0.0001x^3 + 0.0019x^2 + 0.1023x + 258.49$. Based on the experimental data which were shown in Table 5.3, the cables from three sections did not fail: the ROUTE E circuit 1, section 9; the ROUTE L circuit 1, section 9; and the ROUTE L circuit 2, section 9. Therefore, it can be concluded that the reinforcing tapes have not failed when the applied stress is less than 111.8 MPa and when the applied stress is larger than 113 MPa the tapes trend to fail. Hence, the critical applied stress can be simulated as the average value between these two failure and non-failure cases, which equals 112.4 MPa. With such critical applied stress (112.4 MPa), the critical pit depth then can be calculated by using the analogous function, which equals 123.3 μm . Therefore, when the pit depth on a tape is larger than the critical pit depth, the cable has failed, or has reached the 'at-risk' level. When the pit depth on a tape is less than the critical value, this cable has a low probability of reaching the 'risk' level and can stay in place for a longer period of time.

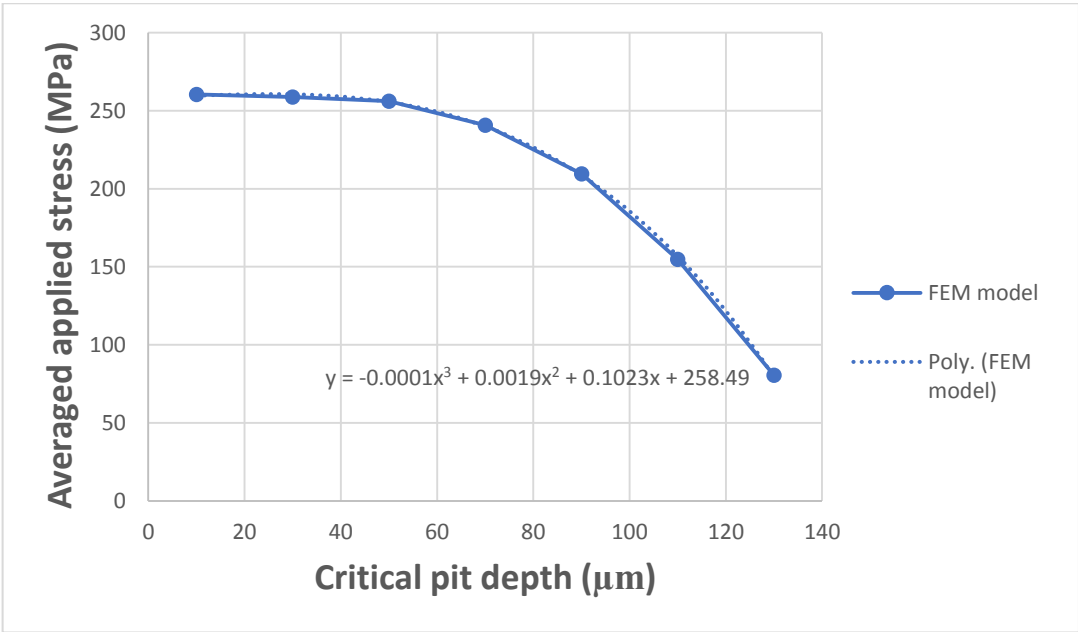
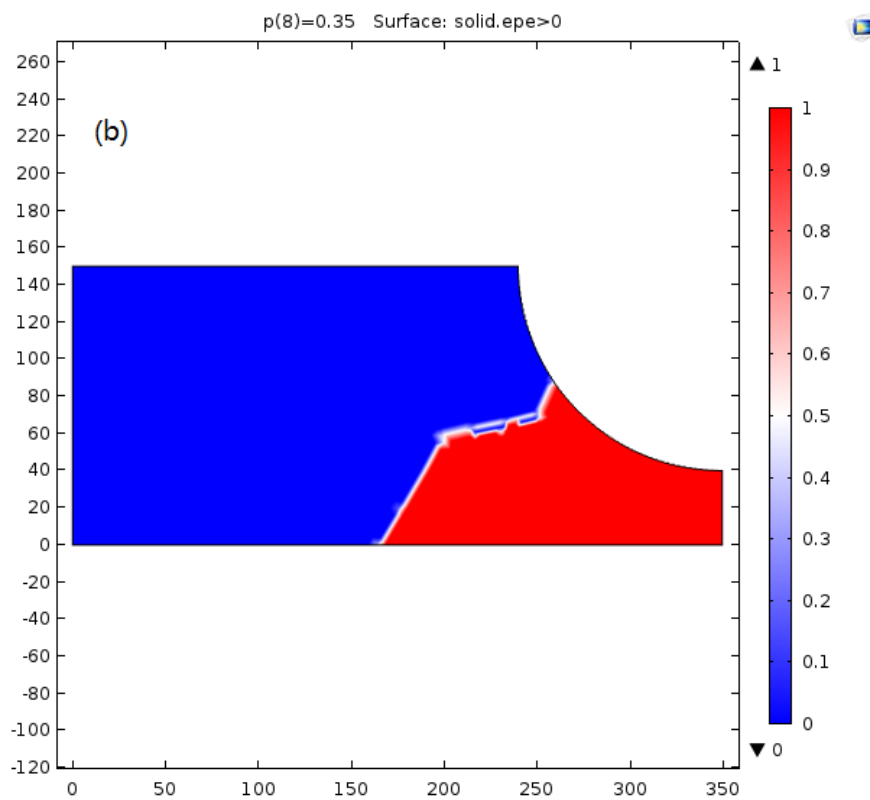
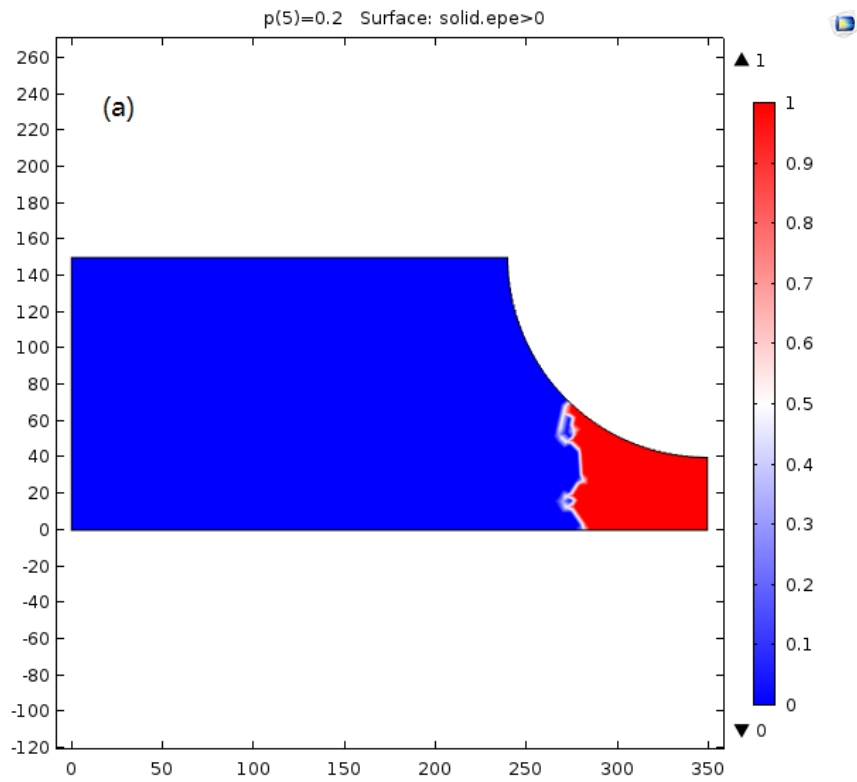


Figure 5.16: The averaged applied stress that meet the failure condition with different critical pit depth



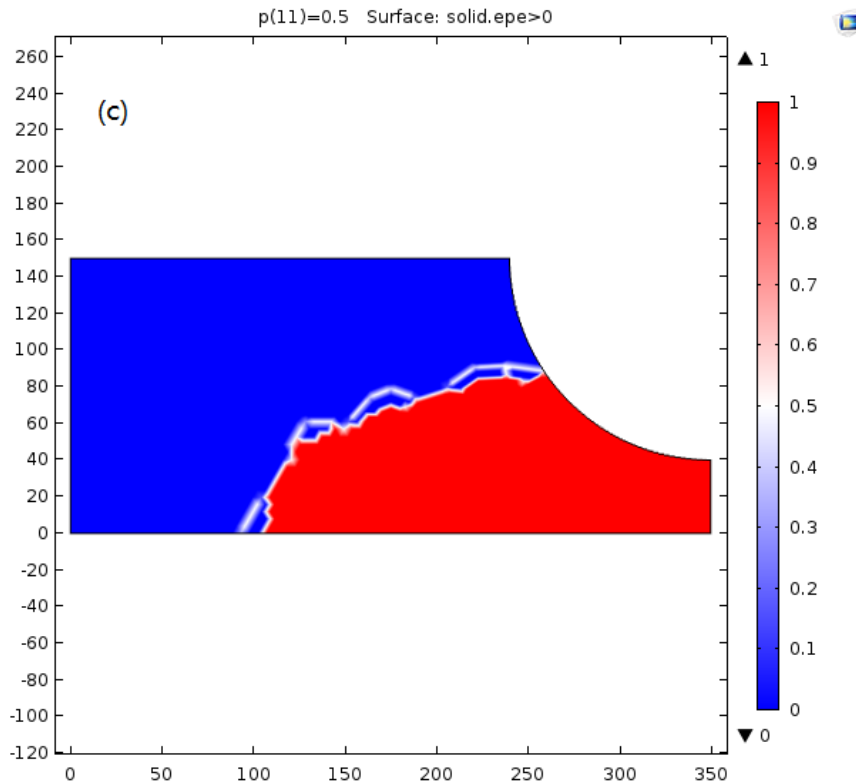


Figure 5.17: Plastic region for the FEM model with pit depth equal to 110 μm : (a) Applied stress with 73.95 MPa, (b) Applied stress with 104.57 MPa, (c) Applied stress with 130.40 MPa

For a further stress analysis, the 'Effective plastic strain (solid.epe)' is chosen to show the strain distribution by using the COMSOL model. However, the results only need to consider the plastic region, which means that the plastic strain is non-zero. In Figures 5.17, the red zones show where the plastic strain is non-zero. It can be clearly seen that for the relatively high applied stress, the plastic region occupies almost the half area. That means that under high applied stress, the material may lead to a relatively large plastic deformation, and this kind of large effective plastic deformation may lead to the failure of the material. As shown in Figure 5.17 (a), when the reinforcing tape works under a relatively low applied stress with a constant pit depth, the tape has a lower chance of reaching the 'at-risk' level. In other words, the reinforcing tape works in a safer environment, and has less chance of failure when the working stress or load condition is relatively low.

Based on the equation (5.10) with critical pit depth 123.3 μm , the critical time that lead to pit grows to such depth is just 398 days. After adding the dissolution time 100 days, the total time that a pit needed from nucleation to maximum value is approximately 500 days (less than 2 years). However, as discussed in previous sections, the Monte Carlo model shown almost all the pits cannot reach to the critical depth. Also, the experiment data shows that the cable failed after about 40 years. In this situation, the corrosion fatigue which was discussed in Section 5.1 should be considered during the whole serving time. Hence, the failed time can be determined from equation (5.6) and (5.9) as:

$$t_f = \frac{n}{C * \sigma_{\text{applied stress}}^p * x_c^{q-1}} \quad (5.29)$$

The crack growth parameters (C , p , and q) are determined from the experimental data. Then the failed time can be calculated as 47.87 years. Figure 5.18 shows the relationships between applied stress and failure time with a constant pit depth (123.3 μm). As a result, when the applied stress is increased, the serving time is reduced, and bring about the failure of the reinforcing tape.

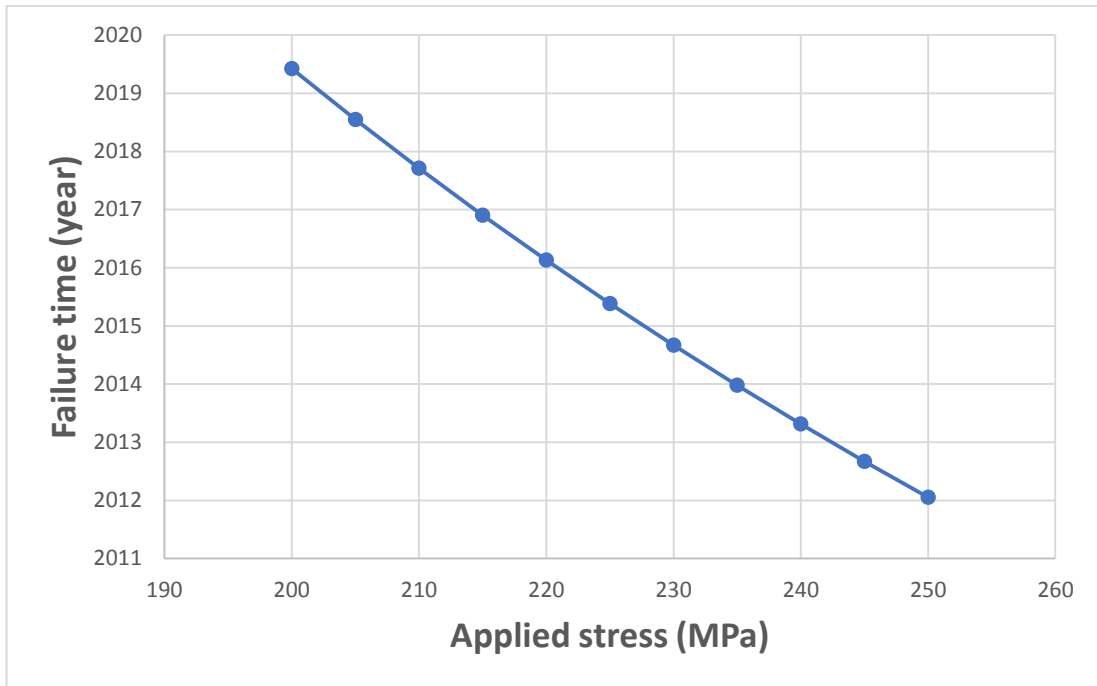


Figure 5.18: Applied stress against failure time with a constant pit depth

5.6 Summary

For the reinforcing tin-bronze tapes, a number of complex factors including pitting corrosion and internal oil pressure lead cables to fail. After reviewing the model of failure, it can be seen that when the pit depth reaches the critical value and will lead to the failure of the reinforcing tapes, with applied stress. A FEM model is introduced to specify the relation of critical pit depth and applied stress. To apply the FEM model, a mesh refinement study is needed to justify the computational model and thereby approach a true solution. In this COMSOL model, von Mises stresses are used to verify whether the model built is acceptable and can gain accurate results. The curve of the von Mises stresses in different element sizes reveals that they conform with each other to a high degree of accuracy, and the computational model can then be used to analyse the applied stress of the reinforcing tapes with pitting corrosion.

A simple 'non-interaction' model is built by using parameters from Chapter 4 (α , n & γ) to model the pit depth distribution. The parameters α and n are gained from the pit growth model without repassivation occurs. The value of parameter γ can vary only from 0.066 to 0.266. Then the critical size of pits x_c is defined with a probability of p_c of existing. When there is one or more pits reach to critical size, the reinforcing tin-bronze tapes will fail. Hence, a probability of failure is introduced by using Poisson distribution. The results demonstrate that for a relatively lower repassivation probability, the value of critical pit depth becomes bigger with a constant value of p_c . Similarly, for a relatively lower pit growth rate, critical pit depth turns into larger value as well.

In the COMSOL model, the failure condition of the reinforcing tape is examined. This kind of condition depends on the maximum stress equal to UTS and it shows how the applied stress with pit depth lead to the failure of the tape. When the pit depth remains a constant and the applied stress is reduced, the cable tends not to reach the failure criterion. Therefore, for reinforcing tapes that work under conditions of high oil pressure, the cable will face the 'at-risk' level and replacement or refurbishment needs to be considered. For the reinforcing tin-bronze tapes taken from the same circuit, the experimental data shows that certain pit depth cannot reach the critical value; with such small pit, the plastic region is significantly small, and will not lead to the failure of tape. The failure mechanism of the reinforcing tapes therefore depends not only on the pit depth, as discussed before, but also depends on high stress or load conditions.

For the reinforcing tin-bronze tapes with a critical pit depth, a COMSOL model is used to simulate the area of plastic deformation zones with various applied stresses. By comparing reinforcing tape with different applied stress, it can be seen that a large area is found when the reinforcing tapes will fail, while a relatively small area occurs when the tapes have not reached the failure level.

Chapter 6. Conclusions and recommendations for future work

6.1 Overall conclusions

In this work, a Monte Carlo method that has a mechanism of pitting corrosion was created to simulate the distribution of the pit depth for reinforcing tin-bronze tapes. This model examines the repassivation of the pit growth process, using the Monte Carlo method; the results were based on a large amount of simulated data, and eliminated some of the environmental uncertainties. Most of the parameters used in this simulation were gained from actual data of reinforcing tapes supplied by the National Grid. Using this model, a series of investigations were performed to come to understand the distribution of pit depth for various reinforcing tapes from different locations of underground power transmission cables. Additionally, further studies were performed to investigate the asset life of underground cables, using a distribution of pit depth to identify the 'at-risk' level of each cable.

A critical analysis of pitting corrosion data for the underground power transmission cables indicated that after being used for over 40 years, all the reinforcing tapes on the cables had different levels of pitting corrosion. The degree of pitting corrosion of these cables shows that environmental factors have different effects on pitting corrosion, and that these effects must be taken into account during a simulation. Moreover, experimental data from some failed cables proves that not all the reinforcing tapes that are corroded then fail, and only a certain amount of pitting corrosion leads to cable failure; in addition, the cables that have not failed show that slightly corroded reinforcing tapes have a relatively longer service life. The experimental procedure indicated that the tape samples removed from the cables may not contain the deepest pitting corrosion of the entire cable section or route, while it was also unlikely that the tape sections that were examined would show the deepest corrosion pit of the sample due to the limitations of the measurement procedure. Nevertheless, these pitting

corrosion data do reflect the failure probability of each cable. Based on these data, the asset life of the cables can be predicted to illustrate when they will reach the high risk of failure, and when the cable will need to be replaced or refurbished.

The computational model based on the Monte Carlo simulation successfully explained the mechanisms of pitting corrosion. In order to eliminate some uncertain external factors and make the results more credible, the model used a large amount of repeatable data to simulate the results. In the simulation of this model, based on the Monte Carlo principle, a large number of random numbers were used in the calculation process to ensure that these results were more truly reflective. The curve of the pit depth-time showed how the computational model can fit the empirical model, and the results of the pit depth distribution were therefore in a reliable range. The pit depth distribution showed that most of the pits repassivate before they can reach the maximum depth during the entire period of growth. However, unlike experimental data, the computational model indicates the maximum pit depth of the reinforcing tapes, which may not have been shown in the experimental observations. The dissolution time, which indicates that all the stable pits have nucleated, was tested with several values, and the results show little difference. Based on the experimental data, the best dissolution time for the computational model was chosen to be 100 days, which means that all the stable pits had nucleated within 100 days.

Based on the findings of Chapter 4, the statistical distributions of the pit depth from the computational data show a relatively high consistency with the experimental data from most of the reinforcing tin-bronze tapes. Furthermore, the computational model was validated by using the pit depth distribution of different service times to indicate that the model can accurately simulate the pit occurrence or growth of the reinforcing tin-bronze tapes. The dissolution time and environment temperature do not significantly affect the pit depth; the only parameter that needs to be considered is the delayed repassivation constant. However, the value of the repassivation constant will not

change sharply, according to the experimental and computational models. The range of the value varies from 0.066 to 0.266, and therefore by using this computational model to simulate the pit depth for various reinforcing tapes, the delayed repassivation constant should be used with different values to evaluate the distribution of the pit depth for various circuits. The high value of the delayed repassivation constant illustrates that the pits on the reinforcing tapes have a relatively low potential to grow, and therefore such reinforcing tapes have a lower probability of failure, compared to other tapes.

The study of the finite element model to come to a failure model, as presented in Chapter 5, revealed the importance of the applied stress working on the reinforcing tapes with a critical pit depth. After the applied stress is evaluated, the FEM model can analyse the effect of the critical pit depth. The properties of the reinforcing tapes indicate that with various internal oil pressures, all the tapes go beyond the elastic yield point, and are working in the hardening region. The plastic deformation zone clearly illustrates that for the reinforcing tapes that are under conditions of high oil pressure, the cable would be at an 'at-risk' level, and replacement or refurbishment would need to be considered. As the experimental data shows, most of the pits on the reinforcing tapes only penetrate 30% of the thickness, and do not reach the critical depth. With this pit depth, the FEM model also shows that the plastic deformation region occurs on the pit surface and in the area around the pit. Therefore, the failure mechanism of reinforcing tapes not only depends on the pit depth, as discussed previously, but also on high stress or load conditions. It was identified from the literature that these pits are likely to grow a maximum of three times, compared to those under zero or tensile loads.

In the study of the failure mechanisms in Chapter 5, it was found that there was a relation between the pit depth and applied stresses in the time to failure of the cables. The Monte Carlo model provided distributions of pit depth for each reinforcing tape to simulate the critical pit depth with the determination of the probability of failure. The

FEM model analysed the plastic deformation of each reinforcing tape with various applied stresses to simulate a critical pit depth which can lead to the failure of tape. This critical value was a criterion for judging the extent of failure for different circuits. Therefore, when a cable is worked with a relatively low applied stress, it can remain in place for a longer period of time, even with same deep pit depth, compared to other cables.

Overall, using the Monte Carlo simulation can translate into large computational time savings and great flexibility, both in enabling changed service times of reinforcing tapes, and in utilising the results from the experimental data and the parameters in the computational model to investigate the probability of failure for each cable. Furthermore, the FEM model is used to successfully analyse the failure mechanisms of the reinforcing tin-bronze tapes. This FEM model indicates the critical pit depth for all the failure cables and makes a comparison to illustrate the extent of failure of different reinforcing tapes. Moreover, the FEM model is adaptable and can be further extended by changing the pit depth scale and applied stress from the working environment.

6.2 Recommendations for future work

All the studies performed using the Monte Carlo simulation to track each pit independently and randomly. However, the experimental observations show that come of the pits that occur on the reinforcing tapes touch each other. Once this happens, the smaller pit is declared repassivated, and the two pits become one ellipsoidal pit, instead of two hemispherical pits. In case of such an overlap, the average potential drop of a pit is not the same as for a hemispherical pit. In future, the interactions between pits in the corrosion process can be considered by adding this pit shape calculation, and such a conclusion would be more accurate than the simplified model.

Another factor in the improvement of the Monte Carlo simulation is the environment of the soil conditions. The literature indicates, as revealed in Section 2.3.3, that electrolyte composition can influence the potential of pitting corrosion. Materials have a high chance of corroding with a relatively high concentration of aggressive anions, and with such a high concentration, pits tend to grow, rather than repassivate. Through the analysis of different soil conditions, the relationship between the concentration of aggressive anions and delayed repassivation constant is proven. However, for the aims of this research, the simplified model that examines the delayed repassivation constant was found to be satisfactory for simulating the pit depth distribution.

The FEM model with a single pit analysis could potentially be extended to a multi-pit analysis that accounts for the total number of pits on the reinforcing tape surface. The stress analysis then simulates the distributions of the strain deformation region of the entire tape, which in turn calculates the point on the entire tape that is most likely to fail. Since every pit occurs randomly on the tape and there is also overlap between the pits, the model must be based on extensive experimental data to ensure its accuracy and reliability, and therefore applying the multi-pit methodology to more complex geometries remains a challenge. Further work is needed to provide a satisfactory method for mapping these pits with various depths on a FEM model surface, which could also make use of the Monte Carlo method to simulate the position of each pit. Additionally, a 3D FEM model with complex geometries should be tested by the convergence study to ensure the model can simulate accurate results. The 3D FEM model with a simple single pit and applied stress analyses the plastic deformation region with static mean stress and alternating stress. As the corrosion fatigue has illustrated, the model with a single pit should experience a daily changed cyclic load, but further work is needed to incorporate the findings from the applied dynamic stress on the FEM model, and model more complex boundary conditions with time changes in 3D models.

References

1. Foresta, M.; Gnanasambandam, S.; Weston, D.; Li, F.; Pan, J. Z.; Blanc, M, L. Corrosion fatigue of phosphor bronze reinforcing tapes on underground power transmission cables – Failure analysis. *Engineering Failure Analysis*. 2018; 02. 006.
2. Zhou, H.; Gnanasambandam, S.; Foresta, M.; Li, F.; Blanc, M. L.; Weston, D.; Pan, J. Z. Life prediction of phosphor bronze reinforcing tape used in underground power cables. Accept by *CORROSION*.
3. Gnanasambandam, S.; Zhou, H; Foresta, M.; Weston, D.; Li, F.; Pan, J. Z.; Blanc, L. M. Measurement and Modelling of Pitting Depth Distribution for Phosphor Bronze Tapes Used in Underground Power Transmission Cables. *CORROSION*. 2017; Vol. 73, No. 7, pp. 844-852.
4. Dolley, E. J.; Lee, B.; Wei, R. P. The effect of pitting corrosion on fatigue life. *Fatigue and Fracture of Engineering Materials and Structures*. 2000; 23:6.
5. Blanc, C.; Mankowski, G. Susceptibility to pitting corrosion of 6065 aluminium alloy. *Corrosion Science*. 1997; 39:11.
6. Ezuber, H.; El-Houd, A.; El-Shawesh, F. A study on the corrosion behaviour of aluminium alloys in seawater. *Materials and Design*. 2008; 29:5.
7. McCafferty. E. Sequence of steps in the pitting of aluminium by chloride ions. *Corrosion Science*. 2003; 45:18.
8. Wei, R. P. Environmental considerations for fatigue cracking. *Fatigue and Fracture of Engineering Materials and Structures*. 2002; 25:10.
9. Pan, C.; Liu, L.; Li, Y.; Wang, F. Pitting corrosion of 304ss nanocrystalline thin film. *Corrosion Science*. 2013; 73:12.

10. Nakhaie, D.; Moayed, M. H. Pitting corrosion of cold rolled solution treated 17-4 PH stainless steel. *Corrosion Science*. 2014; 80:9.
11. Tian, W.; Du, N.; Li, S.; Chen, S.; Wu, Q. Metastable pitting corrosion of 304 stainless steel in 3.5% NaCl solution. *Corrosion Science*. 2014; 85:8.
12. Caleyó, F.; Velázquez, J. C.; Valor, A.; Hallen, J. M. Probability distribution of pitting corrosion depth and rate in underground pipelines: A Monte Carlo study. *Corrosion Science*. 2009; 51:10.
13. Foroulis, Z. A. Environment sensitive fracture of engineering materials. *The metallurgical society of AIME*. Warrendale, 1979.
14. Batchelor, A. W.; Chandrasekaran, M. & Lam, L. N. *Materials Degradation and Its Control by Surface Engineering*. 2014. Imperial College Press, Singapore.
15. Valor, A.; Velázquez, J. C.; Caleyó, F. and Hallen, J. M. Predictive Model for Pitting Corrosion in Buried Oil and Gas Pipelines. *National Association of Corrosion Engineers International*. 2009; 65, p. 332-342.
16. Mohd, M. H.; Kim, D. K.; Kim, D. W.; Paik, J. K. A time-variant corrosion wastage model for subsea gas pipelines. *Ships and Offshore Structures*. 2014; 9: 16.
17. Harara, W. Pit-depth measurement on large diameter pipes by tangential radiography using a Co-60 gamma-ray source. *Russian Journal of Nondestructive Testing*. 2004; 40: 7.
18. Alamilla, J. L.; Sosa, E. Stochastic modelling of corrosion damage propagation in active sites from field inspection data. *Corrosion Science*. 2008; 50, p. 1811-1819.
19. Turnbull, A.; McCartney, L. N.; Zhou, S. A model to predict the evolution of pitting corrosion and the pit-to-crack transition incorporating statistically distributed input parameters. *Corrosion Science*. 2006; 48, p. 2084-2105.
20. Rajasankar, J. and Iyer, N. R. A probability-based model for growth of corrosion pits in aluminium alloys. *Engineering Fracture Mechanics*. 2006; 73, p. 553-570.

21. Nathan, C. C.; Dulaney, C. L. Localized Corrosion. *NACE*. 1984.
22. Sheikh, A. K.; Boah, J. K.; Hansen, D. A. Statistical modeling of pitting corrosion and pipeline reliability. *Corrosion*. 1990; 46:8.
23. Johnsen, T.; Hilfer, R. Statistical prediction of corrosion front penetration. *Physical Review E - Statistical Physics, Plasmas, Fluids, and Related Interdisciplinary Topics*. 1997; 55:10.
24. Komukai, S.; Kasahara, K. On the requirements for a reasonable extreme value prediction of maximum pits on hot-water-supply copper tubing. *Journal of Research of the National Institute of Standards and Technology*. 1994, 99:6.
25. Isogai, T.; Katano, Y.; Miyata, K. Models and inference for corrosion pit depth data. *Extremes*. 2004; 7:18.
26. Valor, A.; Caleyó, F.; Alfonso, L.; Velázquez, J. C.; Hallen, J. M. Markov Chain models for the stochastic modeling of opitting corrosion. *Mathematical Problems in Engineering*. 2013; 13.
27. Cavanaugh, M. K.; Buchheit, R. G.; Birbilis, N. Modeling the environmental dependence of pit growth using neural network approaches. *Corrosion Science*. 2010; 52:8.
28. Shibata, T. W.R. Whitney Award lecture: statistical and stochastic approaches to localized corrosion. *Material und Organismen*. 1996; 52:18.
29. Engelhardt, G. R.; Macdonald, D. D. Monte Carlo Simulation of Localized Corrosion. *CORROSION*, 2008, New Orleans, April 2008, Paper no. 08270.
30. Cicek, V. *Cathodic Protection: Industrial Solutions for Protecting Against Corrosion*. 2013. Wiley.
31. Richardson, T. J. A. *SHREIR'S CORROSION*. 2010; Volume 2, 4th Edition.

32. Trethewey, K. R.; Chamberlain, J. *Corrosion for Science and Engineering*. 1995. Harlow: Longman, 2nd edition.
33. Williams, D. E.; Westcott, C.; Fleischmann, M. Stochastic models of pitting corrosion of stainless steels. I Modelling of the initiation and growth of pits at constant potential, *Journal of the Electrochemical Society*. 1985; 132: 1796.
34. Isaacs, H. S. The localized breakdown and repair of passive surfaces during pitting. *Corrosion Science*. 1989; 29: 313.
35. Baker, M. A. and Castle, J. E. The initiation of pitting corrosion at MnS inclusions. *Corrosion Science*. 1993; 34 (4), p. 667-82.
36. Landolt, D. *Corrosion and surface chemistry of metals*. 2007. EPFL press, Lausanne.
37. Burstein, G. T.; Pistorius, P. C.; Mattin, S. P. The nucleation and growth of corrosion pits on stainless steel. *Corrosion Science*. 1993; 35, p. 57-62.
38. Macdonald, D. D.; Engelhardt, G. R. *Predictive Modelling of Corrosion*. In: Shreir's Corrosion. 2010; Volume 2, p. 1630-1679. Amsterdam: Elsevier.
39. Böhni, H.; Suter, T. *Electrochim. Acta*. 2001; 47, 191.
40. Lohrengel, M. M.; Moehring, A.; Pilaski, M. *Electrochim. Acta*. 2001; 47, 137.
41. Frankel, G. J. *Electrochem. Soc.* 1998; 145, 2186.
42. Frankel, G. S. Pitting corrosion of metals: A review of the critical factors. *J. Electrochem. Soc.* 1998; 145, p. 2186-2198.
43. Soltis, J. Passive breakdown, pit initiation and propagation of pits in metallic materials – Review. *Corrosion Science*. 2015; 90, p. 5-22.
44. Angst, U.; Elsener, B.; Larsen, C. K.; Vennesland, Øystein. Chloride induced reinforcement corrosion: Rate limiting step of early pitting corrosion. *Electrochimica Acta*. 2011; 56, p. 5877-5889.

45. Ansari, T. Q.; Xiao, Z.; Hu, S.; Li, Y.; Luo, J. L.; Shi, S. Q. Phase-field model of pitting corrosion kinetics in metallic materials. *Computational Materials*. 2018; 4:38.
46. Alvarez, M. G.; Galvele, J. R. Pitting corrosion. *Shreir's Corrosion*. 2010. Volume 2. p. 772-800. Reference Module in Materials Science and Materials Engineering.
47. Horvath, J.; Uhlig, H. H. *J. Electrochem. Soc.* 1968; 115, 791.
48. Lislovs, E. A.; Bond, A. P. *J. Electrochem. Soc.* 1975; 122, 719.
49. Reding, J. T.; Newport, J. J. *Mater. Prot.* 1966; 5, p. 15-18.
50. Osorio, W. R.; Freire, C. M.; Caram, R.; Garcia, A. The role of Cu-based intermetallics on the pitting corrosion behaviour of Sn-Cu, Ti-Cu and Al-Cu alloys. *Electrochimica Acta*. 2012; 77, p. 189-197.
51. Liu, Z. Y.; Li, X. G.; Cheng, Y. F. Electrochemical state conversion model for occurrence of pitting corrosion on a cathodically polarized carbon steel in a near-neutral pH solution. *Electrochimica Acta*. 2011; 56, p. 4167-4175.
52. Da Cunha Belo, M.; Rondot, B.; Bergner, J.; Montuelle, J. *Mem. sci. rev. métallurg.* 1973; 70, 725.
53. Kong, D.; Dong, C.; Wei, X.; Man, C.; Lei, X.; Mao, F.; Li, X. Size matching effect between anion vacancies and halide ions in passive film breakdown on copper. *Electrochimica Acta*. 2018; 292, p. 817-827.
54. Kaesche, H. Z. *Phys. Chem. NF*. 1962; 34. P. 87-108.
55. Davis, J. R. *Surface Engineering for Corrosion and Wear Resistance*. 2001. ASM International. Materials Park.
56. Brown, B. F. *A preface to the problem of stress corrosion cracking*. In *Stress corrosion cracking of metals – a state of the art*. Edited by Craig, H. L., ASTM, Philadelphia PA, 1972; pp. 3-15.
57. Zaman, K. B. M. Q.; Wei, R. P. Probability approach for prediction of corrosion and corrosion fatigue life. *AIAA Journal*. 1994; 32, p. 2073-2079.
58. Kondo, Y.; Wei, R. P. Approach on quantitative evaluation of corrosion fatigue crack initiation condition. In: *Proceedings of EVALMAT89, Iron & Steel Institute of Japan, Kobe, Japan*. 1989; p. 135-138.

59. Wan, K. C.; Chen, G. S.; Gao, M.; Wei, R. P. Corrosion fatigue of a 2024-T3 aluminium alloy in the short crack domain. *Int. J. Fracture*. 1994; 69, R63-R67.
60. Sriraman, M. R.; Pidaparti, R. M. Crack Initiation Life of Materials Under Combined Pitting Corrosion and Cyclic Loading. *J Mater. Eng. Perform.* 2010; 19, 7-12.
61. Shi, P.; Mahadevan, S. Damage tolerance approach for probabilistic pitting corrosion fatigue life prediction. *Eng. Fract. Mech.* 2001; 68, p. 1493-1507.
62. Rokhlin, S. I.; Kim, J. Y.; Nagy, H.; Zoofan, B. Effect of pitting corrosion on fatigue crack initiation and fatigue life. *Eng. Fract. Mech.* 1999; 62, p. 425-444.
63. Qingyuan, W.; Kawagoishi, N.; Chen, Q.; Pidaparti, R. M. Evaluation of the probability distribution of pitting corrosion fatigue life in aircraft materials. *Acta Mech. Sinica*. 2003; 19, p. 247-252.
64. Ishihara, S.; Saka, S.; Nan, Z. Y.; Goshima, T.; Sunada, S. Prediction of corrosion fatigue lives of aluminium alloy on the basis of corrosion pit growth law. *Fatigue Fract. Eng. M.* 2006; 29, p. 472-480.
65. Hoepfner, D. W. Model for prediction of fatigue lives based upon a pitting corrosion fatigue process. J.T. Fong (Ed.) *Fatigue Mechanisms*, ASTM STP675, Philadelphia PA. 1979; p. 841.
66. Müller, M. Theoretical Considerations on Corrosion Fatigue Crack Initiation. *Mecall. Trans.* 1982; 13A, p. 649-655.
67. Kondo, Y. Prediction of Fatigue Crack initiation Life Based on Pit Growth. *Corrosion*. 1989; 45, p. 7-11.
68. Harlow, D. G.; Wei, R. P. A probability model for the growth of corrosion pits in aluminium alloys induced by constituent particles. *Engng Fract Mech.* 1998; 59, 305-25.

69. Chen, G. S.; Gao, M.; Wei, R. P. Microconstituent-Induced Pitting Corrosion in Aluminium Alloy 2024-T3. *Corrosion*. 1996; 52, 8-15.
70. Chen, G. S.; Wan, K. C.; Gao, M.; Wei, R. P.; Flournoy, T. H. Transition from pitting to fatigue crack growth - modelling of corrosion fatigue crack nucleation in a 2024-T3 aluminium alloy. *Mater. Sci. Eng. A – Struct.* 1996; 219, p. 126-132.
71. Harlow, D. G.; Wei, R. P. Probability modelling and material microstructure applied to corrosion and fatigue of aluminium and steel alloys. *Eng. Fract. Mech.* 2009; 76, p. 695-708.
72. Engelhardt, G.; Macdonald, D. D. Unification of the deterministic and statistical approaches for predicting localized corrosion damage. *I. Theoretical foundation, Corros. Sci.* 2004; 46, p. 2755-2780.
73. Engelhardt, G.; Macdonald, D. D.; Zhang, Y.; Dooley, B. Deterministic Prediction of Corrosion Damage in Low Pressure Steam Turbines Power Plant. *Chem.* 2004; 6, 647.
74. Turnbull, A.; Zhou, S. Pit to crack transition in stress corrosion cracking of a steam turbine disc steel. *Corros. Sci.* 2004; 46, p. 1239-1264.
75. Turnbull, A.; McCartney, L. N.; Zhou, S. Modelling of the evolution of stress corrosion cracks from corrosion pits. *Scripta Mater.* 2006; 54, 575-578.
76. Romanoff, M. *Underground corrosion*. 1957. NBS Circular 579, National Bureau of Standard, Washington, DC.
77. Foley, R. T. Localised corrosion of aluminium alloys – a review. *Corrosion*. 1986; 41, 277-88.
78. Cadaro, E. N.; Nakazato, R. Z.; Horovistiz, A. L.; Ribeiro, L. M. F.; Ribeiro, R. B.; Hein, L. R. O. An image processing method for morphological characterization and pitting corrosion evaluation. *Mater Sci Engng A*. 2002; 334, p. 298-306.

79. Orr, S. J.; Pyun, S. I.; Nam, S. W. Characterisation of pit morphology of sputtered Al-1 wt.% Si-0.5 wt.% Cu alloy thin films. *Thin Solid Films*. 1996; 279, 7-10.
80. Mooney, C. Z. *Monte Carlo simulation*. 1997. Calif, Thousand Oaks; Sage, London.
81. Liu, J. S.; Chen, R. Sequential Monte Carlo Methods for Dynamic Systems. *Journal of the American Statistical Association*. 1998; 93, 443.
82. Chao, C. Y.; Lin, L. F.; Macdonald, D. D. *J. Electrochem. Soc.* 1981; 128, 1194.
83. Macdonald, D. D.; Urquidi-Macdonald, M. *Electrochim. Acta*. 1986; 31, 1079.
84. Macdonald, D. D.; Urquidi-Macdonald, M. *J. Electrochem. Soc.* 1987; 124, 41.
85. Macdonald, D. D.; Urquidi-Macdonald, M. *J. Electrochem. Soc.* 1989; 136, 961.
86. Macdonald, D. D.; Urquidi-Macdonald, M. *J. Electrochem. Soc.* 1992; 139, p. 3434-3449.
87. Macdonald, D. D. *Pure Appl. Chem.* 1999; 71, p. 951-978.
88. Shibata, T. *Trans ISIJ*. 1983; 23, 785.
89. Fratesi, R. *Corrosion*. 1985; 41, 114.
90. Pistorius, P. S.; Burstein, G. T. *Philos. Trans. R. Soc. Lond. A*. 1992; 341, p. 531-559.
91. Carslaw, H. S.; Jaeger, J. C. *Conduction of Heat in Solids*. 1959. 2nd edition. Oxford Press: London.
92. Velazquez, J. C.; Van Der Weide, J. A. M.; Hernandez, E.; Hernandez, H. H. Statistical Modelling of Pitting Corrosion: Extrapolation of the Maximum Pit Depth-Growth. *Int. J. Electrochem. Sci.* 2014; 9, p. 4129-4143
93. Zapp, P. E. Growth Rate in Carbon Steel Exposed to Simulated Radioactive Waste. *NACE International Annual Corrosion Conf. and Exp.* 1996. March 24-29. Denver, Colorado. Paper No. 129.

94. Bradford, S. *Practical handbook of corrosion control in soils*. 2000. CASTI Corrosion Ser. Vol. 3. CASTI Pub. Inc. Edmonton, Canada.
95. Papavinasam, S.; Revie, R. W. Pipeline Protective Coating Evaluation. *NACE International Annual Corrosion Conf. and Exp.* 2006. March 12-16. San Diego, CA. Paper No. 06047.
96. Coles, S. *An introduction to statistical modelling of extreme values, springer series in statistics*. 2001. Springer-Verlag. London. UK.
97. Zhang, R.; Mahadevan, S. Reliability-based reassessment of corrosion fatigue life. *Struct Safety*. 2001; 23, p. 77-91.
98. Tousek, J. *Theoretical aspects of the Localized Corrosion of Metals*. 1985. Switzerland: Trans. Tech. Publications Ltd.
99. Rajasankar, J.; Iyer, N. R. Probabilistic modelling of growth of corrosion pit from particle clusters. *SST-MLP91-RR-08, SERC*. Chennai. 2004; Issue 1.0.
100. Argyris, J. H.; Kelsey, S. Energy Theorems and Structural Analysis. *Aircraft Engineering*. 1955; Vol. 27.
101. Clough, R. W. The Finite Element Method in Plane Stress Analysis. *Proceeding of 2nd ASCE Conference on Electronic Computation*. 1960. Pittsburg, PA. September.
102. Zienkiewicz, O. C. *The Finite Element Method in Engineering Science*. 1971. McGraw-Hill, London.
103. Martin, H. C.; Carey, G. F. *Introduction to Finite Element Analysis – Theory and Applications*. 1975. Tata McGraw-Hill Publishing Company Ltd.. New Delhi.
104. Cook, R. D.; Makus, D. S.; Plesha, M. F. *Concept and Applications of Finite Element Analysis*. 1981. John Wiley and Sons.
105. Krishnamoorthy, C. S. *Finite Element Analysis, Theory and Programming*. 1987. Tata McGraw-Hill Publishing Company Ltd.. New Delhi.

106. Chandrapatla, T. R.; Belegundu, A. D. *Introduction to Finite Elements in Engineering*. 1991. Prentice Hall.
107. Rajasekharan, S. *Finite Element Analysis in Engineering Design*. 1993. Wheeler Publisher.
108. Bhavikatti, S. S. *Finite Element Analysis*. 2004. New Age International Pvt. Ltd., Publishers.
109. Zhang, X.; Lian, Y.; Liu, Y.; Zhou, X. *The material point method*. 2013. In Chinese. Tsinghua University. Beijing.
110. Zienkiewicz, O. C. and Taylor, R. L. *The finite element method. Vol. 2. Solid and fluid mechanics Dynamics and non-linearity, 4th ed.* 1991. Published, McGraw-Hill Book Company Europe.
111. von Mises, R. Mechanik der Plastischen Formänderung der Kristallen. *Z. angew. Math. Mech.* 1928; 8, 161-85.
112. Herbert, F. M.; Norville, A. J. The creep of lead and lead alloys used for cable sheathing. 1932. *University of Illinois at Urbana-Champaign*.
113. Sherif, E. M.; Park, S. M. 2-Amino-5-ethyl-1, 3, 4-thiadiazole as a corrosion inhibitor for copper in 3.0% NaCl solutions. *Corros. Sci.* 2006; 48, p. 4065-4079.
114. Sherif, E. M.; Park, S. M. Effects of 2-Amino-5-ethyl-1, 3, 4-thiadiazole on copper corrosion as a corrosion inhibitor in aerated acidic pickling solutions. *Electrochim. Acta.* 2006; 51, p. 6556-6562.
115. Zhang, D.; Gao, L.; Zhou, G. Inhibition of copper corrosion in aerated hydrochloric acid solution by heterocyclic compounds containing a mercapto group. *Corros. Sci.* 2004; 46, p. 3031-3040.
116. Kear, G.; Barker, B. D.; Walsh, F. C. Electrochemical corrosion of unalloyed copper in chloride media – a critical review. *Corros. Sci.* 2004; 46, p. 109-135.
117. Yan, C. W.; Lin, H. C.; Cao, C. N. Investigation of inhibition of 2-mercaptobenzoxazole for copper corrosion. *Electrochim. Acta.* 2000; 45, p. 2815-2821.

118. Pareek, S.; Jain, D.; Hussain, S.; Biswas, A.; Shrivastava, R.; Parida, S. K.; Kisan, H. K.; Lgaz, H.; Chung, I.; Behera, D. A new insight into corrosion inhibition mechanism of copper in aerated 3.5wt% NaCl solution by eco – friendly Imidazopyrimidine Dye: experimental and theoretical approach. *Chemical Engineering Journal*. 2019; 358, p. 725-742.
119. International A. Standard Guide for Preparation of Metallographic Specimens. 2011.
120. International A. Standard Guide for Examination and Evaluation of Pitting Corrosion. 2005.
121. Ryaben'kii, V. S.; Tsynkov, S. V. *A Theoretical Introduction to Numerical Analysis*. 2006. CRC Press.
122. Song, C., Zhang, J. Electrocatalytic Oxygen Reduction Reaction. *PEM Fuel Cell Electrocatalysts and Catalyst Layers*. 2008. Springer, London.
123. Richards, T. W.; Collins, E.; Heimrod, G. W. The Electrochemical Equivalents of Copper and Silver. *Proceedings of the American Academy of Arts and Sciences*. 1899; 35: 8.
124. King, F.; Litke, C. D.; Quinn, M. J.; LeNeveu, D. M. The Measurement and Prediction of the Corrosion Potential of Copper in Chloride Concentration and Mass-Transfer Coefficient. *Corrosion Science*. 1995; 37: 5.
125. Sourisseau, T.; Chauveau, E.; Baroux, B. Mechanism of copper action on pitting phenomena observed on stainless steels in chloride media. *Corrosion Science*. 2005; 47, p. 1097-1117.

Appendices

Appendix I

Computer codes of main program

```
PROGRAM PITTING_DEPTH
!
IMPLICIT NONE
INTEGER,PARAMETER::iwp=SELECTED_REAL_KIND(15)
INTEGER::ELEMENT,j,jj,k,kk,kkk,n,it,itt
REAL::initial_I,Kv,alpha,KC,delta_CR,T,r,Faraday_constant,Gas_constant,b,delta_t,ti
me,x,total_t,abc,total_step,delta_step,step,AS,TOTAL
REAL(iwp),ALLOCATABLE::a(:,:),i(:,:),delta_Phi(:,:),New_a(:,:),Ndelta_Phi(:,:),AA(
(:,:),New_i(:,:))
    ,AO(:,:),G(:,:),RP_i(:,:),STOPPED_i(:,:),FINAL_a(:,:),FINAL_i(:,:),DK(:,:)
!
!-----input data-----
open (1,FILE='PITTING1-3.dat')
open (2,FILE='PITTING4-6.dat')
open (3,file='PITTING7-9.dat')
open (4,file='PITTING10-12.dat')
open (5,file='PITTING13-15.dat')
open (6,file='PITTING16-18.dat')
open (7,file='PITTING19-21.dat')
open (8,file='PITTING22-24.dat')
open (9,file='PITTING25-27.dat')
open (10,file='PITTING28-30.dat')
open (11,file='PITTING31-33.dat')
open (12,file='PITTING34-36.dat')
open (13,file='PITTING37-39.dat')
open (14,file='PITTING40-42.dat')
open (15,file='PITTING43-45.dat')
open (16,file='PITTING46-48.dat')
```

open (17,file='PITTING49-51.dat')
open (18,file='PITTING52-54.dat')
open (19,file='PITTING55-57.dat')
open (20,file='PITTING58-60.dat')
open (21,file='PITTING61-63.dat')
open (22,file='PITTING64-66.dat')
open (23,file='PITTING67-69.dat')
open (24,file='PITTING70-72.dat')
open (25,file='PITTING73-75.dat')
open (26,file='PITTING76-78.dat')
open (27,file='PITTING79-81.dat')
open (28,file='PITTING82-84.dat')
open (29,file='PITTING85-87.dat')
open (30,file='PITTING88-90.dat')
open (31,file='PITTING91-93.dat')
open (32,file='PITTING94-96.dat')
open (33,file='PITTING97-99.dat')
open (34,file='PITTING100.dat')

ELEMENT=10
initial_I=0.150 !(A/m2)
Kv=0.00002834784 !(m3/A*day)
alpha=1.0
KC=0.00002 !(A/V*m)
delta_CR=0.2 !(V)
T=298.15 !(K)
r=0.166 !(day-1)
Faraday_constant=96485.3 !(C/mol)
Gas_constant=8.31446 !(V*C/K*mol)
b=2.1
total_t=14600 !(day)
delta_t=1.0 !(day)

```

time=0.0
total_step=20
delta_step=1.0
step=0.0
!abc=exp(-alpha*Faraday_constant*1.0/(Gas_constant*T))
!write(12,*) abc
!S=0.0
!
!-----
ALLOCATE
(a(ELEMENT,ELEMENT),New_a(ELEMENT,ELEMENT)),RP_i(ELEMENT,ELEM
ENT),STOPPED_i(ELEMENT,ELEMENT)
ALLOCATE (i(ELEMENT,ELEMENT),New_i(ELEMENT,ELEMENT))
,G(ELEMENT,ELEMENT),DK(ELEMENT,ELEMENT)
ALLOCATE
(delta_Phi(ELEMENT,ELEMENT),Ndelta_Phi(ELEMENT,ELEMENT),AA(ELEME
NT,ELEMENT)),AO(ELEMENT,ELEMENT)

CALL INITIAL_DEPTH(ELEMENT,a)
CALL INITIAL_POTENTIAL(ELEMENT,delta_Phi)
CALL INITIAL_CURRENT_DENSITY(ELEMENT,initial_I,i)

DO it=1,total_t

    CALL CALCULATION_OF_PITTING_DEPTH(a,ELEMENT,New_a,Kv,delta_t,i)

    CALL
ALL_OTHER_PITS_POTENTIAL(ELEMENT,initial_I,KC,alpha,Faraday_constant,G
as_constant,T,AA,New_a,delta_Phi)
    CALL QIUHE(AA,AS,ELEMENT)
    CALL JIANFA(AA,AO,AS,ELEMENT)
    CALL INTERACTION_WITH_OTHER_PITS(ELEMENT,initial_I,KC,New_a,DK)
    CALL SUMM(ELEMENT,DK,TOTAL)

```

```

DO itt=1,total_step
  CALL
  AVERAGE_POTENTIAL_DROP(ELEMENT,initial_I,KC,alpha,Faraday_constant,delta_Phi,Gas_constant,T,Ndelta_Phi,b,New_a,AO,TOTAL)
  CALL UPDATE_THE_POTENTIAL(ELEMENT,Ndelta_Phi,delta_Phi)
  step=step+delta_step
END DO

CALL
CURRENT_DENSITY(ELEMENT,initial_I,alpha,Faraday_constant,Gas_constant,T,delta_Phi,i)
CALL
DECISION_OF_CURRENT_DENSITY(ELEMENT,delta_CR,initial_I,alpha,Faraday_constant,Gas_constant,T,delta_Phi,New_i,i)
CALL RANDOM_NUMBER_FOR_REPASSIVATION(ELEMENT,x,G)

CALL
PROBABILITY_OF_REPASSIVATION(ELEMENT,G,r,delta_t,RP_i,initial_I,alpha,Faraday_constant,Gas_constant,T,i)
CALL STOPPED_PITTING_DEPTH(ELEMENT,New_i,RP_i,STOPPED_i,i)
CALL UPDATE_PITTING_DEPTH(ELEMENT,New_i,i,New_a,a)

WRITE(1,*) a(1,1),a(2,1),a(3,1)
WRITE(2,*) a(4,1),a(5,1),a(6,1)
WRITE(3,*) a(7,1),a(8,1),a(9,1)
WRITE(4,*) a(10,1),a(2,1),a(2,2)
WRITE(5,*) a(2,3),a(2,4),a(2,5)
WRITE(6,*) a(2,6),a(2,7),a(2,8)
WRITE(7,*) a(2,9),a(2,10),a(3,1)
WRITE(8,*) a(3,2),a(3,3),a(3,4)
WRITE(9,*) a(3,5),a(3,6),a(3,7)

```

```
WRITE(10,*) a(3,8),a(3,9),a(3,10)
WRITE(11,*) a(4,1),a(4,2),a(4,3)
WRITE(12,*) a(4,4),a(4,5),a(4,6)
WRITE(13,*) a(4,7),a(4,8),a(4,9)
WRITE(14,*) a(4,10),a(5,1),a(5,2)
WRITE(15,*) a(5,3),a(5,4),a(5,5)
WRITE(16,*) a(5,6),a(5,7),a(5,8)
WRITE(17,*) a(5,9),a(5,10),a(6,1)
WRITE(18,*) a(6,2),a(6,3),a(6,4)
WRITE(19,*) a(6,5),a(6,6),a(6,7)
WRITE(20,*) a(6,8),a(6,9),a(6,10)
WRITE(21,*) a(7,1),a(7,2),a(7,3)
WRITE(22,*) a(7,4),a(7,5),a(7,6)
WRITE(23,*) a(7,7),a(7,8),a(7,9)
WRITE(24,*) a(7,10),a(8,1),a(8,2)
WRITE(25,*) a(8,3),a(8,4),a(8,5)
WRITE(26,*) a(8,6),a(8,7),a(8,8)
WRITE(27,*) a(8,9),a(8,10),a(9,1)
WRITE(28,*) a(9,2),a(9,3),a(9,4)
WRITE(29,*) a(9,5),a(9,6),a(9,7)
WRITE(30,*) a(9,8),a(9,9),a(9,10)
WRITE(31,*) a(10,1),a(10,2),a(10,3)
WRITE(32,*) a(10,4),a(10,5),a(10,6)
WRITE(33,*) a(10,7),a(10,8),a(10,9)
WRITE(34,*) a(10,10)
```

```
time=time+delta_t
```

```
END DO
```

```
END PROGRAM PITTING_DEPTH
```

```
!-----initial-----
```

```

SUBROUTINE INITIAL_DEPTH(ELEMENT,a)

IMPLICIT NONE
INTEGER,PARAMETER::iwp=SELECTED_REAL_KIND(15)
INTEGER::i,j
INTEGER,INTENT(IN)::ELEMENT
!REAL,INTENT(IN)::initial_I
REAL(iwp),INTENT(OUT)::a(10,10)
DO i=1,ELEMENT
  DO j=1,ELEMENT
    a(i,j)=0
    !delta_Phi(j)=0
    !i(j)=initial_I
  END DO
END DO
RETURN
END SUBROUTINE INITIAL_DEPTH

```

!-----

```

SUBROUTINE INITIAL_POTENTIAL(ELEMENT,delta_Phi)

IMPLICIT NONE
INTEGER,PARAMETER::iwp=SELECTED_REAL_KIND(15)
INTEGER::i,j
INTEGER,INTENT(IN)::ELEMENT
!REAL,INTENT(IN)::initial_I
REAL(iwp),INTENT(OUT)::delta_Phi(10,10)
DO i=1,ELEMENT
  DO j=1,ELEMENT
    !a(j)=0
    delta_Phi(i,j)=0
    !i(j)=initial_I
  END DO
END DO

```

```

RETURN
END SUBROUTINE INITIAL_POTENTIAL
!-----
SUBROUTINE INITIAL_CURRENT_DENSITY(ELEMENT,initial_I,i)

IMPLICIT NONE
INTEGER,PARAMETER::iwp=SELECTED_REAL_KIND(15)
INTEGER::j,k
INTEGER,INTENT(IN)::ELEMENT
REAL,INTENT(IN)::initial_I
REAL(iwp),INTENT(OUT)::i(10,10)
DO j=1,ELEMENT
  DO k=1,ELEMENT
    !a(j)=0
    !delta_Phi(j)=0
    i(j,k)=initial_I
  END DO
END DO
RETURN
END SUBROUTINE INITIAL_CURRENT_DENSITY
!-----
!-----1-----pitting depth-----
SUBROUTINE
CALCULATION_OF_PITTING_DEPTH(a,ELEMENT,New_a,Kv,delta_t,i)
IMPLICIT NONE
INTEGER,PARAMETER::iwp=SELECTED_REAL_KIND(15)
INTEGER::jj,kk
INTEGER,INTENT(IN)::ELEMENT
REAL,INTENT(IN)::Kv,delta_t
REAL(iwp),INTENT(IN)::a(10,10),i(10,10)!delta_Phi(10)
REAL(iwp),INTENT(OUT)::New_a(10,10)
  DO jj=1,ELEMENT
    DO kk=1,ELEMENT

```

```

        New_a(jj,kk)=a(jj,kk)+Kv*delta_t*i(jj,kk)!initial_I*2.718**(-
alpha*Faraday_constant*delta_Phi(jj)/(Gas_constant*T))
    END DO
END DO
RETURN
END SUBROUTINE CALCULATION_OF_PITTING_DEPTH
!-----
!-----
!
!-----2-----potential of all other pits on the corroding surface-----
SUBROUTINE
ALL_OTHER_PITS_POTENTIAL(ELEMENT,initial_I,KC,alpha,Faraday_constant,G
as_constant,T,AA,New_a,delta_Phi)
IMPLICIT NONE
INTEGER,PARAMETER::iwp=SELECTED_REAL_KIND(15)
INTEGER::jj,kk
INTEGER,INTENT(IN)::ELEMENT
REAL,INTENT(IN)::initial_I,KC,alpha,Faraday_constant,Gas_constant,T
REAL(iwp),INTENT(IN)::New_a(10,10),delta_Phi(10,10)
REAL(iwp),INTENT(OUT)::AA(10,10)

DO jj=1,ELEMENT
    DO kk=1,ELEMENT
        AA(jj,kk)=(initial_I*New_a(jj,kk)*New_a(jj,kk)/KC)*(exp(-
alpha*Faraday_constant*delta_Phi(jj,kk)/(Gas_constant*T)))
    END DO
END DO
RETURN
END SUBROUTINE ALL_OTHER_PITS_POTENTIAL
!-----
SUBROUTINE QIUHE(AA,AS,ELEMENT)
IMPLICIT NONE
INTEGER,PARAMETER::iwp=SELECTED_REAL_KIND(15)

```

```

INTEGER::jj,kk
INTEGER,INTENT(IN)::ELEMENT
REAL(iwp),INTENT(IN)::AA(10,10)
REAL,INTENT(OUT)::AS
AS=0
DO jj=1,ELEMENT
  DO kk=1,ELEMENT
    AS=AS+AA(jj,kk)
  END DO
END DO
RETURN
END SUBROUTINE QIUHE
!-----
!
!-----
SUBROUTINE JIANFA(AA,AO,AS,ELEMENT)
IMPLICIT NONE
INTEGER,PARAMETER::iwp=SELECTED_REAL_KIND(15)
INTEGER::jjj,kkk
INTEGER,INTENT(IN)::ELEMENT
REAL,INTENT(IN)::AS
REAL(iwp),INTENT(IN)::AA(10,10)
REAL(iwp),INTENT(OUT)::AO(10,10)
DO jjj=1,ELEMENT
  DO kkk=1,ELEMENT
    AO(jjj,kkk)=AS-AA(jjj,kkk)
  END DO
END DO
RETURN
  END SUBROUTINE JIANFA
!
SUBROUTINE
INTERACTION_WITH_OTHER_PITS(ELEMENT,initial_I,KC,New_a,DK)

```

```

IMPLICIT NONE
INTEGER,PARAMETER::iwp=SELECTED_REAL_KIND(15)
INTEGER::j,k
INTEGER,INTENT(IN)::ELEMENT
REAL,INTENT(IN)::initial_I,KC
REAL(iwp),INTENT(IN)::New_a(10,10)
REAL(iwp),INTENT(OUT)::DK(10,10)
DO j=1,ELEMENT
  DO k=1,ELEMENT
    IF (j.EQ.k.EQ.1) THEN
      DK(j,k)=0
    ELSE
      DK(j,k)=initial_I*New_a(j,k)*New_a(j,k)/(KC*1000*SQRT((j-1)*(j-1)+(k-1)*(k-1)))
    END IF
  END DO
END DO
RETURN
END SUBROUTINE INTERACTION_WITH_OTHER_PITS
!
SUBROUTINE SUMM(ELEMENT,DK,TOTAL)
IMPLICIT NONE
INTEGER,PARAMETER::iwp=SELECTED_REAL_KIND(15)
INTEGER::j,k
INTEGER,INTENT(IN)::ELEMENT
REAL(iwp),INTENT(IN)::DK(10,10)
REAL(iwp),INTENT(OUT)::TOTAL
TOTAL=0

DO j=1,ELEMENT
  DO k=1,ELEMENT
    TOTAL=TOTAL+DK(j,k)
  END DO

```

```

END DO
RETURN
  END SUBROUTINE SUMM

!

!-----3-----center pit potential drop-----
SUBROUTINE
AVERAGE_POTENTIAL_DROP(ELEMENT,initial_I,KC,alpha,Faraday_constant,del
ta_Phi,Gas_constant,T,Ndelta_Phi,b,New_a,AO,TOTAL)
IMPLICIT NONE
INTEGER,PARAMETER::iwp=SELECTED_REAL_KIND(15)
INTEGER::j,k
INTEGER,INTENT(IN)::ELEMENT
REAL,INTENT(IN)::initial_I,KC,alpha,Faraday_constant,Gas_constant,T,b,TOTAL
REAL(iwp),INTENT(IN)::delta_Phi(10,10),New_a(10,10),AO(10,10)
REAL(iwp),INTENT(OUT)::Ndelta_Phi(10,10)
DO j=1,ELEMENT
  DO k=1,ELEMENT
    Ndelta_Phi(j,k)=delta_Phi(j,k)-((b*New_a(j,k)*initial_I/KC)*exp(-
alpha*Faraday_constant*delta_Phi(j,k)/(Gas_constant*T))-
delta_Phi(j,k)+AO(j,k)*TOTAL)/((-
b*New_a(j,k)*initial_I*alpha*Faraday_constant/(KC*Gas_constant*T))*exp(-
alpha*Faraday_constant*delta_Phi(j,k)/(Gas_constant*T))-1)
  END DO
END DO
RETURN
  END SUBROUTINE AVERAGE_POTENTIAL_DROP

!
!
!
!
!-----4-----UPDATE THE POTENTIAL-----

```

```

SUBROUTINE UPDATE_THE_POTENTIAL(ELEMENT,Ndelta_Phi,delta_Phi)
IMPLICIT NONE
INTEGER,PARAMETER::iwp=SELECTED_REAL_KIND(15)
INTEGER::j,k
INTEGER,INTENT(IN)::ELEMENT
REAL(iwp),INTENT(IN)::Ndelta_Phi(10,10)
REAL(iwp),INTENT(OUT)::delta_Phi(10,10)
DO j=1,ELEMENT
  DO k=1,ELEMENT
    delta_Phi(j,k)=Ndelta_Phi(j,k)
  END DO
END DO
RETURN
END SUBROUTINE UPDATE_THE_POTENTIAL

```

!-----4.5 CURRENT DENSITY-----

```

SUBROUTINE
CURRENT_DENSITY(ELEMENT,initial_I,alpha,Faraday_constant,Gas_constant,T,d
elta_Phi,i)
IMPLICIT NONE
INTEGER,PARAMETER::iwp=SELECTED_REAL_KIND(15)
INTEGER::j,k
INTEGER,INTENT(IN)::ELEMENT
REAL,INTENT(IN)::initial_I,alpha,Faraday_constant,Gas_constant,T
REAL(iwp),INTENT(IN)::delta_Phi(10,10)
REAL(iwp),INTENT(OUT)::i(10,10)
DO j=1,ELEMENT
  DO k=1,ELEMENT
    i(j,k)=initial_I*(exp(-alpha*Faraday_constant*delta_Phi(j,k)/(Gas_constant*T)))
  END DO
END DO
RETURN
END SUBROUTINE CURRENT_DENSITY

```

!-----5-----compare potential and critical-----

SUBROUTINE

DECISION_OF_CURRENT_DENSITY(ELEMENT,delta_CR,initial_I,alpha,Faraday_constant,Gas_constant,T,delta_Phi,New_i,i),CR_a)

IMPLICIT NONE

INTEGER,PARAMETER::iwp=SELECTED_REAL_KIND(15)

INTEGER::jj,kk

INTEGER,INTENT(IN)::ELEMENT

REAL,INTENT(IN)::delta_CR,initial_I,alpha,Faraday_constant,Gas_constant,T

REAL(iwp),INTENT(IN)::delta_Phi(10,10),i(10,10)

REAL(iwp),INTENT(OUT)::New_i(10,10)

DO jj=1,ELEMENT

DO kk=1,ELEMENT

IF(delta_Phi(jj,kk).LT.delta_CR) THEN

New_i(jj,kk)=i(jj,kk)

ELSE

New_i(jj,kk)=0

END IF

END DO

END DO

RETURN

END SUBROUTINE DECISION_OF_CURRENT_DENSITY

!-----

!

!-----6-----generate a random number-----

SUBROUTINE RANDOM_NUMBER_FOR_REPASSIVATION(ELEMENT,x,G)

IMPLICIT NONE

INTEGER,PARAMETER::iwp=SELECTED_REAL_KIND(15)

INTEGER::n,k

INTEGER,INTENT(IN)::ELEMENT

REAL,INTENT(IN)::x

```

REAL,INTENT(out)::x
REAL(iwp),INTENT(OUT)::G(10,10)

CALL RANDOM_SEED()
DO n=1,ELEMENT
  DO k=1,ELEMENT
    CALL RANDOM_NUMBER(x)
    G(n,k)=x
  END DO
END DO
RETURN
END SUBROUTINE RANDOM_NUMBER_FOR_REPASSIVATION
!-----
!
!-----7---probability of repassivation-----
SUBROUTINE
PROBABILITY_OF_REPASSIVATION(ELEMENT,G,r,delta_t,RP_i,initial_I,alpha,F
araday_constant,Gas_constant,T,i)
IMPLICIT NONE
INTEGER,PARAMETER::iwp=SELECTED_REAL_KIND(15)
INTEGER::jj,kk
INTEGER,INTENT(IN)::ELEMENT
REAL,INTENT(IN)::r,delta_t,initial_I,alpha,Faraday_constant,Gas_constant,T
REAL(iwp),INTENT(IN)::G(10,10),i(10,10)
REAL(iwp),INTENT(OUT)::RP_i(10,10)
DO jj=1,ELEMENT
  DO kk=1,ELEMENT
    IF(G(jj,kk).GT.(r*delta_t)) THEN

      RP_i(jj,kk)=i(jj,kk)
    ELSE

      RP_i(jj,kk)=0
    
```

```

        END IF
    END DO
END DO
RETURN
END SUBROUTINE PROBABILITY_OF_REPASSIVATION
!
!
!-----
!-----8-----stop pitting depth-----
SUBROUTINE
STOPPED_PITTING_DEPTH(ELEMENT,New_i,RP_i,STOPPED_i,i)
IMPLICIT NONE
INTEGER,PARAMETER::iwp=SELECTED_REAL_KIND(15)
INTEGER::j,k
INTEGER,INTENT(IN)::ELEMENT
REAL(iwp),INTENT(IN)::New_i(10,10),RP_i(10,10),i(10,10)
REAL(iwp),INTENT(OUT)::STOPPED_i(10,10)
DO j=1,ELEMENT
    DO k=1,ELEMENT
        IF((New_i(j,k)*RP_i(j,k)).EQ.0) THEN
            STOPPED_i(j,k)=0
        ELSE
            STOPPED_i(j,k)=i(j,k)
        END IF
    END DO
END DO

RETURN
END SUBROUTINE STOPPED_PITTING_DEPTH
!-----
!
!-----9-----final pitting depth and current density every step-----
!-----

```

```

!
!-----10-----UPDATE PITTING DEPTH-----
SUBROUTINE UPDATE_PITTING_DEPTH(ELEMENT,New_i,i,New_a,a)
IMPLICIT NONE
INTEGER,PARAMETER::iwp=SELECTED_REAL_KIND(15)
INTEGER::j,k
INTEGER,INTENT(IN)::ELEMENT
REAL(iwp),INTENT(IN)::New_i(10,10),New_a(10,10)
REAL(iwp),INTENT(OUT)::i(10,10),a(10,10)
DO j=1,ELEMENT
  DO k=1,ELEMENT
    a(j,k)=New_a(j,k)
    i(j,k)=New_i(j,k)
  END DO
END DO
RETURN
END SUBROUTINE UPDATE_PITTING_DEPTH
!-----

```

Appendix II

Computer code of pits nucleation program

```
PROGRAM PITTING_DEPTH
!
IMPLICIT NONE
INTEGER,PARAMETER::iwp=SELECTED_REAL_KIND(15)
INTEGER::ELEMENT,i
REAL::b,y,a,Tau,initial_N
REAL(iwp),ALLOCATABLE::z(:),AA(:),P(:)

OPEN (2,FILE='ERROR FUNCTION')
ELEMENT=1000
initial_N=450
b=10
a=3.65
Tau=100

ALLOCATE (z(ELEMENT),AA(ELEMENT),P(ELEMENT))

CALL NEIRONG(ELEMENT,a,b,AA,Tau)
CALL ERROR_FUNCTION(ELEMENT,AA,z,b,initial_N)
CALL PROBABILITY(ELEMENT,initial_N,z,P)

!-----(-3,10,-42,216,-1320,9360,-75600,685440,-6894720,76204800)-----
y=1-2*(b-b**3/3+b**5/10-b**7/42+b**9/216-b**11/1320+b**13/9360-
b**15/75600+b**17/685440-b**19/6894720+b**21/76204800-
b**23/918086400)/sqrt(3.14)

DO i=1,ELEMENT
WRITE(2,*) z(i),P(i)
```

END DO

END PROGRAM PITTING_DEPTH

!-----

SUBROUTINE NEIRONG(ELEMENT,a,b,AA,Tau)

IMPLICIT NONE

INTEGER,PARAMETER::iwp=SELECTED_REAL_KIND(15)

INTEGER::i

INTEGER,INTENT(IN)::ELEMENT

REAL,INTENT(IN)::a,b,Tau

REAL(iwp),INTENT(OUT)::AA(1000)

DO i=1,ELEMENT

AA(i)=a/(i-Tau)+b

END DO

RETURN

END SUBROUTINE NEIRONG

!-----

SUBROUTINE ERROR_FUNCTION(ELEMENT,AA,z,b,initial_N)

IMPLICIT NONE

INTEGER,PARAMETER::iwp=SELECTED_REAL_KIND(15)

INTEGER::i

INTEGER,INTENT(IN)::ELEMENT

REAL,INTENT(IN)::b,initial_N

REAL(iwp),INTENT(IN)::AA(1000)

REAL(iwp),INTENT(OUT)::z(1000)

DO i=1,ELEMENT

z(i)=initial_N*erfc(AA(i))/erfc(b)

END DO

RETURN

END SUBROUTINE ERROR_FUNCTION

!-----

```
SUBROUTINE PROBABILITY(ELEMENT,initial_N,z,P)
```

```
IMPLICIT NONE
```

```
INTEGER,PARAMETER::iwp=SELECTED_REAL_KIND(15)
```

```
INTEGER::i
```

```
INTEGER,INTENT(IN)::ELEMENT
```

```
REAL,INTENT(IN)::initial_N
```

```
REAL(iwp),INTENT(IN)::z(1000)
```

```
REAL(iwp),INTENT(OUT)::P(1000)
```

```
DO i=1,ELEMENT-1
```

```
    P(i)=(z(i+1)-z(i))/(initial_N-z(i))
```

```
END DO
```

```
RETURN
```

```
    END SUBROUTINE PROBABILITY
```

```
!-----
```

```
!-----GENERATE A RANDOM NUMBER-----
```

```
SUBROUTINE GENERATE_RANDOM_NUMBER(ELEMENT,x,Gk)
```

```
IMPLICIT NONE
```

```
INTEGER,PARAMETER::iwp=SELECTED_REAL_KIND(15)
```

```
INTEGER::n
```

```
INTEGER,INTENT(IN)::ELEMENT
```

```
REAL,INTENT(out)::x
```

```
REAL(iwp),INTENT(OUT)::Gk(1000)
```

```
CALL RANDOM_SEED()
```

```
DO n=1,ELEMENT
```

```
    CALL RANDOM_NUMBER(x)
```

```
    Gk(n)=x
```

```
END DO
```

```
RETURN
```

```
    END SUBROUTINE GENERATE_RANDOM_NUMBER
```